University of Alberta

Measurement of Carrier Fluid Viscosities for Oil Sand Extraction and Tailings Slurries

by

Jessie Lynne Smith

A thesis submitted to the Faculty of Graduate Studies and Research
in partial fulfillment of the requirements for the degree of

Master of Science
in
Chemical Engineering

Department of Chemical and Materials Engineering

Spring 2013
Edmonton, Alberta

Abstract

The mining of oil sands ore and extraction of bitumen produces aqueous slurries containing bitumen, coarse sand and fine clays. The performance of key process units is highly dependent on the rheology of “carrier fluid”, which is comprised of the fine solids and water. Although viscosity is important in process design and monitoring, it is rarely measured and instead determined using correlations. Viscosity depends on numerous factors including fines concentration, solids mineralogy and water chemistry - properties reflected in the size of aggregates formed by agglomerating solid species. More accurate correlations could be obtained by using additional correlating parameters. In this project rheology measurements were obtained using a concentric cylinder rheometer and compared with fines and aggregate volume fractions determined from particle image analysis. Multiple linear regression of key variables provided an equation to predict viscosity using fines content and calcium ion concentration as correlating parameters.

Acknowledgement

My eternal gratitude is given to my friends and family. I could not have completed this work without their love and support. Thank you especially to my parents, Debbie and Harold, for their endless encouragement and to my aunt, Lynn, who provided my home away from home.

Thank you to my supervisor, Dr. Sean Sanders, for his guidance and teaching. It is with immense gratitude that I acknowledge his patience, knowledge, and enthusiasm that were so crucial to this work.

I am indebted to the entire Pipeline Transport Processes research group. Thank you especially to Terry Runyon, whose help in and out of the lab has been invaluable throughout this process. I would like to thank Azadeh Asadi, Maedeh Marefatallah, Marzieh Saadat, Roberto Fedon, Kofi Adane, and Jean Sebastien Kroll-Rabotin for their technical support, training, and kind words.

Finally I would like to thank the NSERC Industrial Research Chair in Pipeline Transport Processes and the Canadian Oil Sands Network for Research and Development for providing financial support. I would particularly like to acknowledge Jason Schaan from Shell and Peter Cleyle from Suncor for their time and assistance. Special thanks to Dr. Zhenghe Xu for the generous use of his laboratory facilities.

Table of Contents

List of Tables

List of Figures

List of Symbols

Symbol	Description	Units
A_p	projected area	m^2
B	empirical correlating parameter	–
c_i	ion molarity	mol/L
C	solids volume fraction	–
d	particle diameter	μm
f_n	normalized frequency	μm^{-1}
g	acceleration due to gravity	m/s^2
I	ionic strength	–
L	rheometer spindle length	m
m	mass	g
N	number index	–
P_p	particle perimeter	m
R_1	rheometer spindle radius	m
R_2	rheometer cup radius	m
u_∞	terminal settling velocity	m/s
t	time	s or min
V_C	deposition velocity	m/s
$\overline{V}_{sample}$	sample volume	m^3
w	weight fraction	–
Z_i	ion charge number	–

Greek

α	rheometer system factor	m^3
$\dot{\gamma}$	shear rate	1/s
μ	viscosity	mPas
μ_r	relative viscosity	–
ρ	density	kg/m^3
τ	shear stress	Pa
τ_0	Bingham yield stress	Pa
T	torque	Nm
T_{min}	minimum torque to exceed yield stress	Nm
ω	spindle speed	rad/s
ω_{crit}	maximum spindle speed for laminar flow	rad/s

Subscripts

agg	aggregate
B	bitumen
calc.	calculated
CE	circle equivalent
f	fines
floc	floc
i	component index
L	suspending liquid
max.	maximum packing
meas.	measured
S	solids
P	Bingham plastic
W	water

1. Problem Statement

1.1. Slurries in the Oil Sands Industry

The extraction of bitumen from the Athabasca oil sands involves numerous large scale mining operations, occupying over 140,000 km^2 from which 1.6 million barrels of crude oil is produced each day (Canadian Association of Petroleum Producers, 2012). Typical oil sands ore contains coarse sands, fine mineral and clay solids, formation water and bitumen (Masliyah et al., 2011). Oil sands ore is mined then taken by truck from the mine site to crushers. At this stage ore is broken into smaller lumps and combined with water to create an oil sands slurry, which is delivered by hydrotransport pipeline to the extraction plant. The oil sands hydrotransport pipeline is sometimes referred to as a conditioning line because key steps must occur in this pipeline to ready the slurry for the downstream bitumen extraction processes (Masliyah et al., 2004).

The success of bitumen recovery relies on the efficiency of three key conditioning processes: ablation or size reduction of oil sands lumps, liberation of bitumen from sand particles, and aeration of bitumen droplets (Masliyah et al., 2004). It is necessary that the flow behaviour of slurries is well understood in order to optimize hydrotransport conditioning and bitumen recovery, as well as to avoid plugging and damage of facilities that can occur due to the settling of coarse particles. Current hydrotransport pipeline design models require knowledge of slurry flow behaviour to determine operating parameters such as pressure drop due to friction losses and minimum operating velocity (Sanders & Gillies, 2012).

Aqueous slurries are produced and handled at a number of mining and extraction process stages, including: hydrotransport, gravity separation, floatation, froth treatment and tailings disposal (Masliyah et al., 2004). An estimated 500 000 tonnes of solids are transported in slurry form within operating plants each day (Sanders et al. 2004). An example of oil sands extraction operations is shown in Figure 1.1 (adapted from Masliyah et al., 2011).

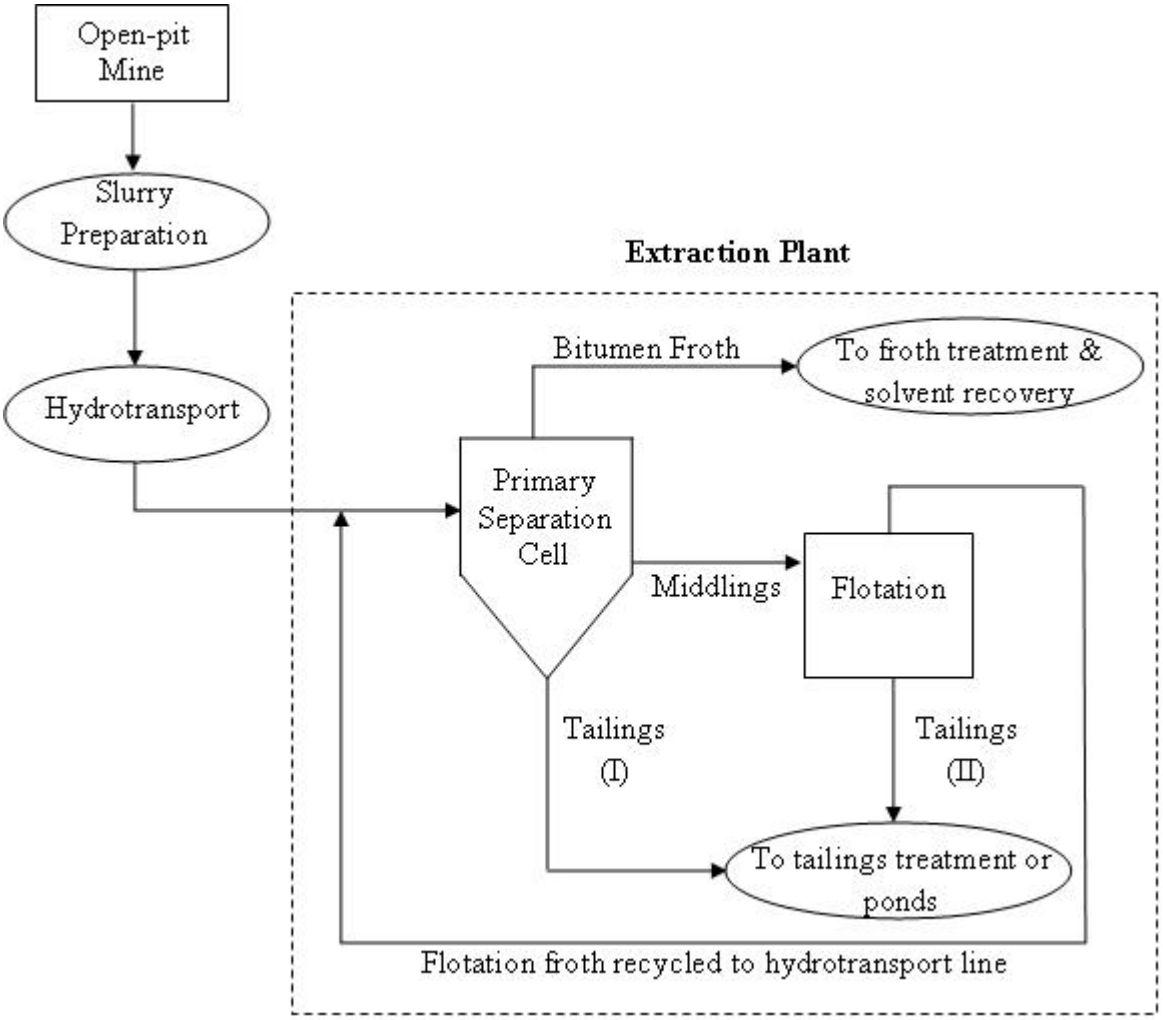

Figure 1.1: Process flow sheet of mining and extraction of bitumen from oil sands ore (adapted from Masliyah et al., 2011).

Upon reaching the extraction facility, hydrotransport slurry is sent through the primary separation cell (PSC) where gravity separation of coarse solids and flotation of aerated bitumen can occur (Masliyah et al., 2004). The bitumen froth from this unit is collected and sent for further froth treatment to remove water and fine solids. The middlings slurry stream, containing fine suspended particles, water and unrecovered bitumen, is sent through additional flotation stages to maximize bitumen recovery. Primary tailings flow from the PSC to tailings treatment facilities or to collection ponds. Froth recovered during secondary flotation is recycled into the hydrotransport slurry. Secondary flotation and froth treatment stages also produce tailings streams, which must be transported through plant piping to processing facilities.

Knowledge of slurry physical properties and flow behaviour is critical in the design and operation of separation equipment. High slurry viscosity can be problematic because it may cause gelation or sludging in separation vessels. This hinders the settling of coarse particles and aeration of bitumen, thereby reducing overall bitumen recovery (Adeyinka et al. 2009). Sludging occurs due to the presence of fine, aggregating clay particles in suspension (Adeyinka et al, 2009). Fine particles and the suspending liquid interact to produce a fluid-like, non-settling mixture that tends to have a greater viscosity than water alone (Michaels & Bolger, 1962; Shook et al., 2002).

1.2. Carrier Fluid and the Two-Layer Model

The flow behaviour of slurries is modeled using the Saskatchewan Research Council (SRC) Two-Layer Model (Shook et al., 2002). In this model heterogeneous (settling) slurries may be represented by two components: coarse settling solids and a pseudo-fluid referred to as carrier fluid. The carrier fluid is comprised of the suspending liquid (i.e. water) and fine suspended particles. A schematic of the pipeline cross-section for heterogeneous slurries is shown in Figure 1.2.

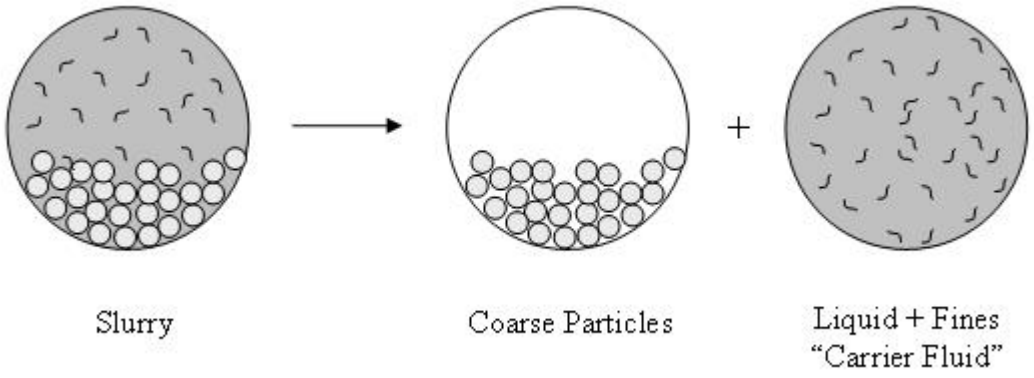

Figure 1.2: Pipeline cross section for a heterogeneous (settling) slurry.

Carrier fluid rheology is an extremely important input for the use of this model, as it has a significant impact on equipment design and operating parameters like pressure gradient and deposition velocity. The deposition velocity of slurry is the minimum operating velocity above which coarse particles remain fully suspended in the carrier fluid during flow. Operating below the deposition velocity may result in settling or excessive wear which can cause damage to pipelines and other

process equipment including erosion, or even complete plugging. Figure 1.3 shows an example of the effect of carrier fluid viscosity on deposition velocity for a specific slurry, with a solids density of 2650 kg/m^3 and a liquid density of 1000 kg/m^3. Detailed calculation of deposition velocity is given by Shook et al. (2002).

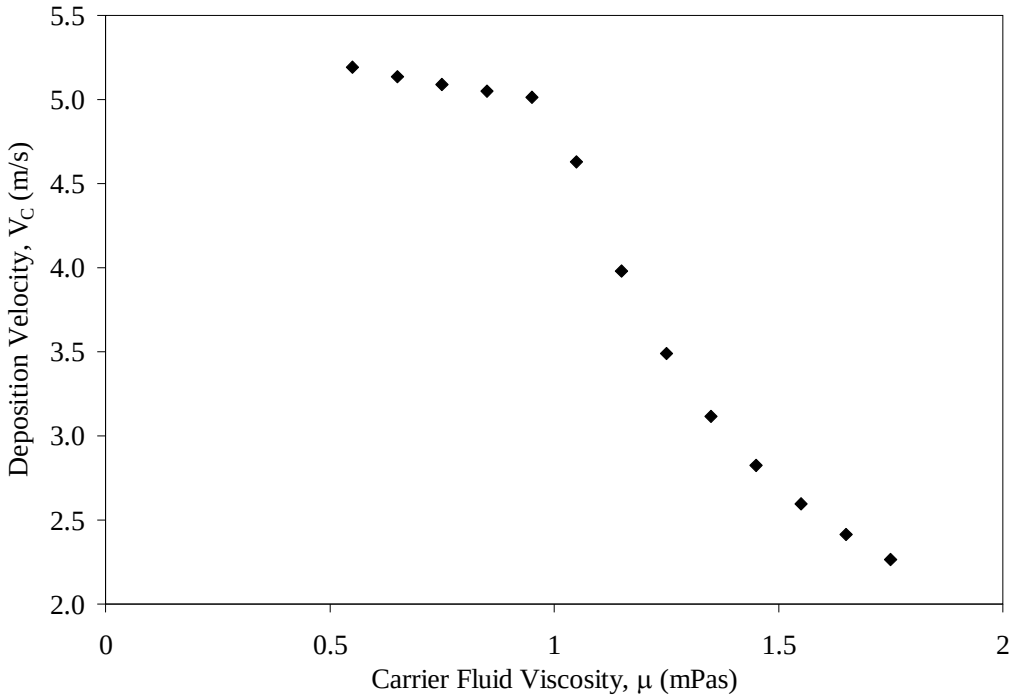

Figure 1.3: Effect of carrier fluid viscosity on the deposition velocity of 180 μm coarse particles in a 30% slurry through a 0.68 m pipeline.

It is evident from Figure 1.3 that at low values of carrier fluid viscosity, the minimum operating velocity is much higher. It is essential to use an accurate value of carrier fluid viscosity to determine the correct deposition velocity. Underestimation of the minimum operating velocity could lead to deposition

within pipelines and possibly total plugging, requiring shut down of the pipeline for flushing and repair. Overestimation of deposition velocity causes high frictional losses, pump power consumption and much higher pipeline wear rates (Sanders et al., 2004).

Although carrier fluid viscosity is critical in the design and operation of slurry process equipment it is rarely measured in industrial settings (Schaan, 2011). Rheological measurements cannot be made online, and preparing samples for off-site testing is difficult and time consuming. Typically empirical correlations are used to determine this essential fluid property. Problems arise when the correlation chosen is not appropriate for the slurry being examined.

The selection of a carrier fluid viscosity correlation will directly influence the prediction of deposition velocity and the chosen operating velocity of a pipeline system. Operating velocity is used to predict may other parameters, for example the frictional pressure losses determined using the SRC Two-Layer model (Shook et al., 2002). Improper choice of the minimum operating velocity and resulting pressure losses can lead to inappropriate pump sizing possibly causing pipeline blockages for undersized pumps, or wasted energy and resources for oversized equipment.

Work done by Einstein (Shook et al., 2002) related viscosity to particle concentration for dilute suspensions containing inert, non-interacting spherical particles. Although this study provides the foundational knowledge of suspension viscosity it cannot be used to describe the complex particle interactions present in industrial slurries, which contain non-spherical particles at higher concentrations. A study by Adeyinka et al. (2009) examined the rheology of suspensions created from varying size fractions of solids taken from industrial mature fine tailings samples. It was seen that for samples of equal concentration, the viscosity was highest for suspensions with the smallest mean particle size. In a separate study a correlation was developed relating rheology to overall fines concentration for the carrier fluid of industrial mature fine tailings samples (Sanders & Gillies, 2012). The rheology measurements in this study were highly scattered. The results of the studies by Adeyinka et al. (2009) and Sanders & Gillies (2012) suggest that slurry viscosity is dependent on unmeasured parameters, such as the water chemistry and solids mineralogy (Shook et al., 2002).

Separate studies have shown that the most important factors responsible for the rheological behaviour of the carrier fluid are fines concentration, solids mineralogy, and water chemistry (Shook et al., 2002). Shahmirzadi (2012) suggests that these three factors are also important in determining both the type and strength of particle interactions for suspensions. Fine solids present in oil sands materials include inert, non-interacting particles, as well as fine agglomerating minerals (Adeyinka et al., 2009; Kaminsky et al., 2009).

Aggregating solids suspended in water display remarkably different rheological behaviour than suspended inert solids. Agglomerating particles interact and join together in networks referred to as flocs and aggregates (Michaels & Bolger, 1962). Michaels and Bolger (1962) indicate that flocs and aggregates, not individual particles, are responsible for the unique flow behaviour seen for suspensions of agglomerating particles. It is desirable to relate rheological behaviour to aggregate concentration, which reflects physical changes in slurry samples such as fines concentration, water chemistry, and mineralogy.

Michaels & Bolger (1964) studied the effect of pH on clay suspensions. It was demonstrated that at lower pH values, clay slurries flocculated, forming dense aggregate structures. As pH was increased particle deflocculation occurred, decreasing suspension rheology. Shahmirzadi (2012) studied the aggregation of clay suspensions and also showed decreasing aggregate concentration for elevated pH values. Zbik et al. (2008) and Shahmirzadi (2012) both showed that the addition of calcium ions drastically increased aggregate size and concentration. Work by Shahmirzadi (2012) sought to relate the rheological behaviour of fine particle suspensions to aggregate concentration. Experiments completed with idealized aggregating kaolinite slurries showed a clear relationship between aggregate concentration and rheology.

Oil sands slurry samples pose a unique challenge with regard to rheological measurement. The presence of bitumen, a wide variety of solid species

(Kaminsky et al., 2009), and fluctuations in water chemistry will cause changes to particle interactions, the resulting aggregate behaviour, and finally, carrier fluid viscosity. Further work is required to incorporate how aggregate concentration changes for slurries seen in industrial settings. In order to relate rheology to aggregate size and concentration for industrially relevant results, measurements must be made on slurry carrier fluid in its natural, aggregated state.

1.3. Project Objectives

Due to the difficulties and time involved in measuring rheological behaviour for industrial slurry carrier fluid, a continuous medium comprised of fine particles in a suspending liquid, it is desirable to develop a method to accurately predict the rheology of these complex materials. The objectives of this research project are to:

- Measure the rheological behaviour of carrier fluid for industrial slurries
- Correlate carrier fluid viscosity with aggregate size and concentration
- Develop a method that can be used industrially to infer carrier fluid rheology from aggregate size analysis that is independent of water chemistry and solids mineralogy

In order to meet these project objectives, the following activities were completed:

- Preparation of raw samples to isolate the carrier fluid from a variety of industrial oil sands slurries
- Rheological measurements using a concentric cylinder rheometer to determine the viscosity of carrier fluid samples
- Automated image analysis using a flow particle image analyzer to determine carrier fluid aggregate size, shape and concentration
- Analytical testing to determine sample composition and water chemistry

2. Background

2.1. Carrier Fluid Rheology

2.1.1. Current Methods for Determining Carrier Fluid Rheology

The SRC Two-Layer Model is widely used for pipeline design and operation in the oil sands industry (Shook et al., 2002; Sanders et al., 2004). In the model, sand slurries are considered to be comprised of two components – coarse settling particles, and a pseudo-fluid called the carrier fluid containing fines and the suspending liquid (Sanders & Gillies, 2012). Fine non-settling particles in the carrier fluid contribute fluid-like or viscous friction, allowing the carrier fluid to be considered a continuous medium (Shook et al., 2002). The viscosity of the carrier fluid is a critical input to the SRC Two-Layer Model. Predictions of pipeline pressure loss and minimum operating velocity are sensitive to the carrier fluid viscosity (Sanders & Gillies, 2012). Carrier fluid rheology is necessary for the proper design and operation of slurry pipelines and process equipment but it is rarely measured in industrial settings (Schaan, 2011).

Measurements of slurry rheology may be made using various methods, including capillary or pipe flow testing and rotational rheometry (Liu & Masliyah, 1996; Mewis & Wagner, 2012). Rheological measurement of the carrier fluid requires extensive and sometimes difficult preparation that includes separation of the coarse solids fraction, and bitumen removal. Tests are time consuming and cannot be made on-line. Even though carrier fluid viscosity should be measured directly (Sanders & Gillies, 2012), empirical correlations are often employed to obtain

estimates of this important parameter because of the difficulties inherent in measuring the carrier fluid rheology (Schaan, 2011). Correlations generally relate the carrier fluid rheology to the volume concentration of fine solids in the carrier fluid. This means that on-line measurement of the size distribution and concentration of fine particles can be used to give an indication of the carrier fluid viscosity. Problems arise because correlations have been developed for a single material or under a specific set of conditions. The physical properties of oil sands slurries are highly variable (Masliyah et al., 2011) and rheology of the carrier fluid depends on many factors that change frequently during processing, such as solids concentration, water chemistry and mineralogy (Shook et al., 2002; Sanders & Gillies, 2012). This limits the usefulness of correlations based only on fines concentration. It is necessary to incorporate key physical properties of the carrier fluid into future correlations or to determine rheology using a parameter that reflects changes in slurry composition and water chemistry. The physical properties of the carrier fluid will not only determine rheological behaviour, but also particle interactions which may be observed by studying the aggregation of the fine particles. As a result aggregate size and concentration could be used to help predict the rheological behaviour of carrier fluid.

2.1.2. Carrier Fluid Rheology and Particle Aggregation

Shook et al. (2002) identified that the most important factors responsible for the rheological behaviour of carrier fluid: fines concentration, solids mineralogy, and water chemistry. These factors will determine the type and strength of particle interactions within the fluid. Salama & Mikula (1996) stated that slurry behaviour is strongly associated with the strength of particle interactions or the prevalence of particle aggregation. Individual or primary particles may agglomerate to form dense flocs. Michaels & Bolger (1962) assert that flocs, not primary particles, are the basic structures contributing to the behaviour of suspensions. These flocs can form larger formations called aggregates. Figure 2.1 illustrates the relationship describing effective solids concentration for systems containing the same concentration of primary particles with different degrees of aggregation.

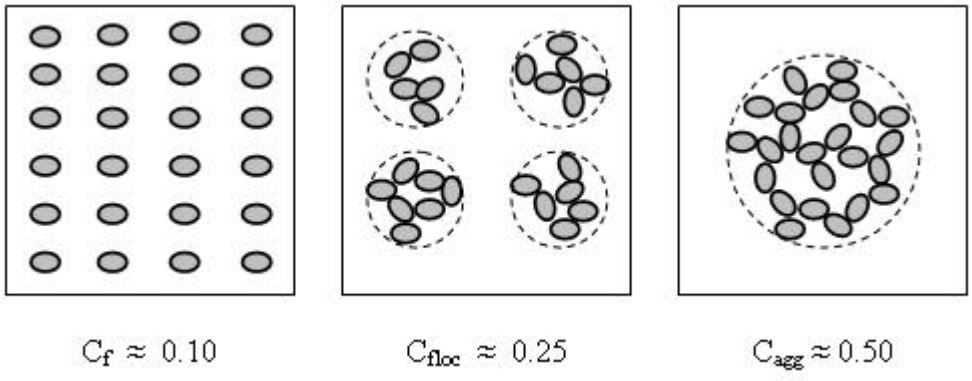

Figure 2.1: Particle configurations in aggregating systems.

It can be seen for this imagined system that the formation of aggregates could increase the apparent particle concentration by as much as five times. Aggregation

also increases viscosity. Shook et al. (2002) show that slurries containing aggregating particles have higher values of viscosity than those with fully dispersed particles at the same overall solids concentration. Figure 2.1 illustrates that the loose formation of an aggregate traps water interstitially, isolating the water from the bulk suspension fluid and resulting in an aggregate concentration greater than the true solids content (Broughton & Windebank, 1938). Studies by Michaels and Bolger (1964) saw that for some aqueous kaolin slurries, aggregates contained as little as 10% solids by volume but had elevated viscosity and yield stress values. Clearly, it is necessary to characterize the aggregate behaviour for a system, rather than the behaviour of individual particles, in order to model its true rheological properties. If one was unwilling or unable to measure rheology directly, it seems that aggregate size and concentration could potentially be measured on-line allowing for real time prediction of rheological behaviour.

The degree of particle aggregation in the carrier fluid depends on the same parameters as those responsible for rheological behaviour: overall fines concentration, the solid species present, and the chemistry of the suspending water. The size distribution and composition of the solids fraction of the carrier fluid may change frequently depending on the source of ore (Masliyah et al., 2011). Oil sands solids are comprised primarily of silica sands (82%), with the remainder made up of clays (14%) and other trace minerals (Masliyah et al., 2011). The fine particles which are present in the carrier fluid are mainly silica and clay species like kaolinite and illite (Adeyinka et al., 2009; Masliyah et al.,

2011). Fine silica sand particles (d < 74 μm) are relatively inert and as a result make a relatively small contribution to carrier fluid viscosity (Shahmirzadi, 2012). Clays are fine, plate-like particles (Masliyah et al., 2011) that join in networks to form aggregate structures. The presence of aggregating mineral species will increase carrier fluid viscosity. This behaviour was shown by Adeyinka et al. (2009) who observed lower viscosity values for samples containing higher sand to clay ratios at equal solids volumes. Shahmirzadi (2012) demonstrated experimentally that aggregating clays contribute more to carrier fluid viscosity than equal volumes of fine sand particles.

For clays, the size and concentration of aggregates is determined by the strength of particle interactions (Michaels & Bolger, 1964) which vary from species to species. The surface charge of the particles determines whether attraction or repulsion will occur between clay surfaces. This behaviour, referred to as electrostatic interaction, causes agglomerating particles to aggregate or disperse. Hao (2008) explains that attractive electrostatic interactions between particles in suspension contribute to increased aggregation and overall viscosity. Water ion content and pH can alter the surface charge of clay particles affecting aggregation (Masliyah et al., 2011). The types of clays present will also change the electrostatic interactions in a carrier fluid sample. Kaminsky et al. (2009) examined the clay species found in oil sands materials. Figure 2.2 shows the composition of clays found in a typical oil sands tailings sample.

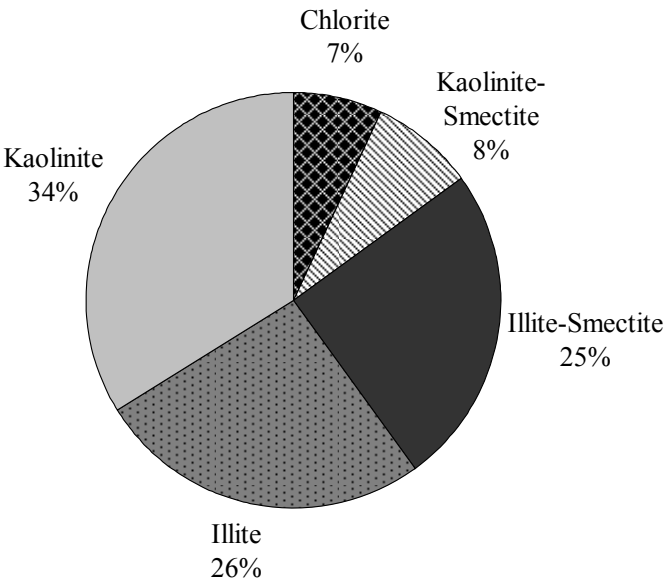

Figure 2.2: Relative composition of clay species in an oil sands tailings sample (Kaminsky et al., 2009).

Kaolinite is the dominant clay species found in oil sands materials (Adeyinka et al., 2009; Kaminsky et al., 2009; Masliyah et al., 2011) and is used here to illustrate clay surface charge. The basal-plane or face of a kaolinite particle has a permanent negative charge, while the edges of the particle have a charge that is dependent on the surrounding water chemistry and pH (Michaels & Bolger, 1964). At acidic pH values the edges are positively charged, causing stronger attractions between particles (Miller et al., 2007). This increases aggregation and the resulting clay suspension viscosity (Michaels & Bolger, 1964). At elevated (more alkaline) pH values the edges are negatively charged (Miller et al., 2007).

This causes repulsion between particles, hindering aggregation of the particles and lowering sample viscosity (Michaels & Bolger, 1964).

The surface charge of the particles also changes with the dissolved ions in the suspending liquid (Michaels & Bolger, 1964). Clays in ionic solutions experience isomorphic substitution, where ions in solution replace those within the crystal structure of the clay, creating a surface charge on the particle (Masliyah et al., 2011). In the absence of dissolved ions, clays are highly flocculated at low pH values (Michaels & Bolger, 1964) causing increased viscosity. For alkaline suspensions there is even less attraction between clay particles, thus reduced aggregation and viscosity (Michaels & Bolger, 1964; Shahmirzadi, 2012). The addition of divalent cations (like dissolved calcium) causes kaolinite basal planes to undergo isomorphic substitution (Masliyah et al., 2011) reducing the negative surface charge. Under acidic conditions, this decreases edge-to-face attraction, reducing aggregation and resulting viscosity values (Michaels & Bolger, 1964). Different clay species will exhibit varying levels of isomorphic substitution (Masliyah et al., 2011). This means the change in surface behaviour due to the addition of cations will vary from species to species.

Experimental work has been completed to examine the aggregation of fine particles with respect to water chemistry. Coussot & Piau (1994) observed a strong relationship between pH and flow behaviour. Michaels & Bolger (1964) suggest that at lower pH values, kaolinite slurries are highly flocculated, with the

particles forming small dense structures. As pH is increased, particle deflocculation occurs and viscosity decreases. Rand & Melton (1977) measured the rheological behaviour of kaolinite slurries at a concentration of 9% by mass. A 33% decrease in Bingham plastic viscosity was seen as pH was increased from 6 to 9. Shahmirzadi (2012) examined the effect of pH and ion content for aqueous kaolinite suspensions. Comparison of samples at pH 4 and pH 9 showed that both aggregate concentration and viscosity were lower at the higher pH. At a clay concentration of 5% by volume, the viscosity at pH 4 was nearly double the value measured at pH 9. Shahmirzadi (2012) also showed that the addition of calcium ions drastically increased aggregate size and concentration, as well as viscosity. Zbik et al. (2008) investigated the effect of calcium ions on kaolinite slurries and also showed that particle aggregation increases, resulting in increased settling rates and higher suspension viscosity.

2.1.3. Existing Correlations for Carrier Fluid Viscosity

When examining the viscosity of solid liquid mixtures, it is typically relative viscosity which is discussed. Relative viscosity is defined as the ratio of mixture viscosity to the viscosity of the suspending liquid (Liu & Masliyah, 1996). This relationship is given as:

$$\mu_r = \mu/\mu_L \qquad \textbf{(2.1)}$$

where μ_r is relative viscosity, μ is mixture viscosity and μ_L is the suspending liquid viscosity.

There have been extensive efforts to characterize the rheological behaviour of solid-liquid suspensions. The simple but theoretical model derived by Einstein provides the following relationship between relative viscosity (μ_r) and solids volume fraction (C) (Shook et al., 2002):

$$\mu_r = 1 + 2.5C \qquad \textbf{(2.2)}$$

Einstein's relationship was developed for rigid, non-interacting, spherical particles in dilute suspensions. At solids concentrations greater than 1-5% by volume, there is some degree of particle interaction which causes a divergence from the Einstein equation (Broughton & Windebank, 1938). For fine, agglomerating particles, this means deviations from Einstein's equation will occur even at very low solids concentrations (Broughton & Windebank, 1938). Einstein's equation is most certainly not appropriate for industrial oil sands carrier fluid where solids concentrations are high, particles are poly dispersed and non spherical, and aggregation may occur.

Work by D.G. Thomas (1965) sought to expand on the Einstein equation in order to predict the viscosity of more concentrated suspensions. An empirical relationship was developed using the measured viscosity of a variety of

suspensions. The experimental data include suspensions composed of non-interacting materials such as polystyrene, rubber latex, glass, and methyl methacrylate and solids content of up to 75% by volume. Particle diameter ranged from 0.099 to 435 μm. It was noted that as solids concentration increased there were two additional contributions to suspension viscosity that must be considered. A second order term was added to the Einstein equation to account for hydrodynamic forces, the interaction between particles and the surrounding fluid. An exponential term was added to account for interactions between particles. For very small flocs and aggregates the viscosity contribution of hydrodynamic forces will be negligible. However, due to increased aggregation the contribution due to particle interactions will be quite significant.

Many attempts have been made to predict the rheological behaviour of industrial slurries. Exponential relationships have been used frequently to predict viscosity in order to account for the strong particle interactions in aggregating clay slurries. A study conducted by A.D. Thomas (1999) examined the rheology of fine particle slurries produced from mineral ores. The relationship between suspension viscosity and fines concentration developed by A.D. Thomas (1999) is:

$$\mu_r = \exp\left(\frac{C_f}{BC_{max.}}\right) \qquad \textbf{(2.3)}$$

where $C_{max.}$ is the maximum packing concentration of the particles. B is an experimentally determined constant, which demonstrates the importance of

completing rheology measurements. Experimental data is required to determine the correlation coefficient, which is an indicator of the strength of particle interactions.

Measurements were made of the viscosity of Syncrude mature fine tailings (Shook et al., 2002). The experimental data obtained were fitted to an exponential function determine the relationship between carrier fluid viscosity and fines concentration for samples containing 10 to 30% solids by volume, given as:

$$\mu_r = \exp\left(12.5C_f\right) \quad \textbf{(2.4)}$$

Equation 2.4 is frequently used in the design of slurry pipelines and process vessels (Schaan, 2011); however, Sanders & Gillies (2012) suggest that this correlation should be used only as an estimate of carrier fluid viscosity due to fluctuations in slurry composition and water chemistry. It is not possible to know if the properties of the suspension being considered will be similar to those of the MFT for which the correlation was developed. The scattered data obtained during the original testing of the MFT only emphasizes the importance of making measurements of carrier fluid viscosity as the most preferred choice, or alternatively using a correlation that takes into consideration the most important parameters: concentration, sample mineralogy and water chemistry.

Shahmirzadi (2012) sought to relate the concentration of aggregated structures to relative viscosity for idealized carrier fluid samples. The viscosity, aggregate size and aggregate concentration were measured for aqueous kaolinite suspensions. Solids concentration and water chemistry were varied and an attempt was made to correlate aggregate concentration to rheological data. The ratio of aggregate to fines concentrations was found by comparing aggregated samples to those in a generally dispersed state at pH 9. Higher viscosity values were seen under conditions favourable to aggregation. Overall results indicated that for an idealized kaolin-water carrier fluid, viscosity depended only on the aggregate concentration of samples, and was not affected by water ion content or pH. Shahmirzadi (2012) also briefly examined changes carrier fluid viscosity with the addition of fine sand particles. The fine sand particles did not appear to aggregate and contributed less to overall viscosity than equal volumes of clay.

This project seeks to build upon the previous work by Shahmirzadi (2012) to study aggregate concentration and carrier fluid rheology for industrial (real) slurries. Aggregates in industrial slurries are expected to behave differently than those seen in idealized samples due to residual bitumen on particle surfaces, the wide variety of solid species, and fluctuations in process water chemistry.

2.2. Rheology

2.2.1. Measurement Techniques

Two of the more common techniques for the measurement of carrier fluid rheology are capillary/pipe flow testing and rotational rheometry (Mewis & Wagner, 2012). Concentric cylinder rheometry, the method used in this study, is a particularly effective technique because tests are conducted using a relatively small amount of sample (Mewis & Wagner, 2012). Various geometries can be utilised to measure viscosity, including: cone and plate, parallel plate, and concentric cylinder configurations (Mewis & Wagner, 2012). Cone and plate and parallel plate geometries are not suitable for the measurement of slurry rheological behaviour when larger particles or aggregates are present (Mewis & Wagner, 2012). Larger particles may settle during testing and the resulting concentration gradient gives the appearance of lower slurry viscosity (Mewis & Wagner, 2012). Ideally particles do not settler or at least must settle slowly in order to measure rheological behaviour (Shook et al., 2002).

Concentric cylinder rheometers operate on the principles of Couette flow (Shook et al., 2002). For this geometry, a spindle is allowed to freely rotate within a fixed cup. The speed of the spindle is controlled, and the torque response is measured. Figure 2.3 shows a schematic illustration of a concentric cylinder rheometer. The spindle shown has a conical end, the shape of which has been exaggerated here for the sake of illustration. R_1 is the spindle radius, R_2 is the cup radius and L is

the length of the spindle in the field of measurement. The angular velocity or spindle speed of the system is given by ω.

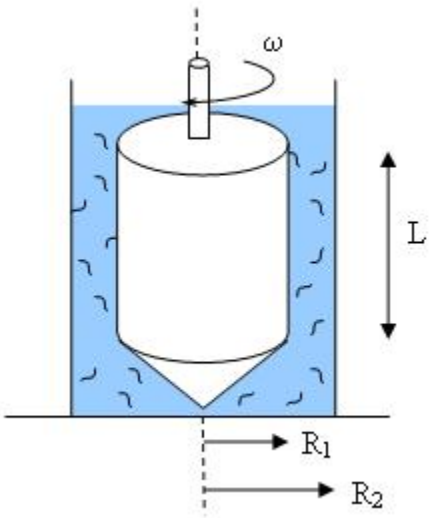

Figure 2.3: Schematic illustration of a concentric cylinder rheometer.

In order to obtain meaningful results, samples must be sheared at low enough speeds such that laminar (purely viscous) fluid flow occurs (Shook et al., 2002). If the fluid is sheared at excessively high speeds, a secondary, ordered flow known as Taylor vortices may occur (Bird et al., 2002). This results in an apparent viscosity that is higher than true values for the material (Shook et al., 2002). For some samples, which exhibit a property referred to as yield stress, a minimum torque must be applied to the sample in order for the sample to be fully sheared across the gap between cylinders (Shook et al., 2002). Shear stress does not change linearly with shear rate in this flow regime (Shook & Roco, 1991). Care must be taken to ensure all measured data are analyzed only at spindle speeds

where the sample is fully sheared and only laminar (viscous) flow occurs. Criteria for determining the limits of incomplete shearing and the onset of Taylor vortices are given in the following section.

2.2.2. Rheological Models

Dilute slurry suspensions often exhibit Newtonian behaviour (Michaels & Bolger, 1964). Newtonian fluid behaviour is characterized by a linear relationship between shear rate and shear stress for a fluid exhibiting no yield stress. The characteristic flow profile of a Newtonian fluid is shown in Figure 2.4.

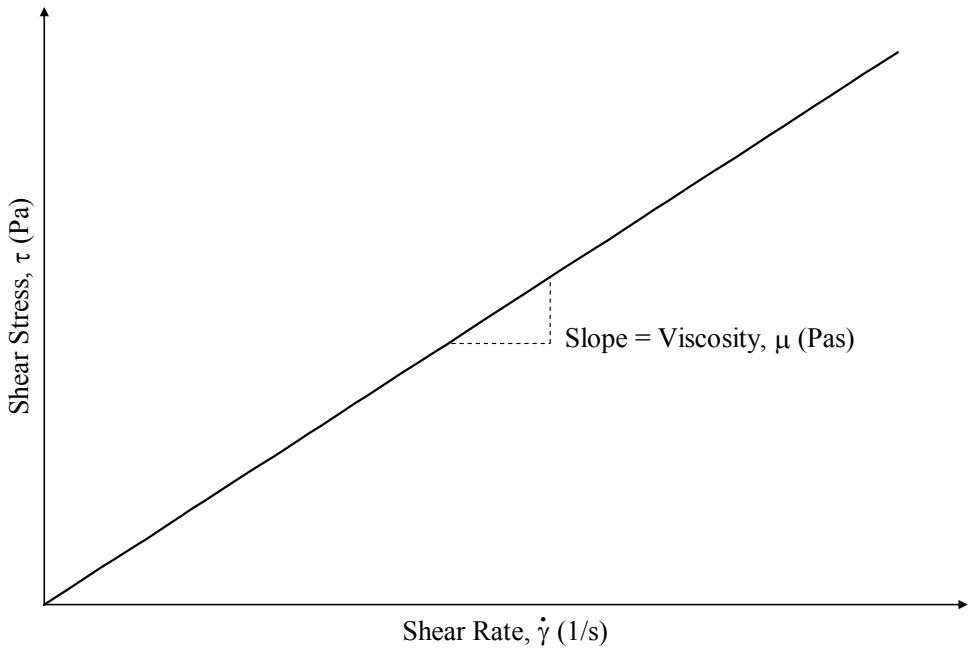

Figure 2.4: Rheological flow profile of a Newtonian fluid.

The relationship between shear rate $\dot{\gamma}$ and shear stress τ is given by Equation 2.5 for one-dimensional flow (Bird et al., 2007), where μ is the proportionality constant referred to as Newtonian viscosity:

$$\tau = \mu\dot{\gamma} \tag{2.5}$$

For concentric cylinder rheology measurements, this relationship can also be expressed in terms of angular velocity (spindle speed) ω and torque T. The relationship is (Shook et al., 2002):

$$\omega = \frac{T}{4\pi L \mu}\left[\frac{1}{R_1^{\,2}} - \frac{1}{R_2^{\,2}}\right] \tag{2.6}$$

In order to simplify this relationship, it is possible to define a system factor α that is dependent only on the system geometry:

$$\alpha = \frac{4\pi L}{\left[\frac{1}{R_1^{\,2}} - \frac{1}{R_2^{\,2}}\right]} \tag{2.7}$$

When torque response for a Newtonian fluid is normalized using a system factor α, the simplified relationship between torque and spindle speed is given by:

$$\frac{T}{\alpha} = \mu\,\omega \qquad \textbf{(2.8)}$$

At sufficiently high angular velocities, flow in the concentric cylinder rheometer is no longer purely viscous and Taylor vortices are formed. For Newtonian fluids, a test parameter may be used to determine the region of laminar flow. The maximum spindle speed for laminar flow of a Newtonian fluid is (Shook & Roco, 1991):

$$\omega_{crit.} = \frac{45\,\mu}{\left[\frac{(R_1 + R_2)}{2}\right]^{1/2} (R_2 - R_1)^{3/2}\,\rho} \qquad \textbf{(2.9)}$$

where ρ is the carrier fluid density.

More concentrated clay suspensions are expected to exhibit non-Newtonian fluid behaviour (Shook et al., 2002). The Bingham fluid model is often appropriate to describe the behaviour of clay suspensions (A.D. Thomas, 1999; Slatter & Wasp, 2002; Litzenberger & Sumner, 2004). Michaels & Bolger (1962) observed Bingham fluid behaviour for aqueous kaolin clay suspensions at concentrations of approximately 3% solids by volume while Litzenberger & Sumner (2004) found kaolin clay suspension rheology in agreement with the Bingham fluid model at solids concentrations up to 19% by volume. Bingham fluids show a linear

relationship between shear rate and shear stress and exhibit a yield stress. The characteristic flow profile of a Bingham fluid is shown in Figure 2.5.

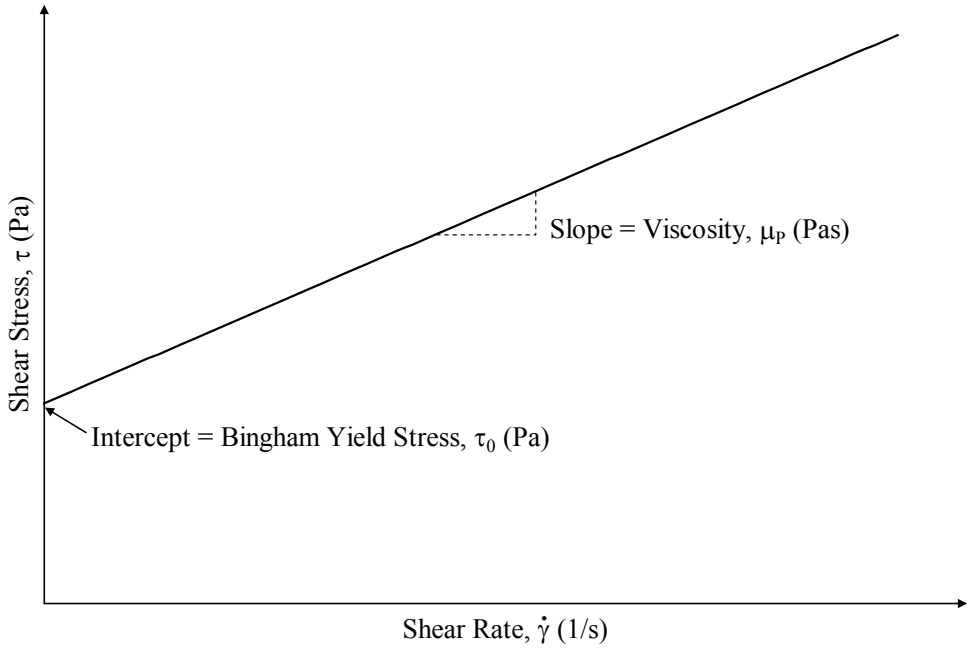

Figure 2.5: Rheological flow profile of a Bingham fluid.

The relationship between shear rate and shear stress for the Bingham fluid model is given by (Liu & Masliyah, 1996):

$$\tau = \tau_0 + \mu_P \dot{\gamma} \qquad \textbf{(2.10)}$$

The constant τ_0 represents the Bingham yield stress, or the minimum force that must be overcome in order to shear the material evenly across the gap. The proportionality constant μ_P is the Bingham plastic viscosity of the material.

This relationship can also be expressed in terms of spindle speed and torque. The Bingham fluid relationship for a concentric cylinder rheometer is shown in Equation 2.11 (Shook et al., 2002).

$$\omega = \frac{T}{4\pi L \mu_P}\left[\frac{1}{R_1^{\,2}} - \frac{1}{R_2^{\,2}}\right] - \frac{\tau_0}{\mu}\ln\left(\frac{R_2}{R_1}\right) \qquad \textbf{(2.11)}$$

When torque response for a Bingham fluid is normalized using the system factor α, the simplified relationship between torque and spindle speed is:

$$\frac{T}{\alpha} = \mu_P\ \omega + \tau_0\ \ln\left(\frac{R_2}{R_1}\right) \qquad \textbf{(2.12)}$$

For Bingham fluids, yield stress must be exceeded in order for laminar flow to occur evenly across the gap (Shook et al., 2002). If the fluid stress has not exceeded this minimum force, incomplete shearing will occur (Shook et al., 2002). The minimum torque response required to ensure fluid is fully sheared is (Shook et al., 2002):

$$T_{min} = 2\pi L \tau_0\ R_2^{\,2} \qquad \textbf{(2.13)}$$

While Taylor vortices can also occur in fluids exhibiting Bingham plastic behaviour, there is no set criterion by which to determine the onset of secondary

flows for non-Newtonian fluids in Couette flow (Bird et al., 2002). However, Equation 2.9 has been used as an estimate for the onset of Taylor vortices for Bingham fluids (Litzenberger & Sumner, 2004).

2.3. Particle Size and Shape Analysis

2.3.1. Measurement Techniques

In order to characterize oil sands ore, an assessment is typically made of the solid particle size distribution. The size distribution is used to identify fines content, coarse solids content, and the grade or quality of the ore (Masliyah et al., 2011). Fines content must be known in order to use existing carrier fluid viscosity correlations; however the size distribution of fine particles also has a strong effect on carrier fluid viscosity. Michaels & Bolger (1964) have noted that suspension rheology is dependent not just on particle concentration, but also on shape, mean particle size and the size distribution. Fine particle aggregation tendencies increase strongly as primary particle diameter decreases (Michaels & Bolger, 1964). It has been previously noted that aggregation increases carrier fluid viscosity, indicating that knowledge of aggregate size and concentration is key to understanding carrier fluid flow behaviour. The development of a correlation that relates viscosity to aggregate properties or the factors affecting aggregation could lead to more accurate prediction of carrier fluid viscosity. In this study, the particle size distribution (PSD) of carrier fluid was measured for samples in both dispersed and aggregated states.

Particle sizing may be done using direct methods that provide quantitative results from measurement, or indirect methods that allow particle size information to be inferred from results (Shook et al., 2002). Current industrial practice for solids size analysis includes indirect methods like sedimentation tests and direct measurement techniques like sieving, as well as microscopy and other optical techniques (Shook et al., 2002).

Sieving is frequently used in characterizing particle size (Salama & Mikula, 1996). Sieves come in a wide variety of mesh sizes and can be easily used to determine the size distribution of samples. Sieving may be done with solids in suspension or with solids dried prior to testing. Dry sieving is limited in that it cannot give information about the aggregated structures that are responsible for changes to the carrier fluid viscosity. Wet sieving does provide information about the aggregate structures, however frequent plugging of the sieves occurs at smaller mesh sizes, especially in the presence of bitumen. Due to these testing constraints, sieving is not appropriate for particle size measurement in this study.

Gravity sedimentation tests are also used to determine a mean particle size for a slurry sample. During sedimentation testing, a measured amount of slurry sample or solids are allowed to settle and the solids-water interface is monitored. The slurry sedimentation rate is measured and from this the mean particle diameter d can be calculated using Stokes Law, given in Equation 2.14 (Shook et al., 2002):

$$d = \left[\frac{18 \mu_L u_\infty}{g(\rho_S - \rho_L)} \right]^{1/2} \quad \textbf{(2.14)}$$

The particle sedimentation velocity is denoted by u_∞, g is gravitational acceleration and ρ_S and ρ_L are the densities of the solids and liquid respectively.

Michaels and Bolger (1964) conducted sedimentation tests for aqueous kaolin slurries with a variety of water chemistries to examine settling behaviour. Testing showed that viscosity increased with overall floc size and concentration, moving from Newtonian to increasingly non-Newtonian rheological behaviour. Although sedimentation effectively gives a mean particle size, that value may not be particularly representative for samples with wide size distributions or irregularly shaped particles. As a result, this method is not ideal for oil sands slurries.

Many optical methods can be used to and determine size and shape parameters for particle entities. One popular method, scanning electron microscopy (SEM), can provide high quality images for extremely small particles (Salama & Mikula, 1996). Cryo-SEM is a technique that involves freezing particles in their hydrated form before testing, allowing aggregates to be examined as they appear in suspension. Zbik et al. (2008) examined the size, shape, and aggregating characteristics of aqueous kaolinite suspensions using cryo-SEM. Although electron microscopy can provide accurate information about aggregate properties, only a small number of aggregates may be examined per test. This is unlikely to

give results representative of carrier fluid samples, which may contain aggregates in a wide range of shapes and sizes. Electron microscopy requires extensive and time-consuming sample preparation that makes it poor choice for use in industrial settings where PSD measurements are required frequently and quickly.

Automated particle image analysis can offer a technological advantage over other optical methods due to its ability to analyze a large number of images of particle entities while requiring relatively small amounts of sample. Flow image analysis is useful because it allows one to study particles in their aggregated state. Flow cytometry is one type of automated image analysis that has previously been used in medical fields for the characterization of cells and proteins (Macey, 2007). The novel technique can measure multiple parameters simultaneously (Macey, 2007) allowing for simple shape and size analysis of a large number of particles. The device used in the current study is the Flow Particle Image Analyzer (Sysmex FPIA-3000) by Malvern, which utilises flow cytometry technology. Figure 2.6 illustrates liquid flow through the device.

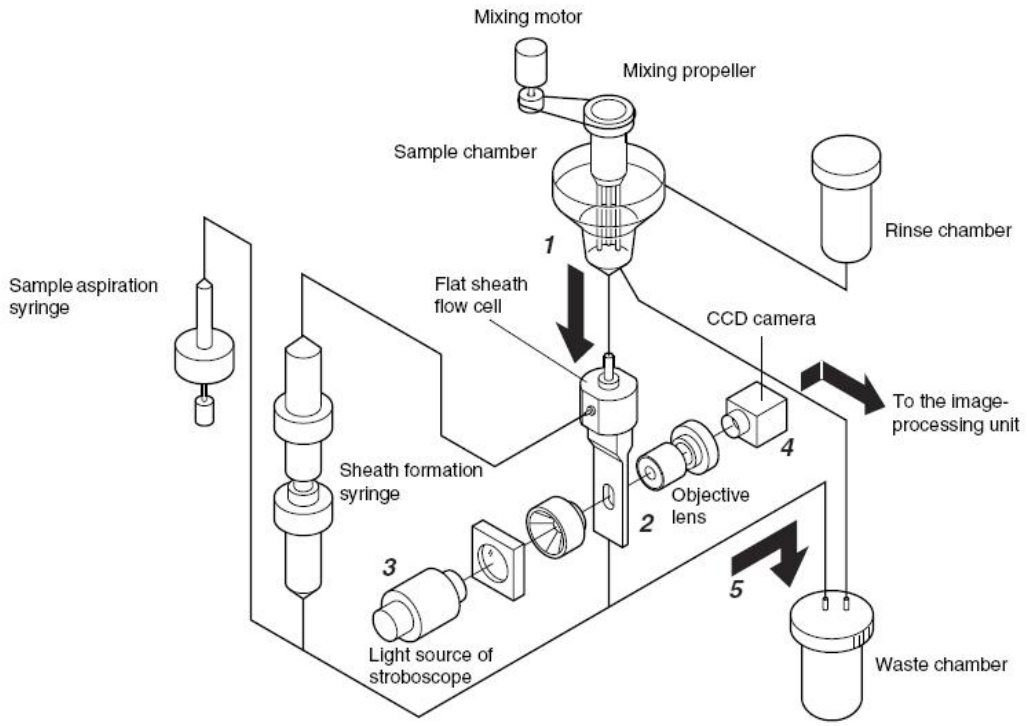

Figure 2.6: Fluid flow through the Sysmex FPIA-3000 (from Symex Corporation, 2008).

Sample is injected to the mixing chamber (1) where it is then oriented into a flat sheath flow and sent into the test field (2). Samples are illuminated by a light source (3) and images of each particle or entity are captured by a camera (4) and saved for analysis. After testing, the sample is rinsed from the device into a waste collection chamber (5).

Limited studies have been conducted using the FPIA. Komabayashi & Spangberg (2008a) used the device to determine the size and shape of dental materials. The Flow Particle Image Analyzer was selected for use in that study due to its rapid imaging capabilities. Komabayashi & Spangberg (2008b) also used the FPIA-

3000 to examine samples with similar mineralogy and found that the images generated did not allow one to easily distinguish one species from another, although size and shape differences could be observed for the different species. Shahmirzadi (2012) examined aqueous kaolin suspensions using the FPIA-3000 and successfully measured the size and concentration of aggregate structures.

A major advantage of the FPIA-3000 is its ability to provide consistent particle orientation. When particles are measured at the same orientation the relative size and distribution between particles is more accurately determined. Many devices, including the Mastersizer, lack the ability to select or control particle orientation. Besendorfer & Roosen (2008) compared shape distributions of mono-sized ceramic suspensions using the Mastersizer and FPIA-3000. Potential particle orientations were verified using SEM micrographs. The authors found that samples tested in the Mastersizer displayed wider PSDs indicating that particle orientation was random and that no consistent alignment could be achieved. The same samples tested in the FPIA-3000 resulted in narrower PSDs as well as narrow shape distributions. This indicates a consistent alignment for the particles tested. Random orientation leads to less reliable size and distribution information for a sample, as a result the FPIA-3000 was selected for use in this study.

3. Experimental Methods

3.1. Materials

3.1.1. Oil Sands Extraction Slurry Materials

The industrial slurry samples used in testing were obtained from a number of sources which are detailed below. A summary of the samples tested is given in Table 3.1.

Shell Canada provided samples from an extraction plant in Fort McMurray, AB. The extraction process used by Shell has been described by Masliyah (2010). Oil sands ore is processed in a manner similar to that shown in Figure 1.1, however tailings are processed in additional stages. Tailings from flotation stages are sent through cyclones which separate the coarse tailings (underflow) from the remaining fine material (overflow). The fine tailings are treated with polymer flocculants then pass through mechanical thickeners. Both coarse and thickened fine tailings are moved by pipeline to tailings settling ponds for storage. Fine solids and water removed from the bitumen froth are treated with a paraffinic solvent to recover any residual bitumen. Following this stage, these fine tailings are sent to the solvent recovery unit, where the solvent is recovered. These tails are also sent to the tailings settling ponds. Over a period of time, much of the solid material will settle at the bottom of the ponds, while ultra-fine solids remain suspended. The non-settling portion of the suspension is referred to as mature fine tailings.

Suncor Energy provided samples from an extraction plant in Fort McMurray AB. The extraction process used by Suncor has been described by Masliyah (2010). Suncor processes ore using the method shown in Figure 1.1 with additional flotation, froth treatment and tailings treatment stages. The hydrotransport slurry passes through three stages of flotation. Each flotation cell produces bitumen froth, middlings and a tailings underflow. The underflow from the third (tertiary) flotation cell is referred to as final tailings. Tailings from froth treatment stages are processed through a centrifuge (Cleyle, 2013). The centrifuge feed is separated into three streams: the discharge light phase (diluted bitumen), nozzle discharge (nozzle water, an aqueous stream containing fine solids), and the discharge heavy phase (ring dam water, a tailings stream).

Syncrude Canada Ltd. provided samples from a pilot-scale extraction plant in Edmonton AB. The pilot scale facility is a simplified version of the process shown in Figure 1.1. Ore is combined with water and then passed through a hydrotransport pipeline loop. The slurry is processed by a separation cell where bitumen froth, middlings and tailings streams can be recovered.

Total E&P Canada provided tailings from a batch extraction unit (T-T). Examples of this type of device have been used by Sanford & Seyer (1979) and Zhou et al. (2004) to perform laboratory extraction experiments. In these devices, ore is combined with warm water, then mixed and aerated to produce froth. The froth

phase is removed by skimming from the top of the mixing vessel, leaving an aqueous tailings phase behind.

Table 3.1: Industrial extraction and tailings slurry sample descriptions.

Sample ID	Description
S-M	Shell middlings stream from gravity separation in Primary Separation Cell (PSC).
S-MFT	Shell mature fine tailings (MFT) from tailings storage ponds.
S-TSRU	Shell flotation tailings by the Solvent Recovery Unit to remove residual hydrocarbon materials.
S-TT	Shell flotation tailings thickened using polymer flocculants.
SU-M	Suncor middlings from primary separation cell.
SU-NW	Suncor nozzle water (nozzle discharge) from centrifuge.
SU-RDW	Suncor ring dam water (heavy discharge) from centrifuge.
SU-T	Suncor tailings (underflow) from primary separation cell.
SU-TF	Suncor tailings (underflow) from tertiary floatation cell.
SU-TPSC	Suncor tailings (underflow) from primary separation cell (sample collected separate from sample SU-T).
SU-TSF	Suncor tailings (underflow) from the secondary flotation cell.
SY-HT	Syncrude hydrotransport slurry from pilot scale extraction.
SY-M	Syncrude flotation middlings from pilot scale extraction.
SY-T	Syncrude flotation tailings from pilot scale extraction.
T-T	Total tailings from a bench-scale batch extraction unit.

Large quantities of each sample were provided for testing. Due to natural variances in the slurry samples and differences in collection methods, the total volume of slurry required for testing was separated from the bulk sample. This portion was mixed thoroughly prior to preparation for testing. The overall composition of each raw sample was determined using Dean Stark laboratory analysis.

3.1.2. Reusable Hydrocarbon Sorbent (RHS) Beads

Reusable hydrocarbon sorbent (RHS) beads provided by Gradek Energy Inc. were utilised to remove bitumen from the slurry samples. Bitumen removal was required in order to prevent equipment clogging and damage during particle size measurement. The spheroid RHS beads are smooth surfaced and made from a hydrophobic polymer. The oleophilic or "oil loving" nature of the beads allows hydrocarbon droplets to adhere to the bead surface in an aqueous environment. The beads are buoyant in water with density ranging from 80-350 kg/m^3 and a characteristic length between 12 and 20 mm (U.S. Patent No. 2010/0072110 A1). The average diameter of the beads is 17 mm with a typical density of 250 kg/m^3. Figure 3.1 shows a close-up image of the RHS beads.

Figure 3.1: Reusable Hydrocarbon Sorbent (RHS) beads.

In studies commissioned by Gradek Energy, use of the RHS beads was optimised for maximum bitumen removal (CanmetENERGY, 2003). Bitumen recovery increased with repeated exposures to fresh RHS beads, with maximum bitumen recovery seen after six loads of beads. Removal of bitumen also increased with a rise in temperature from 20°C to 45°C. Maximum bitumen recovery was achieved between 45 and 60°C. As a result, bead treatment was conducted at 45°C and slurry samples were treated with six loads of beads at a beads-to-bitumen mass ratio of 6:1 for each loading cycle. Beads were removed after each cycle and stored for regeneration. Beads loaded with bitumen are shown in Figure 3.2.

Figure 3.2: Spent RHS beads.

After each use the RHS beads were regenerated by washing with a solvent. Studies completed on behalf of Gradek Energy (CanmetENERGY, 2003) indicated that common laboratory solvents such as toluene cause damage to the beads preventing re-use. In order to avoid excessive wear, the beads were regenerated using household Coleman naphtha Camp Fuel. Beads were rinsed under the fume hood using naphtha, and wiped with adsorbent paper until no hydrocarbon residue remained. Beads were left in the fume hood until appearing completely dry, and then heated in a vacuum oven at 75°C for ten minutes to remove any residual naphtha. Figure 3.3 shows the RHS beads after regeneration.

Figure 3.3: RHS beads after regeneration.

3.2. Sample Preparation

3.2.1. Apparatus

The coarse fraction and larger bitumen droplets in the slurry samples were removed using a metal sieve (Fisherbrand U.S. Standard Stainless Steel Test Sieve, Thermo Fisher Scientific, Waltham, MA, USA) with 75 μm square openings (Tyler No. 200). The sieve was loaded with well-mixed slurry and shaken by hand, allowing fine particles and fluid to pass through the sieve into a metal receptacle. The typical fines cut-off of 44 μm (Tyler No. 325) was not used because bitumen droplets cause excessive plugging at this mesh size (Sanders & Gillies, 2012).

After sieving, all slurry samples were treated with reusable hydrocarbon sorbent (RHS) beads to remove residual bitumen. A water bath was used to heat slurry samples and RHS beads. The heating function of a magnetic stirring device (RCT basic IKAMAG safety control, IKA-Werke GmbH & Co., Staufen, Germany) was utilised to heat 600 mL of municipal tap water in a 1500 mL Pyrex beaker. The magnetic stirrer can operate at temperatures between 0 to 310°C and mix at speeds from 0 to 1500 RPM. The water bath temperature was measured using a digital thermometer and kept at a temperature of approximately 45°C. Figure 3.4 shows the magnetic stirrer and water bath.

Figure 3.4: Magnetic stirrer with water bath.

A rotating mixer (Rotary Tumbler Model 3-1.5B, Lortone Inc., Mukilteo, WA, USA) was used to mix heated samples with the RHS beads. A glass jar was used for mixing as the rotating mixer canisters were not suitable for the required experimental temperature. The one litre glass canning jar rotated at a speed of 70 RPM. The jar allowed for mixing to occur at elevated temperatures without the seal being compromised. Due to the buoyancy of the RHS beads, a metal baffle

was placed in the jar to ensure beads were submerged into the sample during mixing. Figure 3.5 shows the rotating mixer set up.

Figure 3.5: Modified rotating mixer used in bitumen removal.

Residual naphtha was removed from the RHS beads using a vacuum oven (GCA Corp. Precision Vacuum Oven, Ogden Manufacturing, Pittsburgh, PA, USA). The oven can operate at temperatures up to 200°C and at vacuum pressures ranging from 0 to 100 kPa. Beads were dried in a Pyrex beaker.

The water needed for (i) sample dilution and (ii) suspending liquid rheology measurements was obtained by filtering solids out of a portion of the bead treated

carrier fluid samples. The filtration equipment included a Buchner funnel with a rubber seal, filter paper with 2.5 μm openings (Qualitative 5 150 mm cellulose filter paper, Whatman Ltd., Little Chalfont, UK) assembled over a side-arm filtration flask connected to a rubber hose. The hose was attached to a faucet aspirator vacuum pump (NALGENE 6140 vacuum pump (aspirator type), Thermo Fisher Scientific, Rochester, NY, USA). Water flows continuously through the three-way device and is discharged into a drain inducing a vacuum. An illustration of the vacuum pump is shown in Figure 3.6.

Figure 3.6: Faucet aspirator vacuum pump illustration.

To ensure the homogeneity of the mixtures, samples were mixed thoroughly prior to testing using a laboratory mixer (RW 20 digital overhead stirrer, IKA-Werke GmbH & Co., Staufen, Germany). The mixer operates from 60 to 2000 RPM and was used with a 45° pitched blade turbine impeller.

3.2.2. Sample Preparation Procedure

Prior to testing sample viscosity and aggregate properties, the carrier fluid must first be isolated from the raw slurry sample. Coarse solid material and larger bitumen droplets were removed by sieving the slurry. Residual bitumen was removed using RHS beads. A portion of the suspending liquid (process water) was isolated by filtration for use in analytical testing, rheology measurements and sample dilution.

A step-by-step procedure detailing the sample preparation has been provided:

1. Collect 100 mL of well-mixed raw sample for Dean-Stark analysis.
2. Pour the remaining raw slurry mixture (at least 1000 mL) onto a 75 micron (200 mesh) sieve with collector pan placed beneath to retain fluid and fine particles.
3. Shake sieve vigorously by hand for at least five minutes to ensure all liquid and fine particles pass through. Approximately 900 mL of sample should be accumulated.
4. Sample 100 mL of sieved slurry for QuickBit testing or Dean-Stark analysis.

5. Add 400 mL of sieved sample to glass jar with metal baffle placed inside.
6. Add RHS beads to jar such that beads are added at a ratio of approximately 6:1 beads-to-bitumen by mass.
7. Using hot water bath at approximately 45°C, heat jar containing beads and tailings samples to for 10 minutes.
8. Place jar on rotating mixer and mix for 10 minutes. Remove and allow jar to stand until RHS beads rise to the top of the container.
9. Pour mixture through metal strainer and collect in a beaker. Retain beads for regeneration. Return sample to glass jar.
10. Repeat bead treatment (steps 6 through 8) five additional times to ensure maximum bitumen removal.
11. Repeat steps 5 through 10 to accumulate 800 mL of bead treated sample.
12. Sample 100 mL for Dean-Stark analysis of carrier fluid sample.
13. Filter portion of bead-treated sample to accumulate at least 350 mL of filtrate water. Repeat filtration at least three times to ensure total solids removal.
14. Sample 100 mL of filtrate water for ion chromatography.

3.3. Analytical Testing

3.3.1. Dean Stark Analysis

Modified Dean Stark extraction (Wallace, 1988) or other similar methods (Bulmer & Starr, 1979) are used industrially to determine the overall composition of slurry samples. This type of analysis measures the amount of mineral solids, water, and hydrocarbon in each sample. An example of Dean Stark extraction equipment is shown in Figure 3.7 (taken from Carlson, 2006, pp. 435).

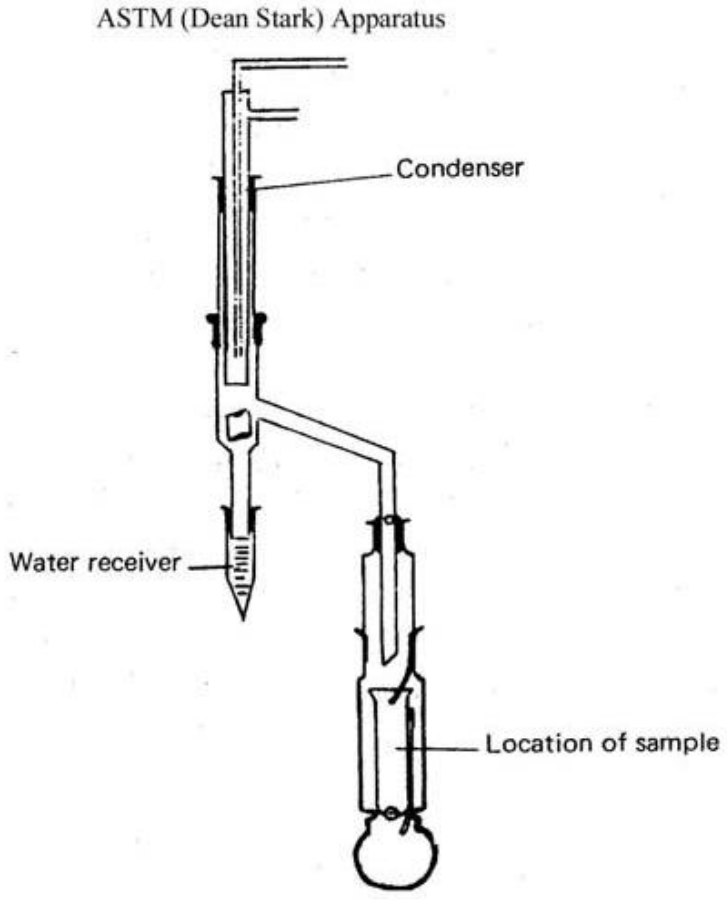

Figure 3.7: Dean Stark analysis apparatus (from Carlson, 2006).

In a Modified Dean Stark extraction, the slurry sample is placed inside a cellulose thimble inside a flask within the apparatus. Toluene is added to the flask and the mixture is refluxed in a closed system. Toluene, dissolved bitumen and water evaporate within the device, and are cooled and collected in a side-arm or trap (Wallace, 1988). Since the toluene and bitumen are water-insoluble, the liquids form two distinct phases allowing the water to be separated and measured. Solids remain behind on the thimble. The weight of the solids is measured after the reflux is complete and the thimble has been dried. Bitumen content can be determined by completing a mass balance for the initial sample or alternatively, filter paper may be wet with the hydrocarbon mixture and allowed to dry under a fume hood leaving behind only bitumen on the filter medium.

Dean Stark analysis was completed for all raw slurry samples, and all carrier fluid samples tested. Testing was completed by AGAT Laboratories and the Shell Research Centre, both located in Calgary, AB. A minimum of 75 mL of slurry sample was provided for testing. In earlier phases of experiments, Dean Stark extractions were also completed for some sieved samples. Raw data from Dean Stark testing can be found in Appendix 1: Dean Stark Analysis Results.

3.3.2. QuickBit Testing

QuickBit testing is an adapted version of Dean Stark analysis. The test was used to give rough estimates of bitumen and solids content to determine the amount of RHS beads required for bitumen removal and necessary sample dilution for

particle size analysis. A tabletop centrifuge (Centrifuge Model No. 1505, Hamilton Bell Co. Inc., Montvale, NJ, USA) was used to promote the separation of the QuickBit samples into two phases. The centrifuge operates at a speed of 3400 RPM. All tests were completed at room temperature. Detailed results of QuickBit testing are shown in Appendix 2: QuickBit Testing Results.

The procedure used for QuickBit testing is as follows:

1. Create test sample by adding 5 mL each of slurry and toluene to 15 mL test tube. Cap the test tube.
2. Shake vigorously for approximately 5 minutes, or until no bitumen appears to remain on solids.
3. Place test tube in centrifuge ensuring the device is balanced to prevent damage. Centrifuge for 5 minutes or until two distinct layers are apparent in test tube. Normally 5 minutes is sufficient.
4. Pipette 2 mL of upper "oil" phase, and dispense onto a pre-weighed piece of Whatman 1 Qualitative filter paper. Allow filter paper to dry completely and re-weigh. The total bitumen mass = 2.5 × mass of dried bitumen on the filter paper.
5. Remove as much of remaining oil phase as possible from the test tube and dispose.
6. Pour entire lower "aqueous" phase with solids onto pre-weighed piece of Whatman 5 Qualitative filter paper. Allow filter paper and solids to dry completely and re-weigh to determine solids content of sample.

3.3.3. Water Ion Chromatography

Ion chromatography testing was performed by University of Alberta Natural Analytical laboratory in Edmonton, AB. The tests measured concentrations of key ions in filtrate water samples including: iron (Fe^{3+}), aluminum (Al^{3+}), calcium (Ca^{2+}), potassium (K^{+}), sodium (Na^{+}), magnesium (Mg^{2+}), chloride (Cl^{-}), sulphate (SO_4^{2-}), nitrate (NO_3^{-}), bicarbonate (HCO_3^{-}), and carbonate (CO_3^{2-}). The sample pH and conductivity were also measured. As stated previously, changes in sample water chemistry greatly affect the formation and strength of clay aggregates. As a result the presence of the ions was monitored to account for changes in fine particle behaviour. One measure of overall water chemistry is ionic strength, which is a measure of the total concentration of electrolytes (Schramm, 1996). The ionic strength of the sample water was calculated using:

$$I = \frac{1}{2} \Sigma \, c_i Z_i^{\,2} \qquad \textbf{(3.1)}$$

where c_i is the molar concentration of each ion species i, and Z_i is the charge number of each ion.

A minimum of 100 mL of filtrate water was required for testing. A complete listing of the results of the ion chromatography testing and calculation of ion strength can be found in Appendix 3: Water Ion Chromatography Results.

3.4. Rheology

3.4.1. Apparatus

All rheology measurements were made using a controlled stress / direct strain / controlled rate rheometer (AR-G2, TA Instruments, New Castle, DE, USA). The measuring systems available for the AR-G2 include: concentric cylinder, parallel plate, and cone and plate. The device has minimum and maximum rotational speeds of 1.4E-9 and 300 rad/s, respectively. In steady, controlled rate operation torque response can be measured in the range of 0.01 μNm to 200 mNm with a resolution of 0.1 nNm. The device is temperature controlled by a re-circulating fluid bath utilizing de-ionized water as the heating/cooling medium. Figure 3.8 shows the AR-G2 rheometer.

Figure 3.8: AR-G2 rheometer (from TA Instruments, 2006).

The concentric cylinder measurement system was selected for testing as it was the most suitable geometry for the relatively low viscosities of the samples examined. Concentric cylinder rheometers operate on the principle of Couette flow, which was discussed in the previous chapter. Rotor speed is controlled and torque response is measured by the device. The rotor used in testing was the conical aluminum DIN rotor. Specifications of the measurement system are given in Table 3.2.

Table 3.2: Specifications of AR-G2 concentric cylinder geometry.

Geometry	Concentric Cylinder with DIN Rotor
Cup Diameter (mm)	30.40
Rotor Diameter (mm)	28.00
Rotor Length (mm)	42.03
Minimum Sample (mL)	22.42
Operating Gap (mm)	0.010

The conical design of the rotor helps to minimize end effects of the rheometer cup. Figure 3.9 shows an image of the AR-G2 concentric cylinder geometry. An illustration of the concentric cylinder geometry is provided in Figure 2.3.

Figure 3.9: AR-G2 concentric cylinder geometry (from TA Instruments, 2006).

The rheometer was calibrated using Newtonian oil standards (Cannon Instrument Company, State College, PA, USA) having different viscosities. The standards selected were in the low (S6), medium (N100), and high (N1000) range of torque for the device. The properties of the standards are given in Table 3.3.

Table 3.3: Properties of Newtonian oil standards at 25°C.

Standard Oil	Density (kg/m^3)	Viscosity (mPas)
N100	869.0	202.2
N1000	846.3	2018.0
S6	874.0	7.852

Each standard was tested at 25°C with the concentric cylinder geometry. Experimental results were compared to viscosity data provided by the manufacturer. An example of this calibration data is shown in Figure 3.10. The results for calibration tests are shown in Table 3.4. Complete calibration data for the rheometer can be found in Appendix 4: AR-G2 Rheometer Calibration Data.

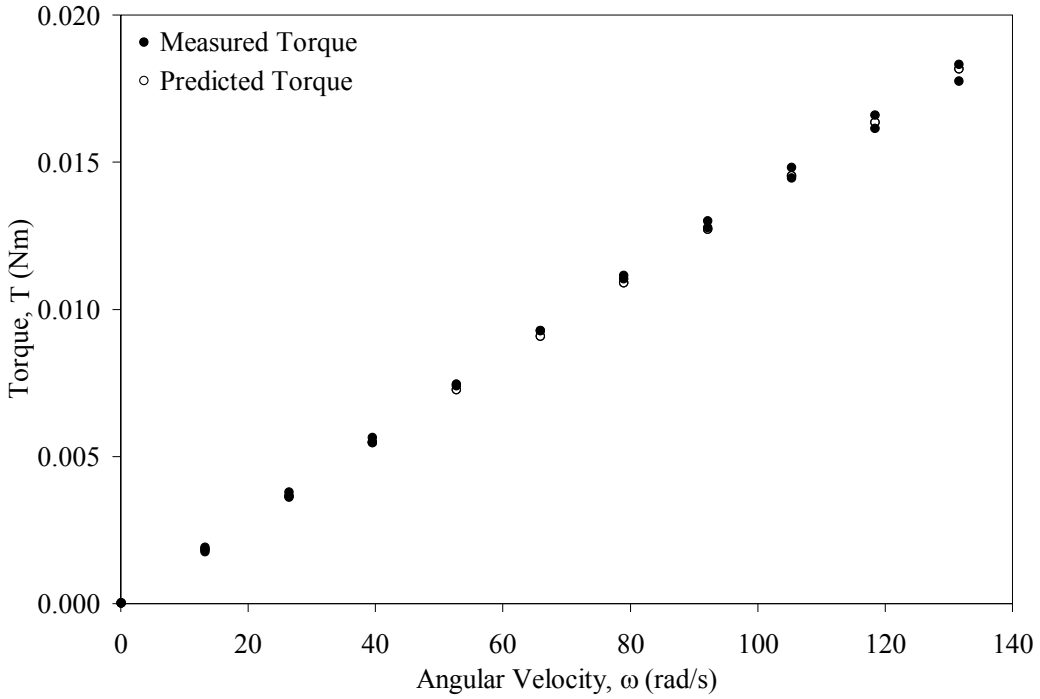

Figure 3.10: Calibration curve of Newtonian oil standard N100 at 25°C.

Table 3.4: Measured viscosity of Newtonian oil standards at 25°C.

Standard Oil	Measured Viscosity (mPas)	% Error
N100	203.3	0.5
N1000	1938.9	3.9
S6	8.68	10.6

It can be seen from the calibration runs that the measured viscosity for the standard at the lowest range of torque values (S6) has an error of approximately +10%. The viscosities for process water samples, discussed in greater detail in Chapter 4, also had +10% error when compared to the viscosity of de-ionized water at 25°C. As a result it is expected that the magnitude of measurement error should be the same for all of the low viscosity filtrate water and carrier fluid samples. Because the correlating parameter is ratio of viscosity values, μ_r, this level of error will not impact the final results.

3.4.2. Rheometer Test Procedure

Carrier fluid and filtrate water samples were tested using the AR-G2 rheometer to determine sample viscosity and yield stress (where applicable). Detailed results given in Appendix 5: Rheological Measurements of Carrier Fluid Water and Appendix 6: Rheological Measurements of Carrier Fluid Slurries.

The procedure for rheometer testing is as follows:

1. Open valve to rheometer air supply and adjust pressure to 32 psi.
2. Remove bearing lock from rheometer and ensure the spindle bearing moves freely.
3. Turn on computer, rheometer and temperature control system. Open instrument software and ensure computer and instrument communication is initiated.
4. Perform instrument calibration on device free of geometry. Expand the Calibration menu to view the inertial calibration tab – click ‘Calibrate’ and select ‘Accept’ when calibration is complete.
5. Attach conical DIN rotor to bearing. Expand the Geometry menu and select concentric cylinder geometry software.
6. Perform instrument mapping. Expand the Calibration menu to view the rotational mapping tab – select ‘Standard’ mapping with two iterations - press ‘Calibrate’ to begin mapping. The mapping will be complete after approximately 2 minutes.

7. Adjust temperature set-point to 25°C and wait for equilibration. This will take about one minute. The temperature reading under the Instrument display panel will remain near constant when the device has equilibrated.
8. Perform zero gap measurement. Expand the Instrument menu and click 'Zero Gap'. Adjust rotor using ↑/↓ buttons to within 10 mm of the bottom of the cup (use guide line on rotor stem and top of cup as reference points). Click 'Start' to begin.
9. Expand Experiment menu and set testing gap to 10 μm and click 'Ok'. Then under the Instrument menu click 'Raise To Loading Gap'.
10. If testing carrier fluid sample, mix with overhead mixer for 60 minutes at 400 RPM prior to use.
11. Expand the Experiment menu and create test procedure appropriate for sample (see Table 3.5 for details).
12. Add 23 mL of sample to the rheometer cup and click 'Go To Geometry Gap'. When rotor has stopped moving begin testing by clicking green 'Play' button under Home menu.
13. At the end of each test, raise the rotor, remove the rotor and cup and clean thoroughly.
14. When testing is complete turn off computer, rheometer and temperature control system.
15. Replace bearing lock and turn off rheometer air supply.

Table 3.5: Rheometer test specifications.

Sample	Filtrate Water	Slurry
Step Name	1. Flow – Peak Hold	1. Flow – Peak Hold
Temperature	25°C	25°C
Controlled Variable	Velocity (20 rad/s)	Velocity (25 rad/s)
Time	300 s	60 s
Step Name	2. Flow – Linear Sweep	2. Flow – Linear Sweep
Temperature	25°C	25°C
Controlled Variable	Velocity (0.1 to 15 rad/s)	Velocity (20 to 0.1 rad/s)
Number of Points	20	20
Point Termination	Yes, at steady state (5 consecutive w/in 5%)	Yes, at steady state (5 consecutive w/in 5%)
Sample Period	3 s	3 s
Max. Point Time	60 s	60 s
Step Name	3. Flow – Linear Sweep	3. Flow – Linear Sweep
Temperature	25°C	25°C
Controlled Variable	Velocity (15 to 0.1 rad/s)	Velocity (0.1 to 20 rad/s)
Number of Points	20	20
Point Termination	Yes, at steady state (5 consecutive w/in 5%)	Yes, at steady state (5 consecutive w/in 5%)
Sample Period	3 s	3 s
Max. Point Time	60 s	60 s

3.5. Particle Size and Shape Analysis

3.5.1. Apparatus

Slurry particle size and morphology were examined using a Sysmex Flow Particle Image Analyzer (Sysmex FPIA 3000, Malvern, Worcestershire, UK). Particles are measured in suspension, allowing both primary particles and aggregate structures to be seen in their natural states. Tests can be completed with as little as 1 mL of solution; however, the manufacturer recommends 5 mL of sample is injected for each test. Test solutions must be sufficiently dilute (< 360,000 particles per sample) to obtain clear images. Figure 3.11 shows an illustration of the FPIA.

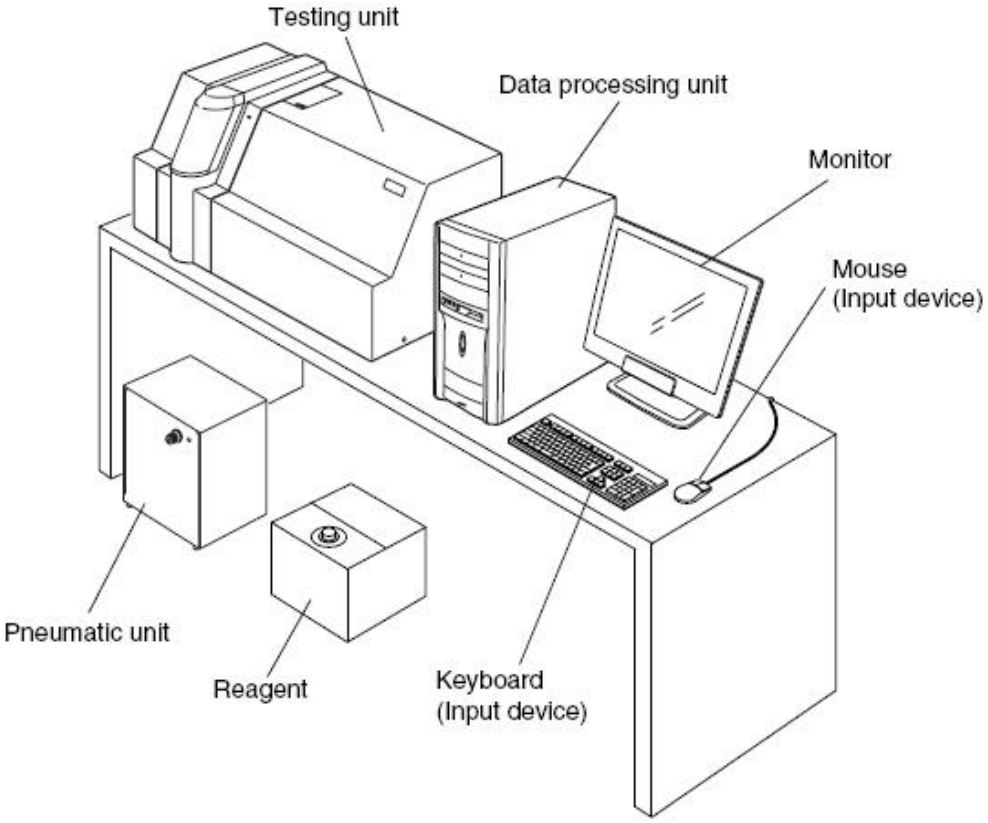

Figure 3.11: Sysmex FPIA-3000 (from Sysmex Corporation, 2008).

The FPIA can measure particles in the range of 0.8 to 300 μm for suspensions and emulsions. The entire range of particle sizes is measured using a variety of lenses under high (HPF) and low (LPF) power magnification fields. The FPIA uses 0.035 μL of sample for tests conducted with the high power field tests and 0.55 μL for low power field tests. The particle range of each lens is shown in Table 3.6. Particle circularity, the ratio of particle circumference to the circumference of a circle with the same area, can be measured in the range of 0.200 to 1.000.

Table 3.6: FPIA-3000 measuring unit specifications.

Measuring Unit	**Particle Size Range (HPF)**	**Particle Size Range (LPF)**
Standard (10×)	1.5 – 40 μm	8.0 – 160 μm
High Magnification (20×)	0.8 – 20 μm	4.0 – 80 μm
Low Magnification (5×)	3.0 – 80 μm	16.0 – 300 μm

The FPIA device operates on the principles of flow cytometry, also called automated image analysis, where a thin sheath of fluid is analysed to determine particle size and shape. The stream of sample is made extremely narrow ensuring the largest particle face is oriented toward the camera. During testing, images are taken of each particle or aggregate at a rate of 60 frames per second. The images

are stored and the projected area of each entity is determined. An illustration of the FPIA sheath fluid flow can be seen in Figure 3.12. Most chemical solvents may be used as sheath fluid. Standard aqueous electrolyte sheath fluid was used in testing for this project. Additional information about the standard sheath fluid is given in Appendix 7: FPIA Settings and Sample Dispersion Information.

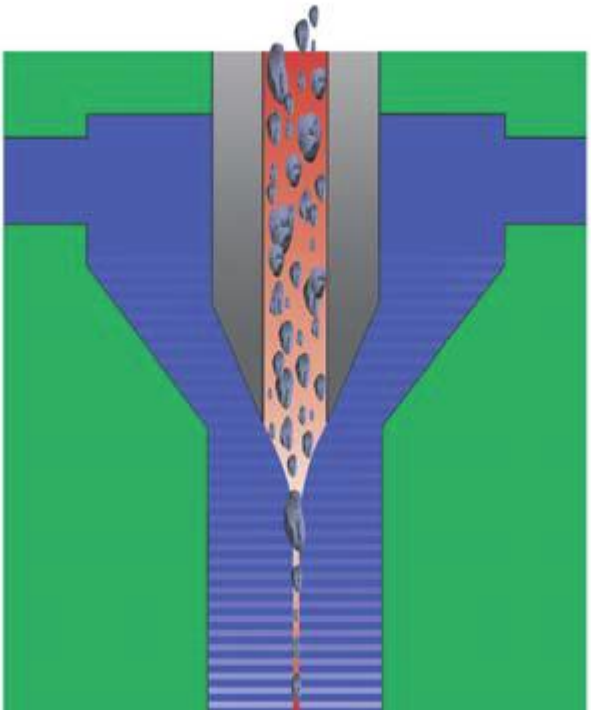

Figure 3.12: FPIA sheath flow (from Sysmex Corporation, 2008).

FPIA results were used to determine the concentration of aggregates in the slurry samples. Samples were tested in their aggregated state, then dispersed and retested. All samples were diluted with filtrate water to concentrations of roughly 10 grams of solids per litre. Tests were completed using the standard lens under the high power field in order to capture the highest number of particles in the

range of interest. Particle entities were analyzed to determine projected area and overall mean circularity. After samples were tested in their aggregated form, the slurries were dispersed by adding sodium hydroxide to increase pH by, adding a chemical dispersant tetrasodium pyrophosphate (TSPP), and using a sonicating probe (Misonix Sonicator – 4000, Qsonica, LLC, Newtown, CT, USA). Aggregated and dispersed mixtures were each sampled three times to ensure accuracy of results. FPIA results were found to be highly repeatable, and the effects of both system and human error were negligible (Shahmirzadi, 2012).

Each time the device is turned on a start-up procedure is run to check the test field for residue from previous runs and to focus the instrument. The FPIA is focussed by injecting an extremely dilute solution of mono-sized polystyrene spheres. A good auto-focus run will have a very narrow size distribution with its peak frequency (mode) occurring at the sphere diameter specified by the calibration solution manufacturer. An example of a good auto-focus test is shown in Figure 3.13. The frequency (%) provided by the FPIA is normalized using diameter data bin size (μm).

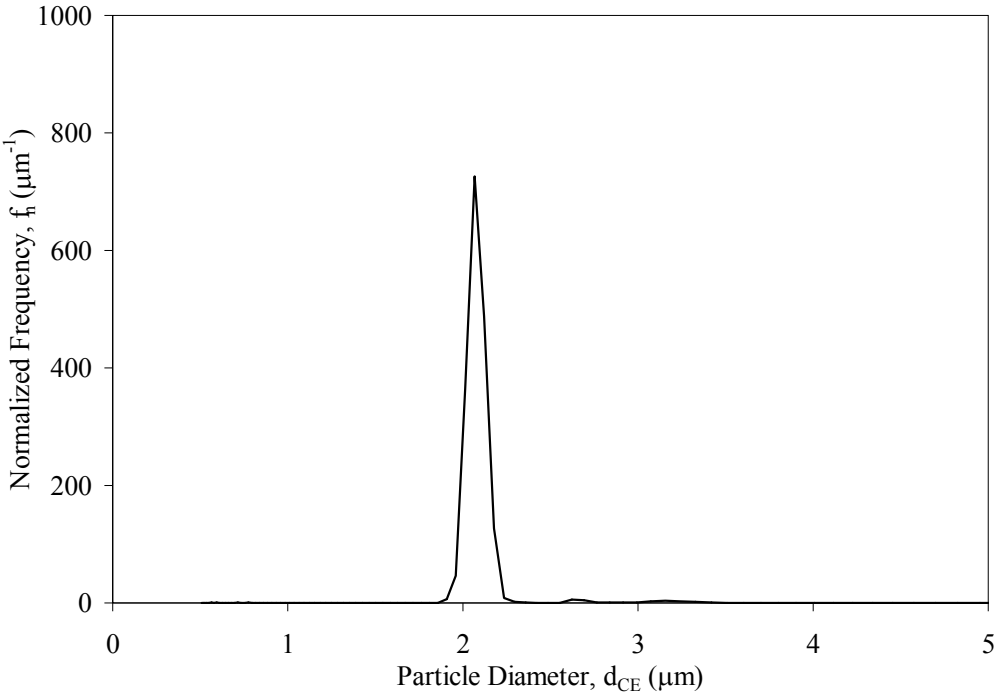

Figure 3.13: FPIA auto-focus test for 2.0 μm spherical polystyrene beads in dilute solution.

3.5.2. Aggregate Size and Concentration in the FPIA

Two-dimensional image analysis captures flat or projected pictures of particle entities. An area equivalent diameter, d_{CE}, is the diameter of a circle of equivalent projected area A_p to the particle entity. Determination of d_{CE} for each image is made using the following equation:

$$d_{CE} = \left(\frac{4A_p}{\pi} \right)^{1/2} \qquad \textbf{(3.2)}$$

The d_{50} is the diameter at which 50% of the total solids volume is composed of larger particles. This median diameter is the value most commonly referred to in industry and is the diameter used in slurry flow correlations (Shook et al., 2002). This characteristic diameter is particularly useful in industrial settings where the individual particles can not be counted. Other measures of mean diameter can be determined from automated image analysis, where every particle is counted and captured for later analysis. The volume-based mean diameter d[3,0] is given by:

$$d[3,0] = \left(\frac{\Sigma d_{CE}^{\ 3}}{N} \right)^{1/3} \qquad \textbf{(3.3)}$$

where N is the total number of particles. Volume-based mean particle size may overestimate particle or aggregate concentration for irregular plate-like clays. It may be more useful to refer to the number based mean, which does not make assumptions as to particle shape. The number based mean diameter d[1,0] is determined using:

$$d[1,0] = \frac{\Sigma d_{CE}}{N} \qquad \textbf{(3.4)}$$

Determination of aggregate concentration can also be found using d_{CE}. For spherical or near spherical particle entities, aggregate concentration C_{agg} may be determined directly using:

$$C_{agg} = \frac{\frac{\pi}{6} \Sigma d_{CE}^{3}}{\overline{V}_{sample}} \quad \textbf{(3.5)}$$

$\overline{V}_{sample}$ is the volume of sample tested. For non-spherical aggregates, diameter may not be sufficient to determine the true volume of the entity. Information about particle shape must also be measured to find true particle volume.

3.5.3. Aggregate Shape in the FPIA

Shook et al. (2002) suggests that for non-spherical particles, deviations from the Einstein equation and higher relative viscosity should be expected. Additional parameters must be defined in order to characterize the non-spherical nature of slurries. Shape parameters can be used to determine many properties inherent to aggregates such as individual aggregate volume, or settling velocity. Shook & Roco (1991) noted that for non-spherical particles, terminal settling velocity of a particle is a function not just of size, but also shape and orientation. Many devices using flow image analysis have the ability to measure shape parameters of aggregate structures.

One example of a shape parameter, sphericity, can be measured using three-dimensional imaging techniques such as SEM, and cryo-SEM. This property gives a measure of how spherical aggregates may be, or in other words, a comparison of the surface area of an entity with respect to the surface area of a sphere of equal volume. For two-dimensional testing methods like flow particle

image analysis, a similar property called circularity can be measured. Circularity is a comparison of the circumference of an area-equivalent circle to the true perimeter of the particle. An equation to calculate particle circularity is given by:

$$\text{Circularity} = \frac{2\left(\pi A_p\right)^{1/2}}{P_p} \qquad \textbf{(3.6)}$$

where P_p is the particle perimeter.

3.5.4. Flow Particle Image Analyzer (FPIA) Test Procedure

Carrier fluid samples were tested using the Sysmex FPIA-3000 to measure size and shape distributions of samples in their aggregated and dispersed states. Detailed results are given in Appendix 8: Particle Size Distributions of Carrier Fluid Samples and Appendix 9: Shape Distributions of Carrier Fluid Samples.

The procedure used for testing is as follows:

1. Create dilute sample for testing by mixing 100 mL sample at a concentration of approximately 10 g solids/L. Combine required amounts of slurry sample and filtrate water in 250 mL jacketed beaker and mix sample for 60 minutes at 400 RPM.
2. Turn on FPIA and open software allowing start-up sequence to run. Do not begin testing until the internal temperature and pressure of the device have stabilized.

3. Perform background check to ensure field is free of particles. If more than five particles are detected, repeat background check.
4. Perform auto focus to calibrate lens using 5 mL of the appropriate diluted polystyrene solution.
5. Begin test using Standard HPF Test Procedure (see Table 3.10 below for details) and inject 5 mL of well mixed sample into the FPIA. Repeat two additional tests.
6. Turn on water bath for jacketed beaker and adjust temperature to 5°C. Allow sample temperature to stabilize.
7. Add aqueous NaOH to diluted sample until the measured pH is approximately 10. Add about 0.05 g of dispersant TSPP to beaker and begin sonication.
8. While sonicating, begin test using custom FPIA test procedure (see Table 3.9 below for details) and inject 5 mL of well mixed dispersed sample into the FPIA. Repeat two additional tests.
9. When testing is completed, close FPIA software and begin shut-down sequence. When prompted, inject 10 mL of de-ionized water into the testing chamber. Turn off FPIA unit.
10. Empty waste bottle into appropriate storage container.

Table 3.7: FPIA test specifications.

Operating Procedure	HPF Standard	Custom
Test Field	HPF	HPF
Count Method	Stop by Time	Stop by Time
Field Lens	×10	×10
Light Field System	Bright field	Bright field
Repeat Times	1	1
Ultrasonic Power	5%	5-50%*
Mid-test Irradiation	Not Apply	Not Apply
Pre-test Irradiation Time	0s	10 – 20s*
Mixing Mode	Apply	Not Apply
RPM Target	300 RPM	-
RPM Range	100 RPM	-

*See Appendix 7: FPIA Settings and Sample Dispersion Information for details.

4. Results and Discussion

4.1. Analytical Testing

4.1.1. Dean Stark Analysis

Dean Stark analysis was used to measure the solid, bitumen and water content of slurry samples. The composition of each raw sample is provided in Table 4.1.

Table 4.1: Composition of raw slurry samples.

Sample ID	Vol% Solids	Vol% Bitumen	Vol% Water
S-M Raw	18.48	0.02	81.50
S-MFT Raw	14.53	5.08	80.39
S-TSRU Raw	7.57	6.65	85.78
S-TT Raw	9.27	0.07	90.66
SU-M Raw	28.03	0.01	71.96
SU-NW Raw	4.72	0.01	95.27
SU-RDW Raw	2.08	0.02	97.91
SU-T Raw	24.86	0.02	75.12
SU-TF Raw	29.59	0.01	70.40
SU-TPSC Raw	34.06	0.01	65.93
SU-TSF Raw	23.38	0.01	76.61
SY-HT Raw	36.17	9.86	53.97
SY-M Raw	21.87	7.57	70.56
SY-T Raw	23.75	6.95	69.30
T-T Raw	6.7	0.4	92.9

Following the sample preparation discussed in Chapter 3, Dean Stark analysis was performed on the carrier fluid samples. Carrier fluid sample compositions are given in Table 4.2.

Table 4.2: Composition of carrier fluid slurry samples.

Sample ID	Vol% Solids	Vol% Bitumen	Vol% Water
S-M1	6.01	0.00	93.99
S-MFT1	14.61	0.01	85.38
S-TSRU1	3.00	1.68	95.32
S-TT1	9.13	0.41	90.46
SU-M1	7.58	0.00	92.42
SU-NW1	4.43	0.01	95.56
SU-RDW1	2.07	0.01	97.92
SU-T1	4.88	0.01	95.11
SU-TF1	5.74	0.00	94.26
SU-TPSC1	5.44	0.00	94.56
SU-TSF1	7.13	0.00	92.57
SY-HT1	18.37	0.01	81.62
SY-M1	9.30	0.01	90.69
SY-T1	10.59	0.01	89.40
T-T1	1.84	0.42	97.74

For a number of slurry samples testing was repeated using additional raw slurry in order to determine the reproducibility of rheology and FPIA results. Slurry samples S-M2, S-MFT2, S-TSRU3, S-TT3 and T-T3 are the replicates tested. These replicate samples were prepared and tested according to procedures detailed in Chapter 3, however the samples did not undergo analytical testing. It was assumed that compositions and process water properties were identical to those measured for original samples (S-M1, S-MFT1, S-TSRU1, S-TT1 and T-T1 respectively). This assumption was verified for sample S-M2, which was compared to sample S-M1. Less than 0.5% change in composition was seen between the samples.

In order to test the effects of concentration on carrier fluid viscosity, a number of samples were diluted or concentrated. Slurry sample S-TT1 was diluted with filtrate water in order to create sample S-TT2. Slurry samples S-TSRU1, SU-TF1, SU-TPSC1, and T-T1 were allowed to settle and liquid was decanted to create more concentrated slurries (S-TSRU2, SU-TF2, SU-TPSC2, and T-T2 respectively). The compositions of the carrier fluid samples with laboratory-altered solids concentrations are given in Table 4.3.

Table 4.3: Composition of laboratory-altered carrier fluid samples.

Sample ID	Vol% Solids	Vol% Bitumen	Vol% Water
S-MFT2	14.61	0.01	85.38
S-TSRU2	4.76	2.95	92.29
S-TT2	8.11	0.24	91.65
SU-TF2	7.13	0.00	92.87
T-T2	4.47	0.78	94.75

Raw data from all Dean Stark testing can be found in Appendix 1: Dean Stark Analysis Results.

4.1.2. Water Ion Chromatography

Ion chromatography testing was performed to determine the water chemistry of carrier fluid samples. Table 4.4 gives the pH, conductivity, ionic strength and key ion content for all samples. Complete testing results are shown in Appendix 3: Water Ion Chromatography Results.

Table 4.4: Conductivity, pH, ionic strength and major ions of filtrate water.

Sample ID	pH	Conductivity (MS/cm)	Ionic Strength (mol/L)	Ca^{2+} (mg/L)	Cl^{-} (mg/L)
S-M	8.53	1.51	0.017	21.0	168
S-MFT	8.81	1.54	0.020	19.0	273
S-TSRU	9.14	1.17	0.015	9.5	160
S-TT	8.99	1.57	0.025	8.4	723
SU-M	9.08	3.02	0.042	7.3	769
SU-NW	8.73	3.09	0.041	5.7	193
SU-RDW	8.76	3.12	0.040	6.3	775
SU-T	9.30	3.37	0.045	6.5	807
SU-TF	9.02	3.01	0.038	6.0	723
SU-TPSC	9.05	3.00	0.038	7.5	708
SU-TSF	9.09	2.76	0.039	7.6	731
SY-HT	8.63	3.35	0.044	73.1	496
SY-M	8.90	3.39	0.108	42.7	412
SY-T	8.58	3.14	0.102	35.5	401
T-T	8.58	0.64	0.016	12.6	54.0

4.1.3. Effect of RHS Beads

Tests were completed to verify that slurry interaction with the RHS beads during bitumen removal did not cause unwanted side effects, such as changes to the process water chemistry. A comparison was made for a low-bitumen (~0.5 vol. %) tailings sample, one portion RHS bead treated (T-T1) and one not (T-T(B)1), to examine effects of the RHS beads on rheology and particle imaging. Results are shown in Table 4.5.

Table 4.5: Effects of RHS bead treatment on slurry carrier fluid.

Sample	T-T1	T-T(B)1
Bitumen Content (Vol. %)	0.4	0.6
Relative Viscosity	1.34	1.30
d[1,0] (μm)	2.41	2.23
d[3,0] (μm)	10.56	9.92
Circularity (Aggregated)	0.871	0.868
Circularity (Dispersed)	0.924	0.924

The RHS beads had a negligible effect on the slurry sample. Rheological behaviour and particle size and shape show no measurable change due to bead treatment. Water ion chromatography also demonstrated no appreciable change. Detailed test results for both samples can be seen in the Appendices.

4.2. Rheology

4.2.1. Rheology Measurements

Rheological behaviour of slurry sample carrier fluid and filtrate water was measured at 25ºC using the AR-G2 rheometer. Measurements were used to determine the carrier fluid relative viscosity, defined as the ratio of carrier fluid viscosity to filtrate water viscosity, for each sample. Torque response was measured as a function of the controlled spindle speed or angular velocity. Measured torque values are normalized using the system factor α (Equation 2.7), which has a value of 6.83×10^{-4} m^3 for the geometry used in this study. The normalized values were then plotted as a function of angular velocity.

Valid data points were fitted using the rheological models previously discussed in Chapter 2 (Equations 2.8 and 2.12). Data points measured after the onset of Taylor vortices (Equation 2.9) were omitted. For samples exhibiting Bingham plastic behaviour, data points measured in the region of incomplete shearing (Equation 2.13) were also eliminated. The sample viscosity and yield stress are calculated using the slope and intercept of a line of best fit for each data set. An example of a Newtonian filtrate water rheology plot is shown in Figure 4.1. A Bingham fluid rheology plot is shown in Figure 4.2. Complete data for all tests is given in Appendix 5: Rheological Measurements of Carrier Fluid Water and Appendix 6: Rheological Measurements of Carrier Fluid Slurries.

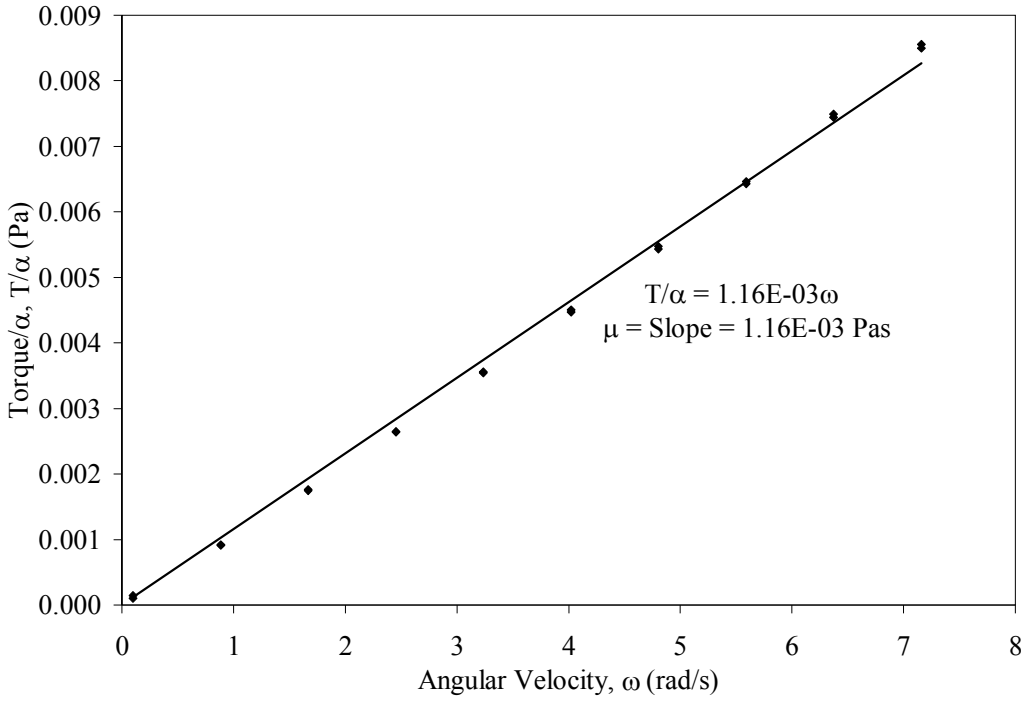

Figure 4.1: Rheology of Syncrude hydrotransport (SY-T) filtrate water.

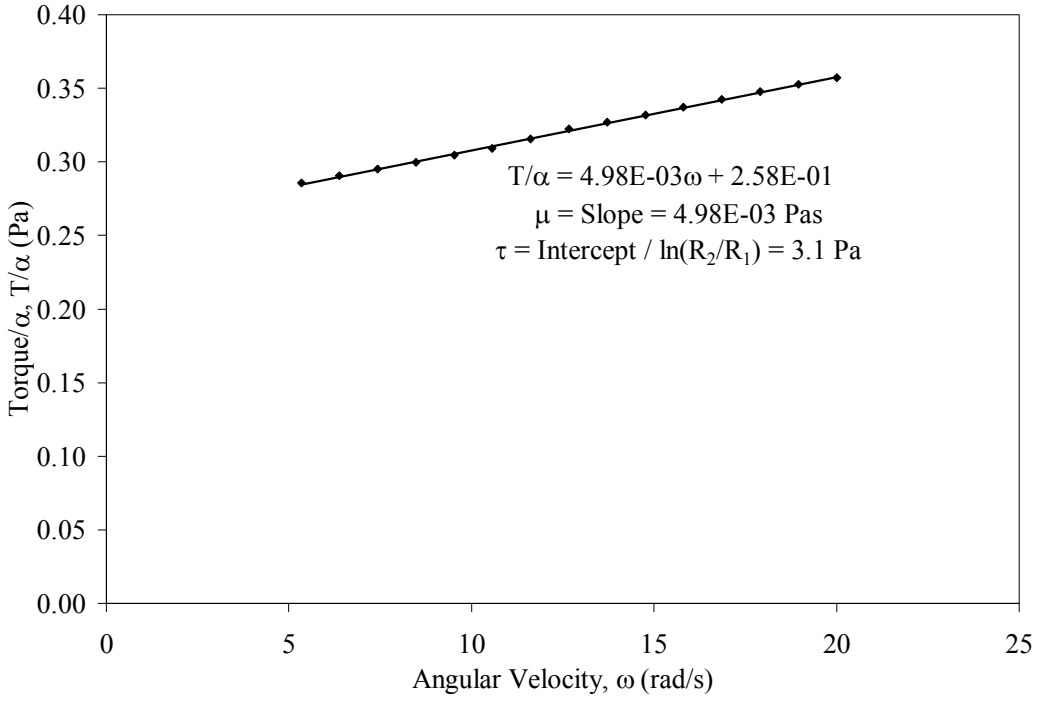

Figure 4.2: Rheology of Syncrude hydrotransport (SY-T1) carrier fluid.

The standard error of the model fit for each sample was determined using Equation 4.1, taken from the AR-G2 rheometer software manual (TA Instruments, 2004):

$$\text{Standard Error} = \frac{\left[\frac{\sum\left(T_{meas.} - T_{calc.}\right)^2}{N-2}\right]^{\frac{1}{2}}}{\text{Range}} \times 1000 \qquad \textbf{(4.1)}$$

$T_{meas.}$ denotes the measured torque value, and $T_{calc.}$ is the torque value at the same spindle speed calculated from Equations 2.6 (Newtonian) or 2.11 (Bingham plastic). N is the total number of points used in determining the model. 'Range' is the difference between the maximum and minimum measured torque values. Lower values of standard error indicate a better fit for data, with values above 20 indicating a poor fit (TA Instruments, 2004).

Data for all filtrate water samples were fitted using the Newtonian model given by Equation 2.8. Carrier fluid samples exhibiting near zero torque values at low shear rates were assumed to have no yield stress and were also fitted using the Newtonian model. Slurry samples that appeared to exhibit yield stress were fitted using the Bingham fluid model given in Equation 2.12. The relative viscosity for each carrier fluid sample was calculated using Equation 2.1. The relative viscosity of samples with respect to fines concentration determined by Dean Stark analysis is shown in Figure 4.3. Viscosity and standard error results for filtrate water samples are shown in Table 4.6. Table 4.7 shows viscosity and standard error

results for carrier fluid slurry samples. Wherever multiple tests were completed, the data point presented represents the mean value for each sample.

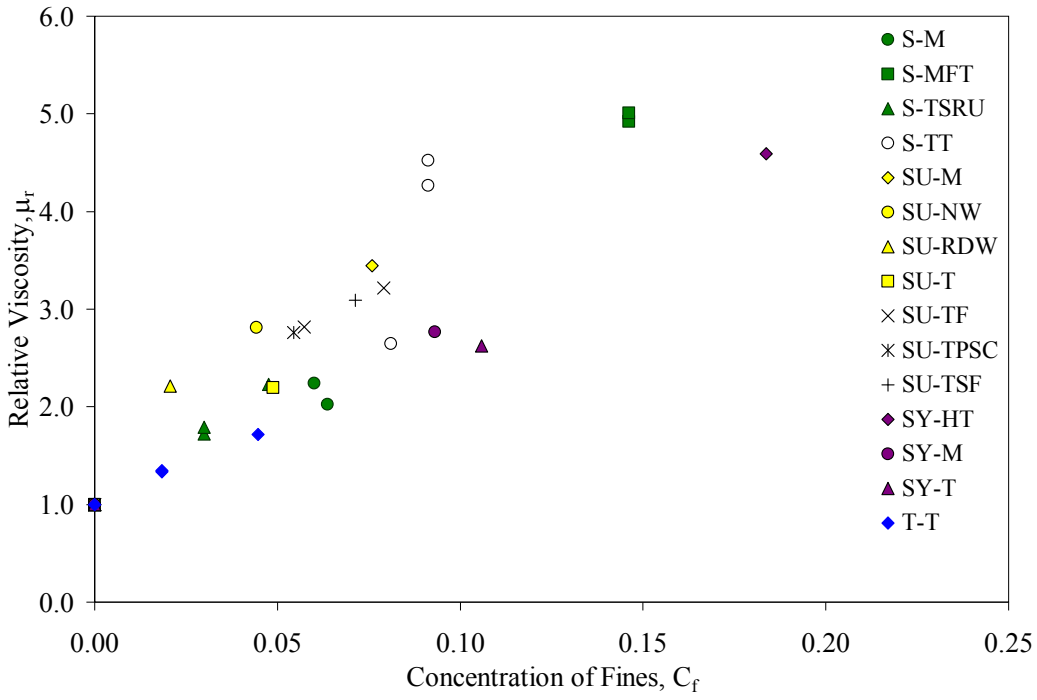

Figure 4.3: Carrier fluid relative viscosity with respect to overall fines concentration for industrial slurry samples.

It can be seen that there is some scattering of the data, and no single trend is apparent.

The values of standard error seen for the filtrate water samples are typically high. This may be due to the increased error at low torque values which was seen for tests done with Newtonian oil calibration standards. The standard error values are still in the range considered to be good model fit; however, viscosity values are

approximately 10% greater than those expected for water. This degree of error was also seen for calibration measurements of the low viscosity standard (S6). It is expected that this level of error will be seen for all low viscosity samples, and as a result this will not affect relative viscosity values.

Table 4.6: Carrier fluid filtrate water rheology results.

Sample ID	Viscosity (mPas)	Standard Error
S-M Water	1.12	18.5
S-MFT Water	1.17	18.3
S-TSRU Water	1.14	17.0
S-TT Water	1.13	17.5
SU-M Water	1.13	18.9
SU-NW Water	1.13	18.8
SU-RDW Water	1.16	17.9
SU-T Water	1.20	17.9
SU-TF Water	1.14	19.3
SU-TPSC Water	1.14	18.0
SU-TSF Water	1.16	17.7
SY-HT Water	1.17	19.5
SY-M Water	1.15	17.9
SY-T Water	1.14	18.2
T-T Water	1.15	17.2

Table 4.7: Carrier fluid slurry rheology results.

Sample ID	Viscosity (mPas)	Yield Stress (Pa)	Standard Error
S-M1	2.50	0.1	5.6
S-MFT1	5.78	1.0	10.4
S-TSRU1	1.96	0.0	15.7
S-TSRU2	2.54	0.0	10.0
S-TT1	4.82	1.1	3.9
S-TT2	2.99	0.3	10.1
SU-M1	3.90	0.4	7.0
SU-NW1	3.19	0.0	10.2
SU-RDW1	2.57	0.0	6.9
SU-T1	2.64	0.0	11.7
SU-TF1	3.22	0.2	5.9
SU-TF2	3.67	0.4	7.7
SU-TPSC1	3.16	0.2	8.2
SU-TSF1	3.59	0.3	9.8
SY-HT1	5.36	3.2	10.1
SY-M1	3.18	0.4	10.1
SY-T1	3.00	0.4	10.7
T-T1	1.54	0.0	16.6
T-T2	1.96	0.0	13.7

4.2.2. Rheology Sensitivities

Shear Response

Because of the shear-dependent nature of the slurry samples, pre-shearing of the mixtures during rheometer testing is required in order to reach steady state values of shear response. The pre-shearing time of carrier fluid samples was determined by subjecting a sample to shear greater than the maximum test value while measuring torque response. Slurry carrier fluid S-TSRU1 was sheared for 30 minutes at 25 rad/s. Results of this testing are shown in Figure 4.4.

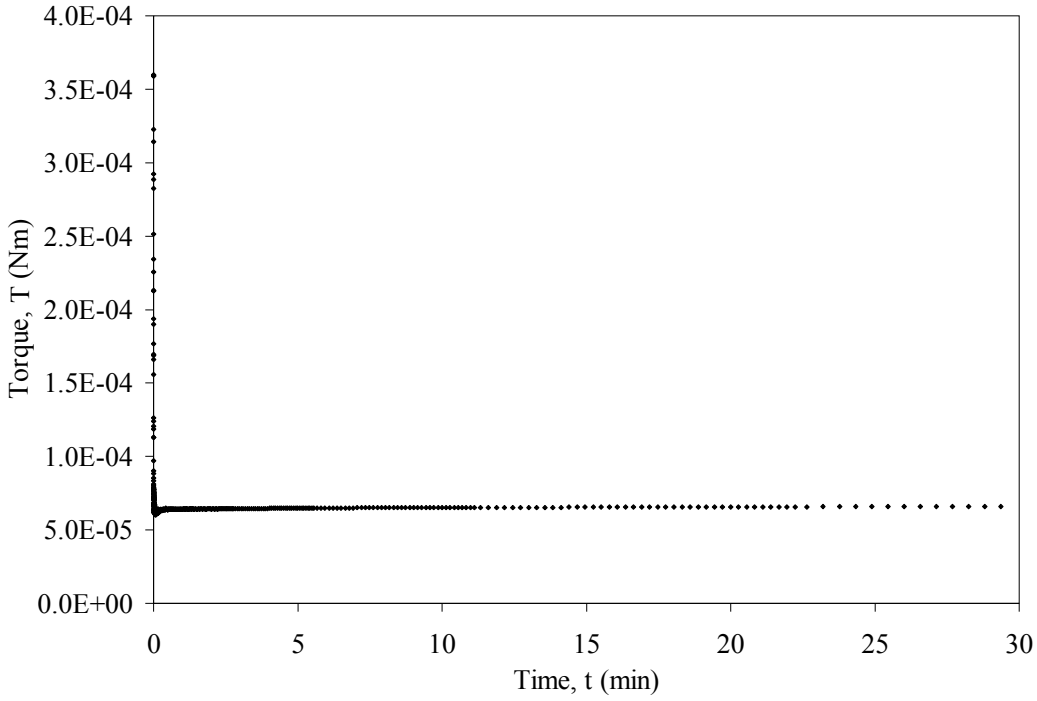

Figure 4.4: Shear response of Shell solvent recovery unit tailings (S-TSRU1) carrier fluid at 25 rad/s.

It can be seen that for the sample, steady values of torque can be seen in less than one minute of shearing. At shearing times greater than ten minutes torque response begins to decrease, likely due to settling within the rheometer. In order to avoid settling within the rheometer, carrier fluid samples were sheared for only one minute prior to testing.

Repeatability

One sample was selected to investigate the repeatability of viscosity results. Slurry SU-RDW1 sample was pre-sheared at 25 rad/s, and then shear was decreased stepwise from 20 to 0.1 rad/s. Immediately afterwards shear was increased stepwise from 0.1 to 20 rad/s to determine if any settling of solids occurred during testing. Results of this testing can be seen in Figure 4.5.

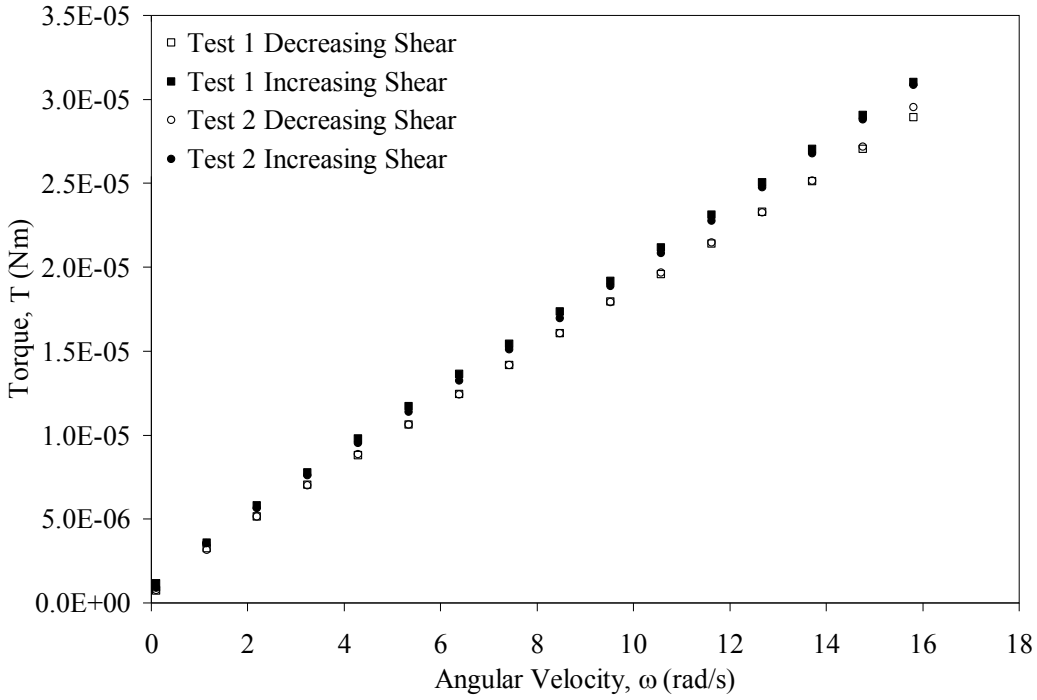

Figure 4.5: Repeatability of rheometer testing for Suncor ring dam water (SU-RDW1) carrier fluid.

It can be seen that results in the increasing and decreasing shear regions are not in agreement. Increasing shear torque values are consistently higher than those for decreasing shear. This is likely due to settling within the rheometer cup, and as a result only decreasing shear values were used in analysis. Results for slurry viscosity from the decreasing shear data were found to be very repeatable. Repeat testing was also completed for the filtrate water of slurry T-T. The results were found to be highly repeatable, in both increasing and decreasing shear regions. The results from four tests were found to vary less than 2% from the mean viscosity. Detailed results of this testing can be found in Appendix 6: Rheological Measurements of Carrier Fluid Slurries.

Reproducibility

Some of the slurry carrier fluid samples were recreated from raw sample in order to determine the reproducibility of results. Samples S-MFT2, S-TT3, S-TSRU3 and T-T3 were compared to S-MFT1, S-TT1 S-TSRU1 and T-T1 respectively. The results of these tests are shown in Table 4.8. The % difference from the original sample is shown in parentheses.

Table 4.8: Rheology reproducibility results.

Sample ID	Viscosity (mPas)	Yield Stress (Pa)	Standard Error
S-M2	2.26 (-9.6%)	0.1 (0.0%)	13.6
S-MFT2	5.94 (+2.8%)	0.9 (-11.1%)	9.4
S-TSRU3	2.04 (+4.1%)	0.0 (0.0%)	16.6
S-TT3	5.10 (+5.8%)	1.1 (0.0%)	5.4
T-T3	1.55 (+0.6%)	0.0 (0.0%)	15.5

It can be seen that the rheology results for the recreated samples are generally in good agreement with those of the original samples. This indicates that the sample preparation and rheology testing are reproducible.

4.3. Particle Size and Shape Analysis

4.3.1. Particle Size Measurements

In order to examine the behaviour of carrier fluid samples, FPIA measurements were made for slurries in their "natural" or aggregated state. To establish the degree of aggregation in each sample, measurements were also made on the carrier fluid samples in a dispersed state. The size of the primary particles and the concentration of the dispersed sample can be compared to aggregate size and concentration to provide information as to the strength of particle interactions in the carrier fluid.

Carrier fluid samples were diluted to a solids concentration of approximately 10 g/L using sample filtrate water and then tested in the FPIA. Images were taken of each particle entity and projected area was determined. The projected area for each entity is used to determine a circularity value and the diameter for an area-equivalent circle. Samples were later dispersed and measured in order to characterize the primary particles.

Figure 4.6 shows sample images of aggregates in slurry SY-HT. It can be seen that the aggregates are irregular in shape with loose (open) structure. Darker areas of the aggregates show individual particles and flocs. Lighter areas in the aggregate show the water that is trapped within the structure, which alters the overall particle concentration of the slurry.

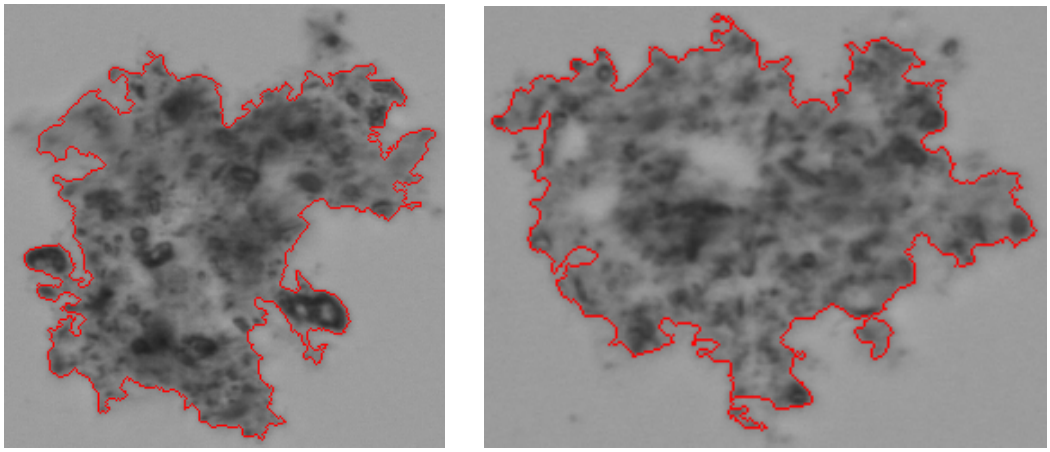

Figure 4.6: FPIA images of aggregates in Syncrude hydrotransport (SY-HT) sample.

Figure 4.7 shows a sample size distribution of particle entities in aggregated sample SY-HT. Size distributions for all aggregated samples tested can be found in Appendix 8: Particle Size Distributions of Carrier Fluid Samples. A distinct frequency peak is seen around 2µm for all samples due to the presence of a large number of non-aggregated or primary particles. This may be a result of non-interacting or inert materials in the carrier fluid samples. It could also be a consequence of the sample dilution required for FPIA testing. At lower fines concentrations, the strength of particle interactions is lower and aggregation is less likely to occur (Michaels & Bolger, 1964; Salama & Mikula, 1996).

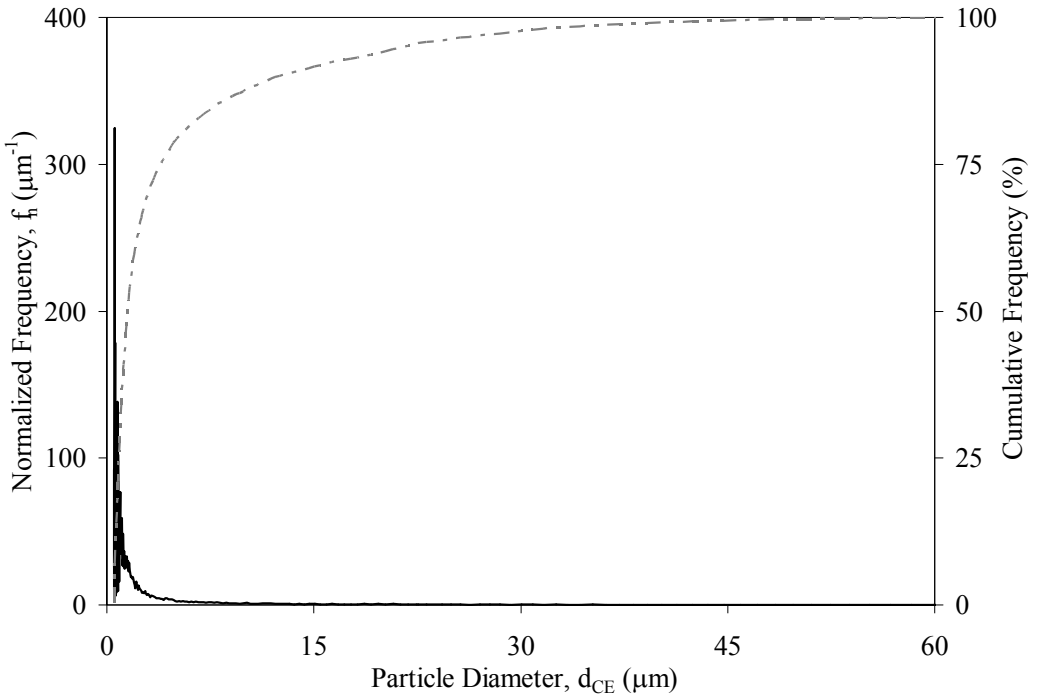

Figure 4.7: Particle size distribution of aggregated Syncrude hydrotransport (SY-HT) sample.

Table 4.9 shows a summary of the FPIA measurements obtained for the aggregated samples. The number and volume based mean area-equivalent diameters are given for each sample. The number base diameter d[1,0] places equal weighting on each particle and as a result is much smaller due to the large number of very small particles. The volume based diameter d[3,0] is larger due to the greater emphasis that is placed on the larger particles. The largest particles contribute most to the total solids volume and as a result are given greater weighting in the analysis.

Table 4.9: FPIA aggregated sample testing results.

Sample ID	d[1,0] (μm)	d[3,0] (μm)
S-M	4.5	14.2
S-MFT	5.5	15.3
S-TSRU	1.8	5.5
S-TT	4.1	16.0
SU-M	3.3	7.3
SU-NW	2.5	7.6
SU-RDW	3.1	10.2
SU-T	1.7	4.3
SU-TF	3.0	9.5
SU-TPSC	3.2	11.4
SU-TSF	3.2	11.6
SY-HT	4.4	13.0
SY-M	6.0	17.9
SY-T	4.1	13.9
T-T	2.4	10.6

Following the testing of carrier fluid samples in their "natural" or aggregated state, the samples were dispersed and re-tested to characterize the primary particles. Particle size and concentration for the carrier fluid in a dispersed state was compared to that of the sample in an aggregated state to determine the strength of particle interactions. Figure 4.8 shows sample images of the primary

particles in dispersed sample SY-HT. The larger particle images are typical of inert materials like silica sand. The smaller particle images are typical of clay materials. Both particle types are typically more circular than aggregates, and are much less irregular in shape.

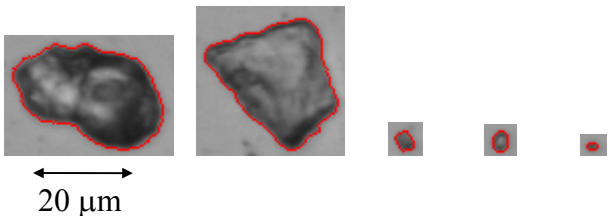

Figure 4.8: FPIA images of primary particles in dispersed Syncrude hydrotransport (SY-HT) sample.

Figure 4.9 shows a sample size distribution of primary particles in dispersed sample SY-HT. Information regarding sample dispersion can be found in Appendix 7: FPIA Settings and Sample Dispersion Information. Particle size distributions for all dispersed samples can be seen in Appendix 8: Particle Size Distributions of Carrier Fluid Samples.

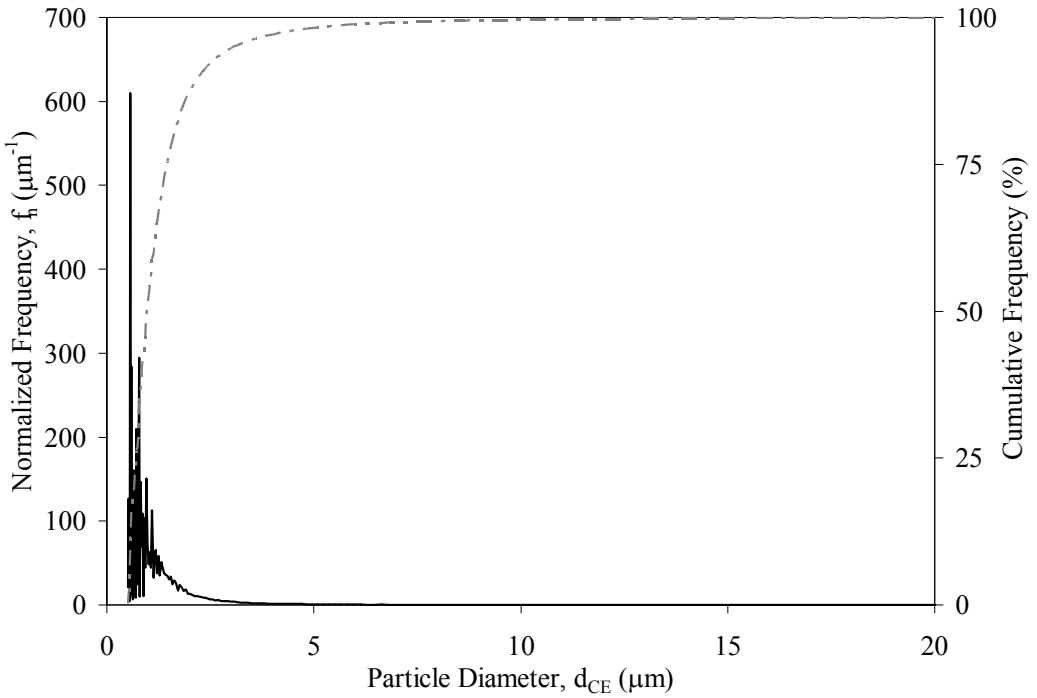

Figure 4.9: Particle size distribution of dispersed Syncrude hydrotransport (SY-HT) sample.

Table 4.10 shows a summary of the FPIA measurements obtained for the dispersed samples. The number based mean area-equivalent diameter and volume based mean area-equivalent diameter are given for each sample. As can be seen in comparing Table 4.9 with Table 4.10 both d[1,0] and d[3,0] are consistently smaller for the dispersed samples. Aggregation is occurring for the carrier fluid samples to varying degrees. It should also be noted that for the dispersed samples, the difference between d[1,0] and d[3,0] is much less pronounced than for the aggregated samples. This confirms the dispersion of the larger flocs and aggregates.

Table 4.10: FPIA dispersed sample testing results.

Sample ID	d[1,0] (μm)	d[3,0] (μm)
S-M	1.4	2.7
S-MFT	1.5	3.1
S-TSRU	1.6	3.6
S-TT	1.4	2.9
SU-M	1.4	2.9
SU-NW	1.6	3.0
SU-RDW	1.6	2.9
SU-T	1.6	3.5
SU-TF	1.5	2.9
SU-TPSC	1.5	3.2
SU-TSF	1.5	3.1
SY-HT	1.3	3.4
SY-M	1.3	2.8
SY-T	1.4	3.3
T-T	1.3	5.5

4.3.2. FPIA Measurement Sensitivities

Shear Response

When shear is initially applied to aggregating mixtures, aggregates are broken down into smaller flocs. After some time, an equilibrium or steady state is reached in terms of aggregate size (Vaezi et al., 2011). In order to determine a

suitable mixing time testing to reach a steady state aggregate size prior to FPIA, an idealized sample comprised of 4.0 g kaolin clay in 400 mL de-ionized water was tested. The sample was mixed at 400 RPM and sampled over the course of 90 minutes. Figure 4.10 shows the mean area-based diameter of aggregates over the elapsed mixing time. Raw data for these tests can be seen in Appendix 7: FPIA Test Settings and Sample Dispersion Information.

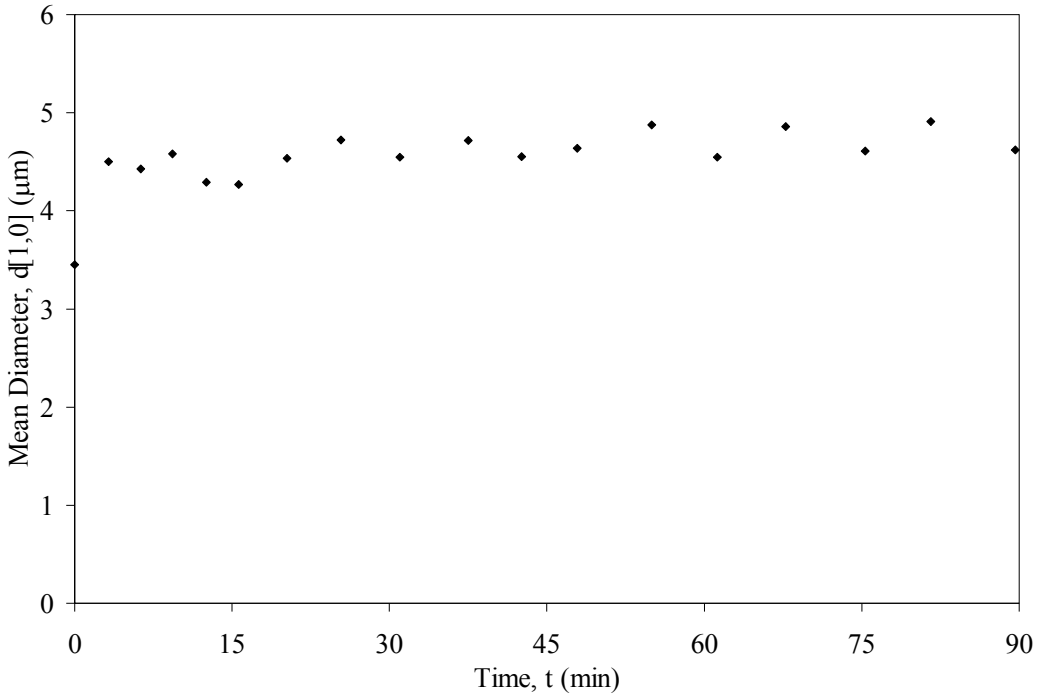

Figure 4.10: FPIA aggregate size for clay-water slurry tested over 90 minutes of mixing.

It can be seen that after approximately 20 minutes of mixing, less than 5% variation is seen in the mean aggregate size. Sixty minutes was selected as the pre-mixing time to ensure steady state was reached prior to testing.

4.3.3. Circularity Measurements

The circularity, or the ratio of the perimeter of a circle with an area equivalent to the aggregate to the actual aggregate perimeter, was also measured during FPIA testing. The circularity of the particles and aggregates was measured in order to see if the assumption of spherical aggregates is appropriate and to test the validity of using projected area measurements to determine solids concentration of the FPIA samples. Irregularly shaped particles will be less circular in shape and their volume can not be accurately determined using equations for spherical entities. Circularity is calculated using Equation 3.6. A sample distribution of circularity values for the aggregated slurry sample SY-T is shown in Figure 4.11.

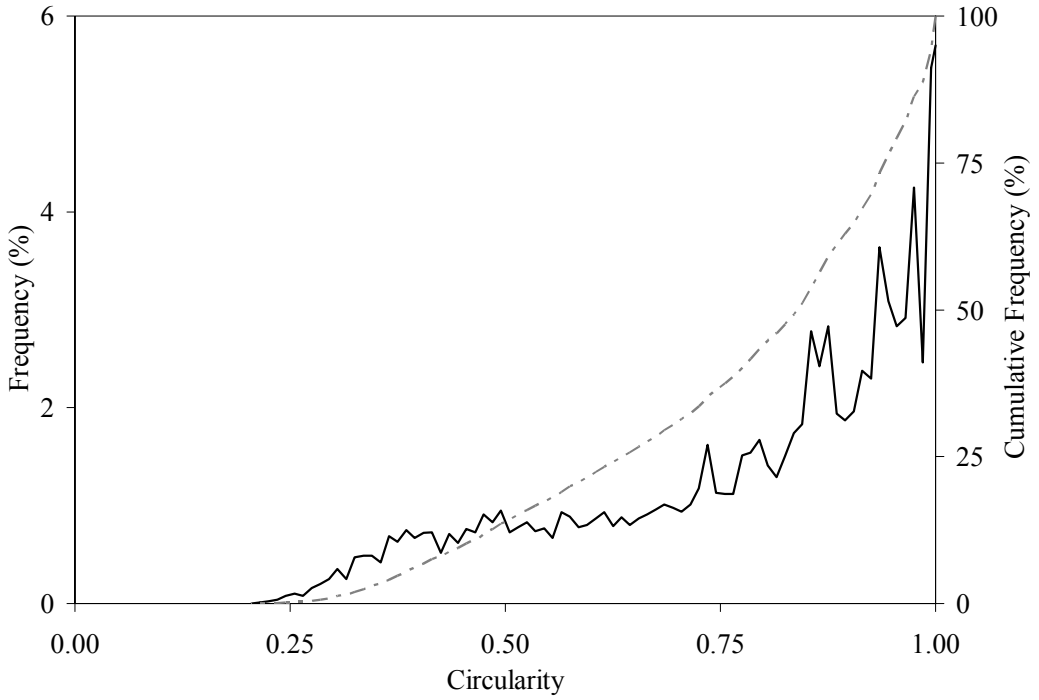

Figure 4.11: Circularity frequency plot of aggregated Syncrude tailings (SY-T) sample.

It can be seen that the sample had a wide range of values and thus the flocs cannot be considered to be spherical in shape. As a result, the FPIA measurements of particle projected area were not used directly to determine the aggregate volume and concentration of carrier fluid samples.

Figure 4.12 shows a sample distribution of circularity values for dispersed slurry sample SY-T.

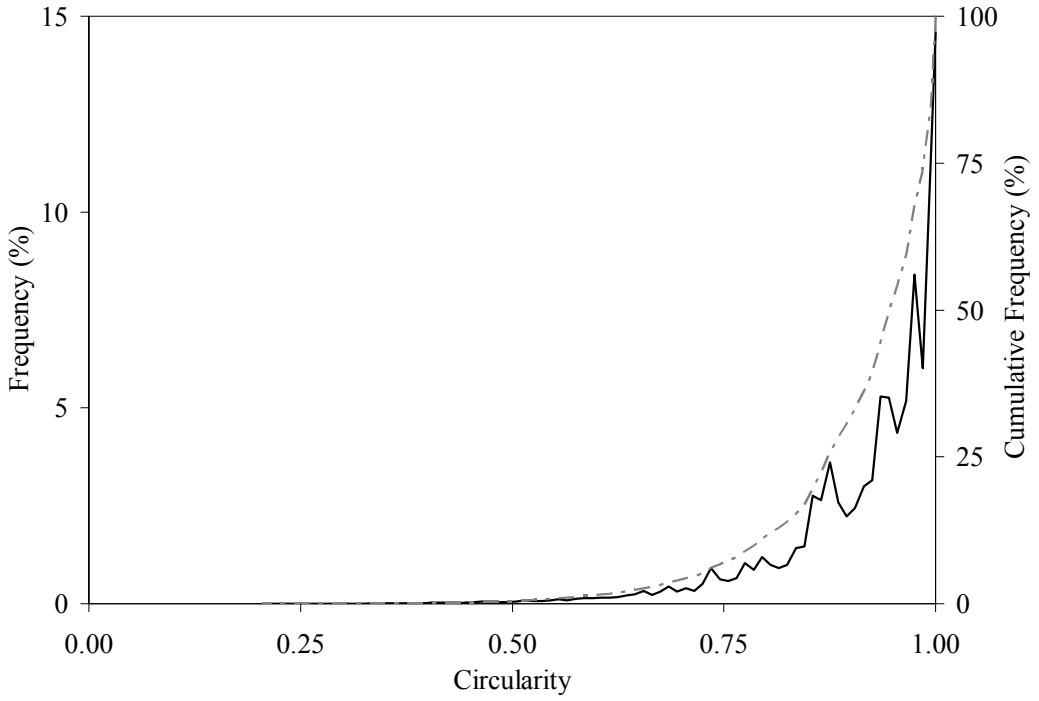

Figure 4.12: Circularity frequency plot of dispersed Syncrude tailings (SY-T) sample.

It can be seen that the sample had a much narrower distribution of circularity values. The primary particles can be considered to be nearly circular in shape.

A summary of the mean circularity data measured for the samples in both their aggregated and dispersed state is shown in Table 4.11. Shape distributions for all samples can be found in Appendix 9: FPIA Shape Distributions of Carrier Fluid Samples.

Table 4.11: Mean circularity of diluted carrier fluid samples.

Sample ID	Mean Circularity	
	(Aggregated)	(Dispersed)
S-M	0.780	0.914
S-MFT	0.768	0.911
S-TSRU	0.888	0.918
S-TT	0.832	0.910
SU-M	0.818	0.883
SU-NW	0.863	0.931
SU-RDW	0.818	0.931
SU-T	0.891	0.904
SU-TF	0.798	0.892
SU-TPSC	0.807	0.891
SU-TSF	0.808	0.894
SY-HT	0.780	0.918
SY-M	0.788	0.908
SY-T	0.811	0.900
T-T	0.871	0.924

The lower values of mean circularity for the aggregated samples indicate that the flocs and aggregates should not be considered spherical. The high values of circularity for the dispersed samples indicate that the assumption of spherical primary particles should hold true. This should be verified by comparing the fines concentration measured by the FPIA with that determined using Dean Stark analysis.

4.3.4. Particle Concentration in the FPIA

The particle concentrations obtained using the FPIA for dispersed samples were compared to those determined from Dean Stark analysis. This was done to ensure that the FPIA does not cause dilution of the sample and to determine if aggregate concentration could be determined directly from FPIA results. Samples were diluted to a concentration of approximately 10 g/L then dispersed using the method described previously, and three FPIA tests were completed. The particle size distributions obtained for one test are shown in Figure 4.13.

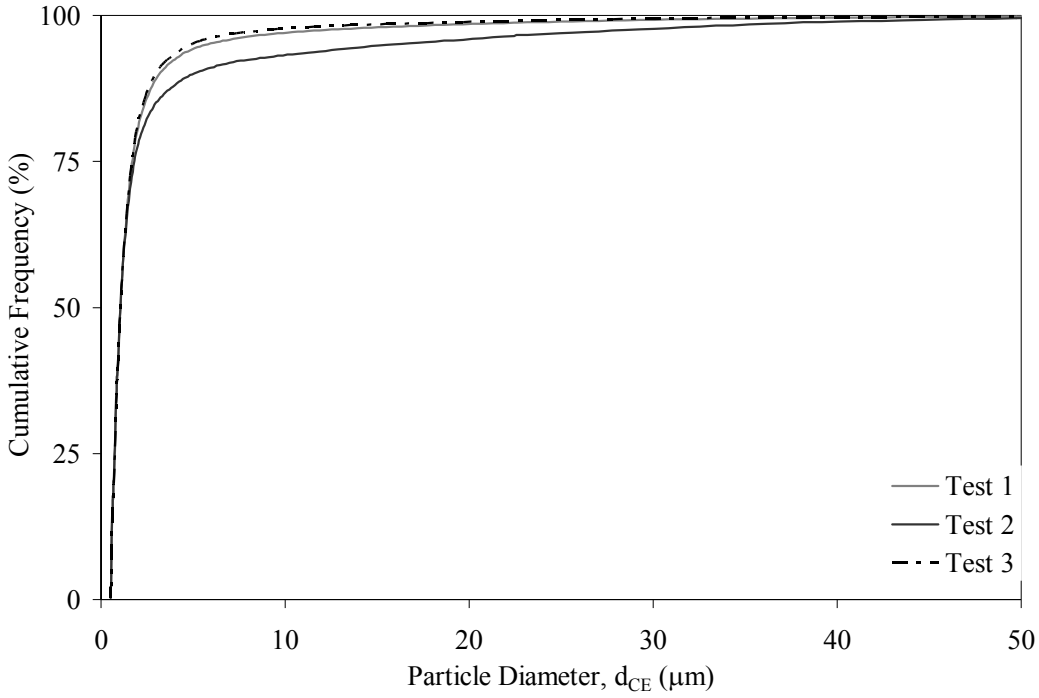

Figure 4.13: FPIA particle size distribution of dispersed Total tailings (T-T) sample.

Using the assumption of spherical particles, the mean solids concentration indicated by the FPIA was 2.1 vol. %. The solids concentration for carrier fluid T-T1 determined by Dean Stark testing was 1.8 vol. %. This would appear to indicate that dilution is not occurring within the FPIA. Figure 4.14 shows a comparison of solids content determined by Dean Stark analysis and FPIA testing.

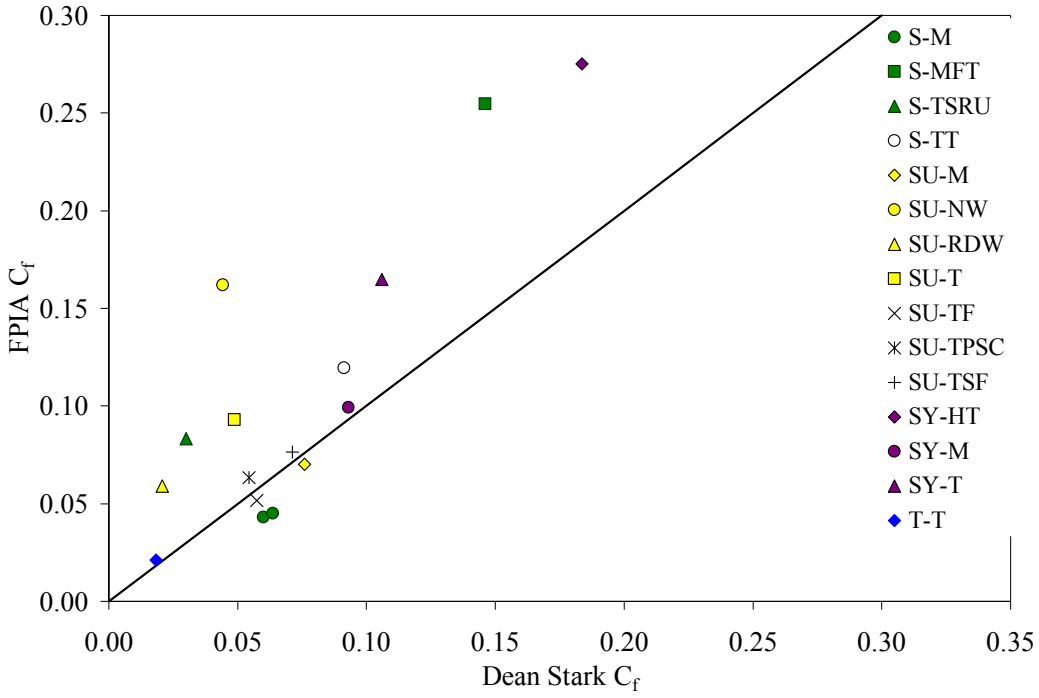

Figure 4.14: Comparison of fine solids concentrations from Dean Stark laboratory analysis and FPIA measurements.

Although the volume fractions for some samples found from FPIA agree with those found through Dean-Stark analysis, many do not. For small errors in concentration, the difference would be insignificant to further data analysis. It is possible that samples were not fully dispersed in the FPIA and this would lead to the appearance of higher concentrations due to the water trapped within the structure of aggregates. There may also be error in the Dean Stark measurements. Since limited testing has been done for the FPIA using aggregated samples, Dean Stark results were selected to represent the solids content of all carrier fluid samples. It is also worth noting that aggregate concentrations determined directly from FPIA results for samples did not yield reasonable estimates. Some of the

calculated aggregate concentrations were higher than C_{max}, the maximum solids concentration in a packed bed, which is not physically possible. The two-dimensional measurements obtained by the device were not sufficient for characterizing aggregate dimensions due to their non-spherical nature. FPIA results indicated aggregates have a lower and much wider range of circularity values than the dispersed primary particles. Consequently, an area based approach was chosen to determine the concentration of aggregates.

4.3.5. Aggregate to Fines Ratio Determination

Due to the irregularity of the aggregate shape, it was not appropriate to assume spherical particles. Therefore, aggregate concentration could not be determined directly from Equation 2.18. Instead the ratio of the total projected area for aggregated carrier fluid to the total projected particle area for dispersed carrier fluid was used as a conversion factor to determine aggregate concentrations for all samples. The definition of C_{agg} is given by Equation 4.2 where the concentration of fines or primary particles, C_f, is the value determined through Dean Stark analysis:

$$C_{agg} = \frac{\Sigma A_p \text{ for Aggregated Sample}}{\Sigma A_p \text{ for Dispersed Sample}} \times C_f \qquad \textbf{(4.2)}$$

The total particle projected area and aggregate to fines conversion ratio for each sample is shown in Table 4.12.

Table 4.12: FPIA aggregate to fines ratio.

Sample ID	Total Projected Area (Aggregated, m^2)	Total Projected Area (Dispersed, m^2)	C_{agg}/C_f
S-M	5.49×10^{-7}	2.30×10^{-7}	2.39
S-MFT	9.87×10^{-7}	4.00×10^{-7}	2.47
S-TSRU	1.94×10^{-7}	1.50×10^{-7}	1.29
S-TT	3.05×10^{-7}	3.21×10^{-7}	0.95
SU-M	1.73×10^{-7}	1.47×10^{-7}	1.18
SU-NW	3.31×10^{-7}	2.72×10^{-7}	1.22
SU-RDW	2.61×10^{-7}	2.33×10^{-7}	1.12
SU-T	1.85×10^{-7}	1.58×10^{-7}	1.17
SU-TF	2.12×10^{-7}	1.26×10^{-7}	1.68
SU-TPSC	1.98×10^{-7}	1.62×10^{-7}	1.23
SU-TSF	2.01×10^{-7}	1.90×10^{-7}	1.06
SY-HT	7.93×10^{-7}	2.70×10^{-7}	2.94
SY-M	7.16×10^{-7}	2.93×10^{-7}	2.44
SY-T	6.21×10^{-7}	3.05×10^{-7}	2.04
T-T	6.67×10^{-7}	3.29×10^{-7}	2.02

4.4. Correlations for Relative Viscosity

4.4.1. Relative Viscosity and Fines Concentration

Current industrial practice is to predict the viscosity of a sample using overall fine solids concentration. Relative viscosity for each carrier fluid sample was calculated using Equation 2.1. The relative viscosity as a function of fines concentration is shown in Figure 4.15. The trend determined using statistical analysis, along with a 95% confidence interval, is given in the figure.

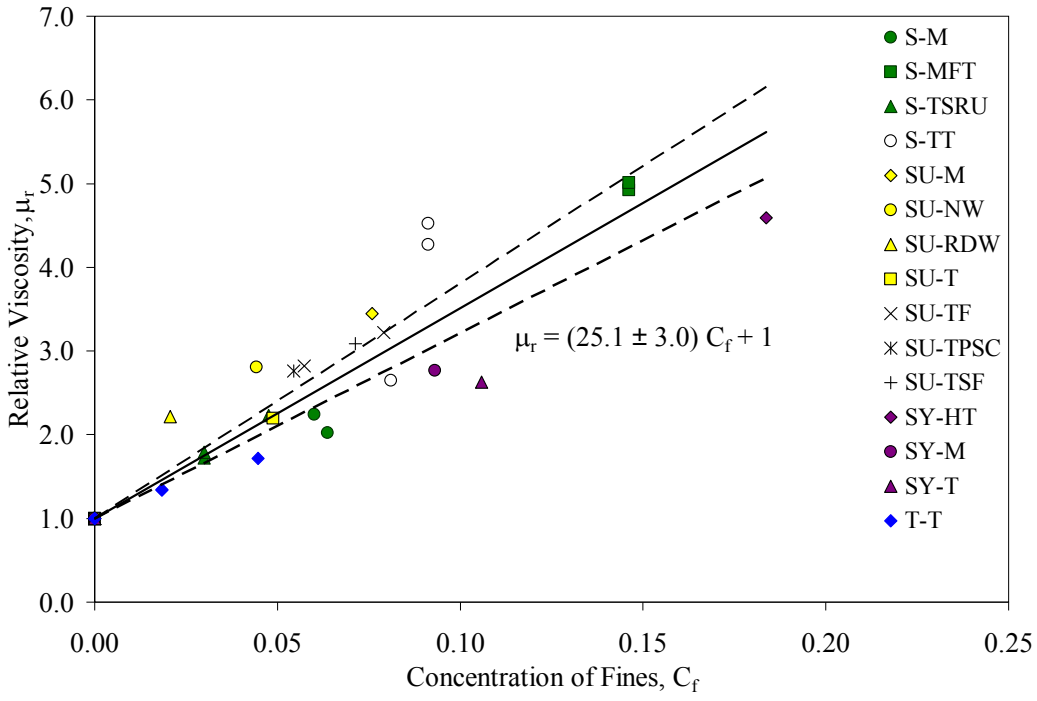

Figure 4.15: Carrier fluid relative viscosity as a function of fine solids concentration.

There is scattering of the data shown in Figure 4.14 and many samples fall outside of the 95 % confidence interval of the linear correlation. As a result, samples were

re-examined based upon key water characteristics, namely pH. Due to increased dispersion of aggregates at high pH values, the samples were divided into two groups – samples with pH ≈ 9 and samples with pH < 9. As discussed in Chapter 2, the data were fitted with an exponential function due to the strong inter-particle interactions that occur in aggregating suspensions. Carrier fluid S-TT was examined separately from other samples, as the addition of chemical flocculants is likely to cause behaviour not seen with the other carrier fluid samples. The data for S-TT are shown in Figure 4.16.

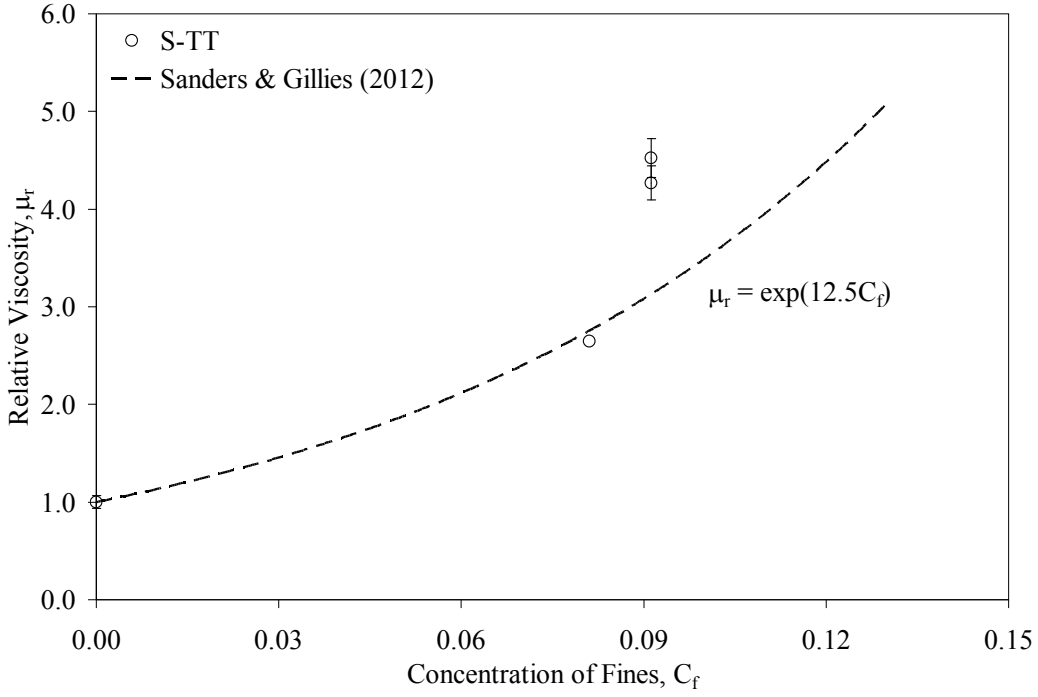

Figure 4.16: Relative viscosity of Shell thickened tailings (S-TT) carrier fluid sample.

It can be seen that the data do not agree with the trend suggested by Sanders & Gillies (2012). For this sample, relative viscosity appears to increase at a greater rate than predicted by Sanders & Gillies (2012). However, this data set is too small to provide anything more than this tentative observation. The addition of polymer flocculants leads to increased aggregate size and slurry viscosity (Liu & Masliyah, 1996; Mewis & Wagner, 2012).

The remaining data were separated into two groups, one with pH values greater than or equal to 9, and the other with pH values below 9. These data were re-examined and are shown in Figures 4.17 and 4.18 respectively.

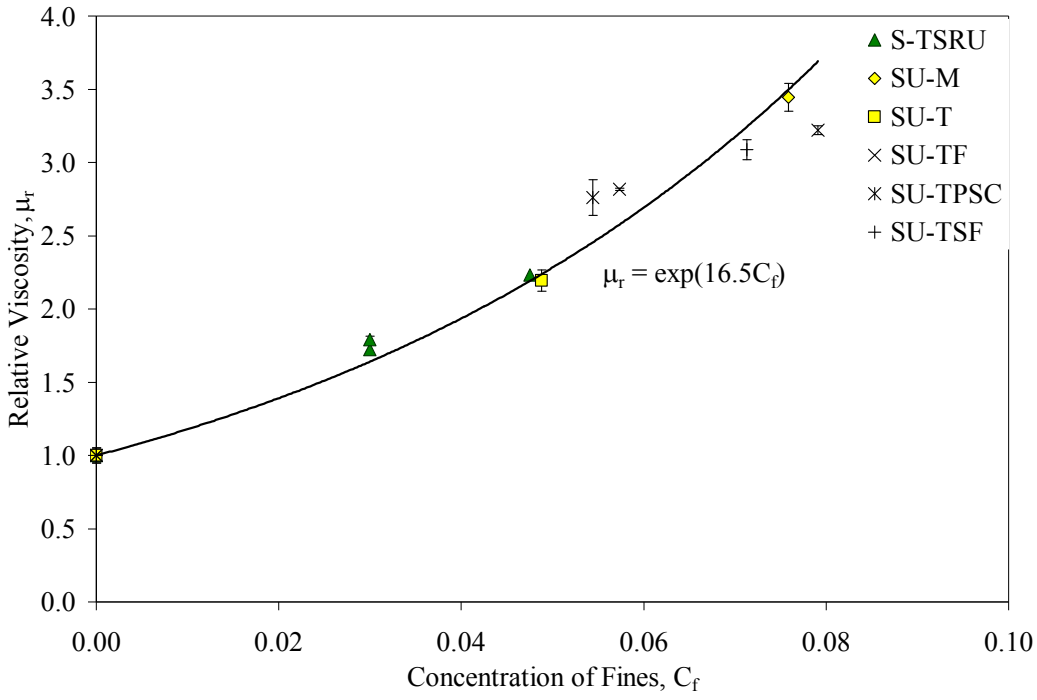

Figure 4.17: Relative viscosity with respect to fines content for carrier fluid samples with pH ≈ 9.

It can be seen that samples with pH 9 can also be described using an exponential relationship; however, again higher relative viscosity values are indicated than those predicted by Sanders & Gillies (2012). It is also of note that the viscosity values seen for these samples are lower than those indicated for the idealized samples at pH 9 studied by Shahmirzadi (2012). This is likely due to the presence of relatively inert sand solids and the differences in water chemistry: Shahmirzadi used de-ionized water with added Ca^{2+} while the samples studied here involve process affected water.

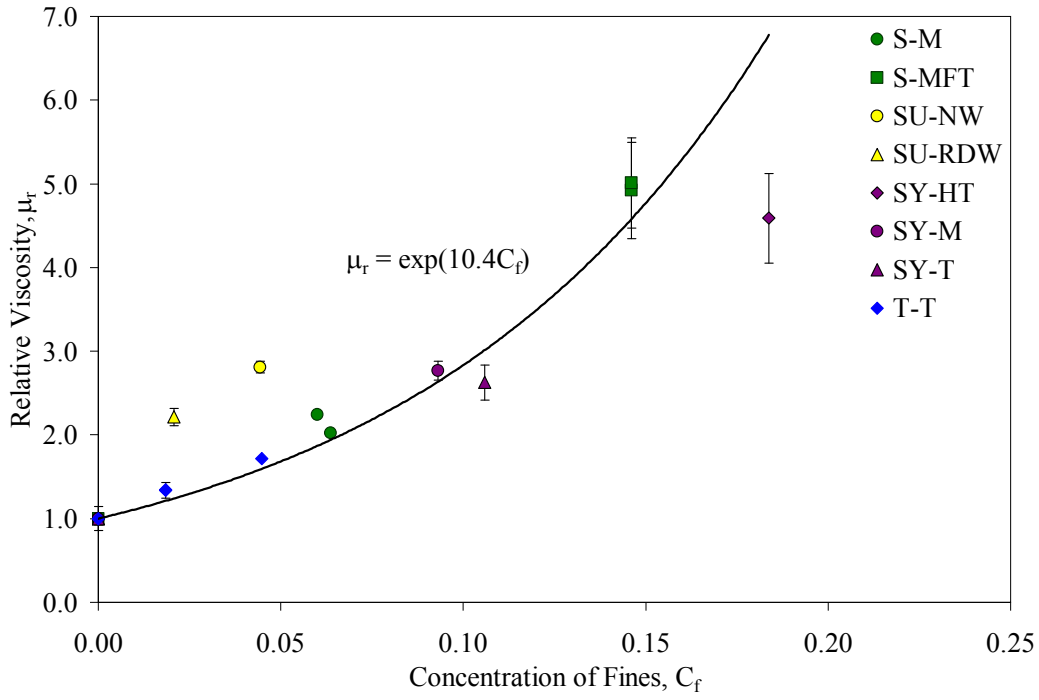

Figure 4.18: Relative viscosity with respect to fines content for carrier fluid samples with pH < 9.

It can be seen that samples with pH less than 9.0 can be described using an exponential trend, however viscosity values are lower than those predicted using the correlation given by Sanders & Gillies (2012). Due to the larger range of pH values the data is scattered. Figures 4.17 and 4.18 are clear in demonstrating the importance of water chemistry. The samples tested also demonstrate viscosity increasing with pH. This effect has previously been seen by Sumner et al. (2000) in the testing of model tailings. It is believed that increasing pH will cause slurries to deflocculate until a minimum viscosity is reached. At this point, further deflocculation only serves to narrow the particle size distribution and increase the presence of extremely fine particles. These fine particles strongly affect the viscosity of samples, and as a result increase the measured viscosity.

4.4.2. Relative Viscosity and Aggregate Concentration

Aggregate concentration was determined using Equation 4.2. Relative viscosity was correlated with aggregate concentration and is shown in Figure 4.19. Because it is expected that the interactions between aggregates would be much weaker than for primary particles, the data were fitted with a linear equation. Note that sample S-TT is excluded from this analysis.

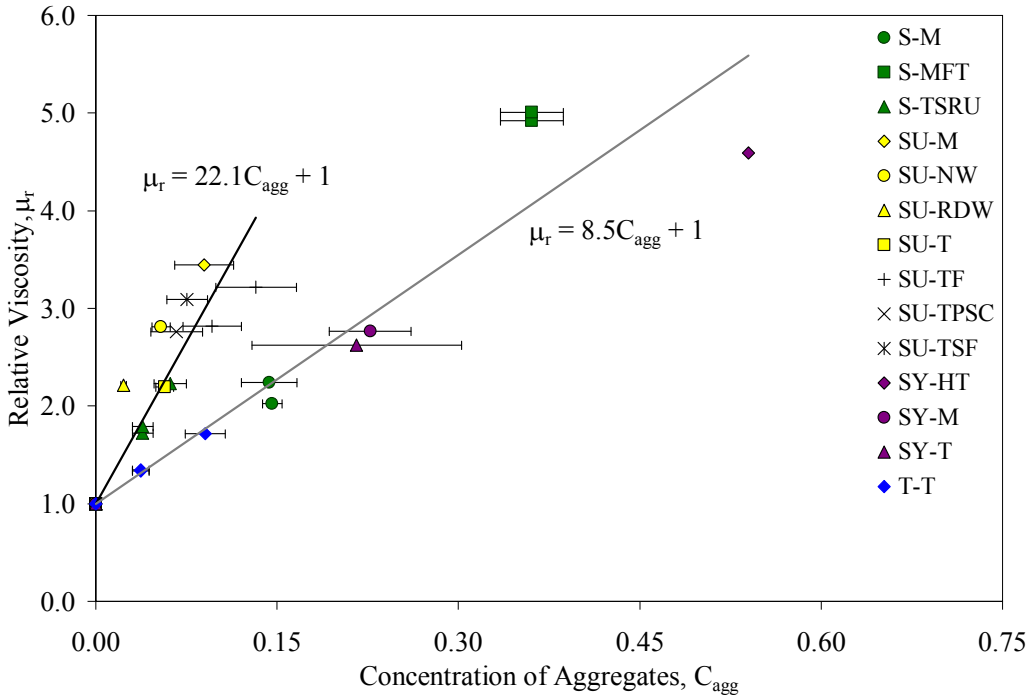

Figure 4.19: Carrier fluid relative viscosity as a function of aggregate concentration determined by FPIA measurements.

It is clear that the aggregated samples could not be described using a single correlation. Two distinct trends were indicated. Neither trend agrees with the relationship found by Shahmirzadi (2012). Both correlations have higher slope values than the Einstein equation. This strongly indicates that the aggregate bodies interact with one another. As slope increases in the linear correlation, stronger interaction between aggregates in the samples is indicated.

Due to the limitations of the FPIA it is possible that the method for determining aggregate fraction is insufficient. The total effect of dilution on aggregate concentration is not fully understood. It is important to note that while viscosity

measurements were made at in-situ concentrations, FPIA measurements required sample dilution. Dilution may cause significant dispersion of aggregates and flocs resulting in aggregate concentrations lower than those seen industrially. Although the qualitative effects are known, the constraints of the FPIA mean that quantitative analysis of the change to aggregate size and contribution with respect dilution can not be measured.

It is apparent from these results that there are mechanisms besides aggregate size and concentration which greatly contribute to carrier fluid viscosity. The split between the carrier fluid samples into two correlations would suggest that there is a key difference between the two groups. It is important to understand the variations between carrier fluid samples in order to determine why two correlations are apparent for seemingly similar materials. As discussed in Chapters 1 and 2, some factors contributing to carrier fluid viscosity include: solids mineralogy, particle shape distribution and water chemistry. Statistical analysis was completed on water chemistry data to determine key factors that may be responsible for rheological behaviour.

4.4.3. Relative Viscosity and Calcium Ion Concentration

Multiple linear regression analysis was performed for carrier fluid relative viscosity with respect to fines concentration, aggregate concentration and each water chemistry variable. A weak relationship was found between viscosity and the concentration of many of the dissolved ions (Fe^{3+}, Al^{3+}, K^{+}, Na^{+}, Cl^{-}, SO_4^{2-}, NO_3^{-}, HCO_3^{-}, and CO_3^{2-}). Stronger correlation was seen between viscosity and fines concentration, aggregate concentration, and divalent cation concentration (Mg^{2+} and Ca^{2+}). Although carrier fluid viscosity correlates strongly with aggregate concentration, a better model fit was found using fines concentration. Statistical analysis of the relevant variables indicated that the strongest relationship occurred with fines concentration and calcium ion content (R^2 = 0.912). The weakest relationship for the relevant variables was found using aggregate concentration and magnesium ion content as correlating parameters (R^2 = 0.616). It is of note that for some water chemistry variables only a narrow range of measured values was seen. A limitation of the regression analysis is that a narrow range of values would cause the variables to be seen as statistically irrelevant when in reality the variable may indeed affect carrier fluid viscosity. The measured range of all variables considered in multiple linear regression analysis is given in Table 4.13.

Table 4.13: Measured range of variables considered in regression analysis.

Variable	Range	Units
C_{agg}	0.023 – 0.540	–
C_f	0.018 – 0.184	–
pH	8.53 – 9.30	–
Conductivity	0.57 – 3.39	MS/cm
$[Fe^{3+}]$	0.0 – 0.5	mg/L
$[Al^{3+}]$	0.0 – 2.9	mg/L
$[Ca^{2+}]$	5.7 – 73.2	mg/L
$[K^{+}]$	11.5 – 31.8	mg/L
$[Na^{+}]$	292.0 – 3951.3	mg/L
$[Mg^{2+}]$	4.8 – 35.7	mg/L
$[Cl^{-}]$	53.6 – 807.5	mg/L
$[SO_4^{2-}]$	21.0 – 526.3	mg/L
$[NO_3^{-}]$	0.0 – 0.2	mg/L
$[HCO_3^{-}]$	129.7 – 737.3	mg/L
$[CO_3^{2-}]$	0.0 – 108.0	mg/L
Ionic strength	0.02 – 0.11	mol/L

Multiple linear regression provided a correlation, which shows carrier fluid relative viscosity as a function of fines concentration and calcium molarity:

$$\mu_r = 1.2 + 30.0\,C_f - 1356.8\left[Ca^{2+}\right] \qquad \textbf{(4.3)}$$

Equation 4.3 was developed using samples with greater than 1% fines by volume at "natural" concentrations; all laboratory-altered samples were excluded from regression analysis. This equation is not valid for the prediction of viscosity for very dilute samples or process water. As the solids content approaches zero, the viscosity should be equal to the process water viscosity. An alternative correlation was developed to ensure a relative viscosity of 1 is calculated for very dilute samples:

$$\mu_r = 1.0 + 28.4\,C_f - 5900.6\left[Ca^{2+}\right] \times C_f \qquad \textbf{(4.4)}$$

The correlation given by Equation 4.4 ensures the boundary conditions of the system are met, however the strength of the model fit decreases ($R^2 = 0.834$) and carrier fluid viscosity values are less accurately predicted. It is unlikely that the correlation would ever be used to predict the viscosity of very dilute, water-like suspensions and as a result it is more prudent to use Equation 4.3 to predict carrier fluid viscosity.

From Equation 4.3 it can be seen that as fines content increased or calcium ion concentration decreased, particle interactions grew stronger and carrier fluid viscosity increased. The negative coefficient on the calcium concentration term is somewhat unexpected. Research by Michaels & Bolger (1964), Zbik (2008), and Shahmirzadi (2012) indicates that the addition of calcium ions should cause an increase in aggregation and the resulting carrier fluid viscosity. Viscosity values predicted by Equation 4.3 are plotted against measured values in Figure 4.20.

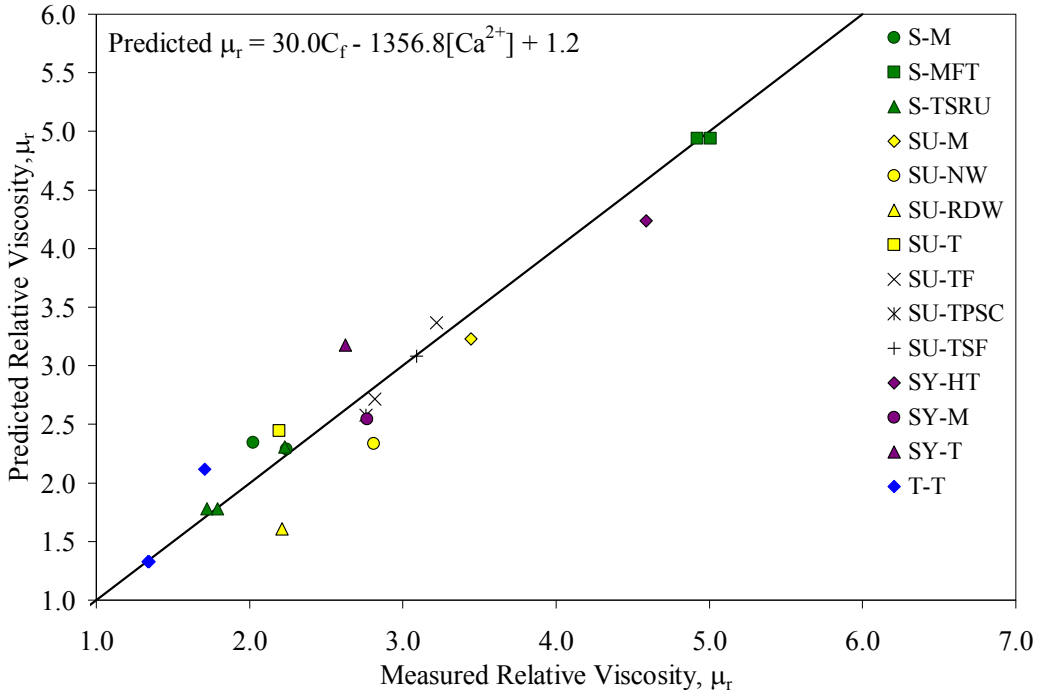

Figure 4.20: Measured relative viscosity compared with values predicted using fines concentration and calcium ion content.

Aggregate concentration provide a good indication of the strength of particle interactions and the resulting carrier fluid viscosity; however, due to the strength

of the correlation seen for fines content and the fact that fines content is currently measured in industrial settings, fines concentration was selected for correlation purposes. It can be seen from Figure 4.20 that model predicted carrier fluid viscosity values are in good agreement with measured viscosities. The relationship presented provides a simple method to predict carrier fluid viscosity using fines concentration and calcium ion content, both of which are measured industrially.

5. Conclusions and Recommendations

5.1. Contributions of this Study

Measurement of the rheological behaviour of industrial carrier fluid is difficult and time intensive. Current pipeline design utilises empirical correlations to predict carrier fluid rheology, however these correlations can be problematic due to the use of overall fines concentration as the only correlating parameter. Agglomeration occurs between fine particles in the carrier fluid, and these particle interactions determine the rheology of the material. Factors such as fines concentration, water chemistry, and solids mineralogy are highly variable in oil sands slurries and determine the degree of aggregation fine particles As a result a method was developed to more accurately predict the rheology of these complex slurries. Viscosity measurements were made for the carrier fluid of a number of industrial slurries providing quantitative viscosity data for these particular slurries. In order to extend the usefulness of this work beyond this specific set of oil sands slurries analysis was completed to allow for the prediction of carrier fluid samples using key physical characteristics. A tentative correlation was developed to relate the relative viscosity of carrier fluid to fines concentration and calcium ion content, both of which are currently measured in industrial settings.

5.2. Conclusions

The primary objectives of this research was to measure the rheological behaviour of the carrier fluid of industrial oil sands slurries and develop a method that can be used industrially to determine carrier fluid rheology from aggregate size. A

number of industrial carrier fluid samples were taken from various points throughout the extraction process. The samples were prepared and viscosity was measured using a concentric cylinder rheometer. An exponential relationship was indicated between overall fines concentration and viscosity. This was in agreement with previous research (A.D. Thomas, 1999 ; Shook et al., 2002) which emphasized the importance of particle interactions in determining rheological behaviour. No single relationship could be found to describe the viscosity of all carrier fluid samples with respect to fines content. Sample viscosity increased with overall fines concentration however rheological behaviour proved to be extremely dependent on the water chemistry of the carrier fluid. Carrier fluid with high pH values had smaller aggregates and lower viscosity values for samples of comparable fines concentration. At lower pH values, larger aggregates and higher viscosity were seen. This indicated that there were parameters in addition to fines content that affected rheological behaviour and must be considered in prediction of carrier fluid viscosity.

The second objective of this work was to correlate carrier fluid viscosity with aggregate concentration, which reflects changes in particle interactions caused by variations in concentration, solids mineralogy and water chemistry. The particle size and shape distributions of samples were measured using the Flow Particle Image Analyzer (FPIA), an automated optic device. Size and shape analysis was completed for samples in both aggregated and dispersed states. Aggregate concentration was determined using the ratio of total projected area for particle

entities in samples in the aggregated and dispersed states. When the carrier fluid relative viscosity was examined with respect to aggregate concentration two distinct linear functions were seen. However, neither trend agreed with the results seen by Shahmirzadi (2012) for aqueous kaolin suspensions, which utilized de-ionized water as the suspending fluid. The effect of water chemistry was again made evident by the results of this study.

The final objective of this work was to provide a method to predict carrier fluid in industrial settings. Carrier fluid viscosity was examined with respect to overall fines concentration as well as aggregate size and concentration. Statistical analysis was completed on the data to identify important relationships between water chemistry and viscosity. The strongest relationship for carrier fluid relative viscosity was found using fines content and calcium ion concentration as correlating parameters. Multiple linear regression analysis was used to identify the following relationship between carrier fluid relative viscosity, fines concentration and calcium ion concentration:

$$\mu_r = 1.2 + 30.0\, C_f - 1356.8 \left[Ca^{2+}\right]$$

Although this tentative empirical correlation provides better prediction of carrier fluid viscosity than current methods, it is important to note that additional work is required to provide a more robust analysis of oil sand extraction slurry materials.

5.2. Recommendations for Future Work

Future work should be done to further examine the effect of solids mineralogy on the carrier fluid rheology. Solids mineralogy is expected to vary greatly between samples. Industrial carrier fluid should be characterized to determine the relative content of commonly occurring clays. Methods that could be used to accomplish this include x-ray diffraction combined with x-ray fluorescence (Kaminsky, et al., 2009) or methylene blue indexing which could give a measure of the surface activity of the solids. Additional statistical analysis should be performed to examine possible relationships between viscosity and individual mineral concentrations.

The dissolved ion content of samples should be further studied. Of particular interest is the total concentration of divalent cations other than calcium. The presence of divalent cations changes solid surface chemistry and can have drastic effects on aggregate size and shape distributions as well as overall aggregate density. Measurement of the total concentration of divalent cations should be made by ion chromatography. Statistical analysis should be done to determine if this parameter (along with fines or aggregate concentration) correlates more strongly with relative viscosity.

Additional work to verify the accuracy of FPIA measurements is critical. The effects of sample dilution should be quantified using industrially accepted methods such as: settling tests, laser diffraction, and other automated imaging

techniques. A comparison of aggregate size and shape results from the FPIA should be made with respect to these accepted methods at dilute conditions. From this data, the size of aggregates could be inferred from concentrated test results of the industrially accepted techniques.

References

Adeyinka, O.B., Samiei, S., Xu, Z. & Masliyah, J.H. (2009). Effect of Particle Size on the Rheology of Athabasca Clay Suspensions. *The Canadian Journal of Chemical Engineering*, 87(3), 2009

Bessendorfer, G. & Roosen, A. (2008). Particle Shape and Size Effects on Anisotropic Shrinkage in Tape-Cast Ceramic Layers. *Journal of the American Ceramic Society*, 91(8), 2514-2520.

Bird, R.B., Stewart, W.E., & Lightfoot, E.N. (2002) Transport Phenomena, (2nd Ed.). New York, NY: John Wiley & Sons Inc.

Broughton, G. & Windebank, C.S. (1938). Agglomeration and Viscosity in Dilute Suspensions. *Industrial and Engineering Chemistry*, 30(4), 407-409.

Bulmer, J.T. & Starr, J. (Eds.). (1979). *Syncrude Analytical Methods for Oil Sand and Bitumen Processing*. Edmonton, AB: Alberta Oil Sands Technology and Research Authority.

Canadian Association of Petroleum Producers. (2012). The Facts on Oilsands: Upstream Dialogue. Retrieved August 1, 2012 from http://www.capp.ca/UpstreamDialogue/OilSands/Pages/default.aspx.

CanmetENERGY. (2003). *Naptha Recovery Potential of Oleophilic Beads,* confidential report to Gradek Energy Inc., May 2003.

Carlson, M.R. (2006). *Practical Reservoir Simulation – Using, Assessing, and Developing Results*. Tulsa, OK: PennWell.

Cleyle, P. (2012). *Personal Communication*, February 21, 2013.

Coussot, P, & Piau, J.M. (1994). On the behaviour of fine mud suspensions. *Rheologica Acta*, 33(3), 175-184.

Gradek, T. (2010). *U.S. Patent No. 2010/0072110 A1*. Washington, DC: U.S. Patent and Trademark Office.

Hao, T. (2008). Viscosities of liquids, colloidal suspensions, and polymeric systems under zero or non-zero electric field. *Advances in Colloid and Interface Sciences*, 142(1-2), 1-19.

Kaminsky, H.A., Etsell, T.H., Ivey, D.G., & Omotoso, O. (2009). Distribution of Clay Minerals in the Process Streams Produced by the Extraction of Bitumen from Athabasca Oil Sands. *The Canadian Journal of Chemical Engineering*, 87(1), 85-83.

Komabayashi, T. & Spangberg, L.S.W. (2008a). Particle Size and Shape Analysis of MTA Finer Fractions Using Portland Cement. *Journal of Endodontics*, 34(6), 709-711.

Komabayashi, T. & Spangberg, L.S.W. (2008b). Comparative Analysis of the Particle Size and Shape of Commercially Available Mineral Trioxide Aggregates on Portland Cement: A Study with a Flow Particle Image Analyzer. *Journal of Endodontics*, 34(1), 94-98.

Litzenberger, C.G. & Sumner, R.J. (2004). Flow behaviour of kaolin clay slurries. *Proceedings of the 16th International Conference on Hydrotransport held in Santiago, Chile, 26-28 April 2004* (pp. 77-92). Bedfordshire, UK: BHR Group Limited.

Liu, S. & Masliyah, J.H. (1996). Rheology of Suspensions. In L.L. Schramm (Ed.) *Suspensions: Fundamentals and Applications in the Petroleum Industry* (pp. 107-176). Washington, DC: American Chemical Society.

Macey, M.G. (2007) Principles of Flow Cytometry. In M.G. Macey (Ed.) *Flow Cytometry: Principles and Applications* (pp. 1-15). Totowa, NJ: Humana Press Inc.

Masliyah, J.H., Zhou, Z., Xu, Z., Czarnecki, J. & Hamza, H. (2004). Understanding Water-Based Extraction from Athabasca Oil Sands. *The Canadian Journal of Chemical Engineering*, 82(4), 628-654.

Masliyah, J.H. (2010). *Course Notes – Fundamentals of Oil Sands Extraction.* Edmonton, AB: Department of Chemical and Materials Engineering, University of Alberta.

Masliyah, J.H., Czarnecki, J. & Xu, Z. (2011). *Handbook on Theory and Practice of Bitumen Recovery from Athabasca Oil Sands, Volume I: Theoretical Basis.* Cochrane, AB: Kingsley Knowledge Publishing.

Mewis, J. & Wagner, N.J. (2012). *Colloidal Suspension Rheology*. New York, NY: Cambridge University Press.

Michaels, A.S. & Bolger, J.C. (1962). The Plastic Flow Behavior of Flocculated Kaolin Suspensions. *Industrial & Engineering Chemistry Fundamentals*, 1(3), 153-162.

Michaels, A.S. & Bolger, J.C. (1964). Particle Interactions in Aqueous Kaolinite Dispersions. *Industrial & Engineering Chemistry Fundamentals*, 3(1), 14-20.

Miller, J.D., Nalaskowski, J., Abdul, B. & Du, H. (2007). Surface Characteristics of Kaolinite and Other Selected Two Layer Silicate Minerals. *The Canadian Journal of Chemical Engineering*, 85(5), 617-624.

Rand, B. & Melton, I.E. (1977). Particle Interactions in Aqueous Kaolinite Suspensions I. Effect of pH and Electrolyte upon the Mode of Particle Interaction in Homoionic Sodium Kaolinite Suspensions. *Journal of Colloid and Interface Science*, 60(2), 308-320.

Salama, A.I.A. & Mikula, R.J. (1996). Particle and Suspension Characterization. In L.L. Schramm (Ed.) *Suspensions: Fundamentals and Applications in the Petroleum Industry* (pp. 107-176). Washington, DC: American Chemical Society.

Sanders, R.S., Schaan, J., Hughes, R., & Shook, C. (2004). Performance of Sand Slurry Pipelines in the Oil Sands Industry. *The Canadian Journal of Chemical Engineering*, 82(4), 850-857.

Sanders, R.S. & Gillies, R.G. (2012). Hydrotransport. In J. Czarnecki, et al. (Eds.) *Handbook on Theory and Practice of Bitumen Recovery from Athabasca Oil Sands, Volume II: Industrial Practice*. Cochrane, AB: Kingsley Knowledge Publishing.

Sanford, E.C. & Seyer, F.A. (1979). Processability of Athabasca Tar Sand Using a Batch Extraction Unit – Role of NaOH. *CIM Bulletin*, 72(803), 164-169.

Schaan, J. (2011). *Personal Communication*, February 3, 2011.

Schramm, L.L. (1996). *Suspensions: Fundamentals and Applications in the Petroleum Industry* (pp. 107-176). Washington, DC: American Chemical Society.

Shahmirzadi, A.A. (2012). The Effect of Fine Flocculating Particles and Fine Inerts on Carrier Fluid Viscosity (M.Sc. Thesis). University of Alberta, Edmonton, AB.

Shook, C.A. & Roco, M.C. (1991). *Slurry Flows: Principles and Practice*. Stoneham, MA: Butterworth-Heinemann.

Shook, C.A., Gillies, R.G., & Sanders, R.S. (2002). *Pipeline Hydrotransport with Applications in the Oil Sand Industry*. Saskatoon, SK: Saskatchewan Research Council.

Slatter, P.T. & Wasp, E.J. (2002). The Bingham Plastic rheological model: friend or foe? In N. Heywood (Ed.) *Proceedings of the 15th International Conference on Hydrotransport held in Banff, AB, 3-5 June 2002* (pp. 315-328). Bedfordshire, UK: BHR Group Limited.

Sumner, R.J., Munkler, J.J., Carriere, S.M., & Shook, C.A. (2000). Rheology of Kaolin Slurries Containing Large Silica Particles. *Journal of Hydrology and Hydromechanics,* 48(2), 110-124.

Sysmex Corporation. (2008). *Flow Particle Image Analyzer FPIA-3000 / FPIA-3000S Operator's Manual*. Kobe, Japan: Sysmex Corporation.

TA Instruments. (2004). *Rheology Advantage Data Analysis: Rheometrics Series Getting Started Guide Revision E*. Newcastle, DE: TA Instruments.

TA Instruments. (2006). *AR-G2 / AR 2000ex Rheometers Operator's Manual: Revision B*. Newcastle, DE: TA Instruments.

Thomas, A.D. (1999). The Influence of Coarse Particles on the Rheology of Fine Particle Slurries. *Proceedings of Rheology in the Mineral Industry II held in Kahuku, HI, 14-19 March 1999* (pp. 113-123). Mount Vernon, VA: United Engineering Foundation.

Thomas, D.G. (1965). Transport Characteristics of Suspension: VIII. A Note on the Viscosity of Newtonian Suspensions of Uniform Spherical Particles. *Journal of Colloid Science*, 20(3), 266-277.

Vaezi G., F., Sanders, R.S., Masliyah, J.H. (2011). Flocculation kinetics and aggregate structure of kaolinite mixtures in laminar tube flow. *Journal of Colloid and Interface Science*, 355(1), 96-105.

Wallace, D. (Ed.). (1988). *A Review of Analytical Methods for Bitumens and Heavy Oils*. Edmonton, AB: Alberta Oil Sands Technology and Research Authority.

Zbik, M.S., Smart, R.S.C., & Morris, G. (2008). Kaolinite flocculation structure. *Journal of Colloid and Interface Science*, 328(1), 73-80.

Zhou, Z., Kasongo, T., Xu, Z. & Masliyah, J.H. (2004). Assessment of bitumen recovery from the Athabasca oil sands using a laboratory Denver flotation cell. *The Canadian Journal of Chemical Engineering*, 82(4), 696-703.

Appendix 1: Dean Stark Analysis Results

The following formulas were used to calculate the RHS beads required for bitumen removal, FPIA sample dilution rates, values used in rheology calculations and the values presented in Chapter 3: Experimental Method.

Mass Fraction

$$w_i = \frac{m_i}{m_S + m_B + m_W}$$

Volume Fraction

$$C_i = \frac{m_i / \rho_i}{m_S / \rho_S + m_B / \rho_B + m_W / \rho_W}$$

Mixture Density

$$\rho = \Sigma C_i \rho_i$$

Component Densities

ρ_S	2650 kg/m^3
ρ_B	1000 kg/m^3
ρ_W	997.04 kg/m^3

Raw Samples

Sample Name	Sample Mass (g)	Mass of Solids (g)	Mass of Bitumen (g)	Mass of Water (g)	Closure (%)
S-M Raw	130.72	47.87	0.0147	79.43	97.4
S-MPSC Raw	115.65	41.37	0.0123	71.34	97.5
S-MFT Raw	110.12	34.11	4.50	71.01	99.5
S-TSRU Raw	89.40	15.93	5.28	67.94	99.7
S-TT Raw	86.96	18.52	0.05	68.12	99.7
SU-M Raw	147.72	73.87	0.0084	71.36	98.3
SU-NW Raw	103.03	11.52	0.0121	87.45	96.1
SU-RDW Raw	111.06	5.71	0.0121	101.33	96.4
SU-T Raw	138.63	62.24	0.0144	70.77	96.0
SU-TF Raw	181.22	94.89	0.0017	84.94	99.2
SU-TPSC Raw	165.65	95.21	0.0015	69.36	99.3
SU-TSF Raw	141.24	62.73	0.0025	77.33	99.2
SY-HT Raw	154.67	92.50	9.52	51.93	99.5
SY-M Raw	135.42	57.54	7.51	69.84	99.6
SY-T Raw	141.98	64.15	7.08	70.42	99.8
T-T Raw	95.67	15.27	0.35	79.69	99.6

Sieved Samples

Sample Name	Sample Mass (g)	Mass of Solids (g)	Mass of Bitumen (g)	Mass of Water (g)	Closure (%)
S-MFT Sieved	86.37	26.07	1.55	58.41	99.6
S-TSRU Sieved	71.38	4.18	0.9	66.07	99.7
S-TT Sieved	81.91	17.8	0.37	63.5	99.7
SY-HT Sieved	90.36	30.65	1.5	57.89	99.6
SY-M Sieved	117.52	24.06	1.07	91.98	99.7
SY-T Sieved	103.2	23.48	0.89	78.35	99.5
T-T Sieved	71.56	4.04	0.42	66.9	99.7

Note: Sieved T-T is also referred to as carrier fluid sample T-T(B)

Carrier Fluid Samples

Sample Name	Sample Mass (g)	Mass of Solids (g)	Mass of Bitumen (g)	Mass of Water (g)	Closure (%)
S-M1	107.35	15.31	0.0022	90.16	98.3
S-M2	120.79	18.12	0.0018	100.30	98.0
S-MFT1	118.31	36.19	0.0135	79.56	97.8
S-TSRU1	93.87	7.09	1.50	84.86	99.6
S-TSRU2	75.46	8.81	2.06	64.34	99.7
S-TT1	110.14	23.13	0.39	86.27	99.7
S-TT2	61.79	11.71	0.13	49.80	99.8
SU-M1	106.46	18.92	0.0011	86.73	99.2
SU-NW1	101.76	10.85	0.0122	88.12	97.3
SU-RDW1	99.05	5.08	0.0114	90.42	96.4
SU-T1	105.34	12.30	0.0086	90.17	97.3
SU-TF1	105.01	14.47	0.0006	89.46	99.0
SU-TPSC1	104.63	13.83	0.0012	90.37	99.6
SU-TSF1	108.71	18.35	0.0009	89.95	99.6
SY-HT1	119.64	43.77	0.0119	73.15	97.7
SY-M1	114.66	24.30	0.0056	89.14	98.9
T-T1	104.80	4.94	0.43	98.94	99.5
T-T2	85.06	9.39	0.62	74.80	99.7

Appendix 2: QuickBit Testing Results

The following formulas were used to calculate the RHS beads required for bitumen removal and solids content for FPIA dilution rates.

Mass Fraction

$$w_i = \frac{m_i}{m_S + m_B + m_W}$$

Volume Fraction

$$C_i = \frac{m_i / \rho_i}{m_S / \rho_S + m_B / \rho_B + m_W / \rho_W}$$

Mixture Density

$$\rho = \Sigma C_i \rho_i$$

Component Densities

ρ_S	2650 kg/m^3
ρ_B	1000 kg/m^3
ρ_W	997.04 kg/m^3

Sample: Sieved S-M Test 1

	Vial 1	**Vial 2**
Volume of Sample (mL)	5.0	5.0
Volume of Toluene (mL)	5.0	5.0
Mass of Filter Paper B (g)	1.46	1.46
Mass of Filter Paper B + Bitumen (g)	1.48	1.48
Mass of Bitumen (g)	0.02	0.02
Mass of Filter Paper S (g)	1.84	1.84
Mass of Filter Paper S + Solids (g)	2.63	2.63
Mass of Solids (g)	0.79	0.79

Average mass of bitumen = 0.02 g

Average mass of solids = 0.79 g

Total bitumen per vial = 0.05 g (0.05 mL)

Total solids per vial = 0.79 g (mL)

Total water per vial = 4.64 g (4.65 mL)

	Mass Basis	Volume Basis
% Solids	14.4	6.0
% Bitumen	0.9	1.0
% Water	84.7	93.0

Sample: Sieved S-M Test 2

	Vial 1	**Vial 2**
Volume of Sample (mL)	5.0	5.0
Volume of Toluene (mL)	5.0	5.0
Mass of Filter Paper B (g)	1.48	1.48
Mass of Filter Paper B + Bitumen (g)	1.52	1.52
Mass of Bitumen (g)	0.04	0.04
Mass of Filter Paper S (g)	1.86	1.86
Mass of Filter Paper S + Solids (g)	2.47	2.47
Mass of Solids (g)	0.61	0.61

Average mass of bitumen = 0.04 g

Average mass of solids = 0.61 g

Total bitumen per vial = 0.10 g (0.10 mL)

Total solids per vial = 0.61 g (0.23 mL)

Total water per vial = 4.66 g (4.67 mL)

	Mass Basis	Volume Basis
% Solids	11.4	4.6
% Bitumen	1.9	2.0
% Water	86.7	93.4

Sample: Sieved SU-M

	Vial 1	**Vial 2**
Volume of Sample (mL)	5.0	5.0
Volume of Toluene (mL)	5.0	5.0
Mass of Filter Paper B (g)	1.47	1.47
Mass of Filter Paper B + Bitumen (g)	1.49	1.49
Mass of Bitumen (g)	0.02	0.02
Mass of Filter Paper S (g)	1.65	1.64
Mass of Filter Paper S + Solids (g)	2.61	2.58
Mass of Solids (g)	0.96	0.94

Average mass of bitumen = 0.02 g

Average mass of solids = 0.95 g

Total bitumen per vial = 0.05 g (0.05 mL)

Total solids per vial = 0.95 g (0.36 mL)

Total water per vial = 4.58 g (4.59 mL)

	Mass Basis	Volume Basis
% Solids	17.0	7.2
% Bitumen	0.9	1.0
% Water	82.1	91.8

Sample: Sieved SU-NW

	Vial 1	**Vial 2**
Volume of Sample (mL)	5.0	5.0
Volume of Toluene (mL)	5.0	5.0
Mass of Filter Paper B (g)	1.48	1.43
Mass of Filter Paper B + Bitumen (g)	1.50	1.46
Mass of Bitumen (g)	0.02	0.03
Mass of Filter Paper S (g)	1.66	1.65
Mass of Filter Paper S + Solids (g)	2.35	2.30
Mass of Solids (g)	0.69	0.65

Average mass of bitumen = 0.025 g

Average mass of solids = 0.67 g

Total bitumen per vial = 0.06 g (0.06 mL)

Total solids per vial = 0.67 g (0.25 mL)

Total water per vial = 4.67 g (4.69 mL)

	Mass Basis	Volume Basis
% Solids	12.4	5.1
% Bitumen	1.2	1.3
% Water	86.4	93.6

Sample: Sieved SU-RDW

	Vial 1	**Vial 2**
Volume of Sample (mL)	5.0	5.0
Volume of Toluene (mL)	5.0	5.0
Mass of Filter Paper B (g)	1.40	1.50
Mass of Filter Paper B + Bitumen (g)	1.41	1.51
Mass of Bitumen (g)	0.01	0.01
Mass of Filter Paper S (g)	1.65	1.67
Mass of Filter Paper S + Solids (g)	2.02	2.02
Mass of Solids (g)	0.37	0.35

Average mass of bitumen = 0.01 g

Average mass of solids = 0.36 g

Total bitumen per vial = 0.03 g (0.03 mL)

Total solids per vial = 0.36 g (0.14 mL)

Total water per vial = 4.70 g (4.71 mL)

	Mass Basis	Volume Basis
% Solids	6.9	2.7
% Bitumen	0.5	0.5
% Water	92.6	96.8

Sample: Sieved SU-T

	Vial 1	**Vial 2**
Volume of Sample (mL)	5.0	5.0
Volume of Toluene (mL)	5.0	5.0
Mass of Filter Paper B (g)	1.45	1.53
Mass of Filter Paper B + Bitumen (g)	1.45	1.54
Mass of Bitumen (g)	0.00	0.01
Mass of Filter Paper S (g)	1.65	1.65
Mass of Filter Paper S + Solids (g)	2.36	2.37
Mass of Solids (g)	0.71	0.72

Average mass of bitumen = 0.005 g

Average mass of solids = 0.715 g

Total bitumen per vial = 0.01 g (0.01 mL)

Total solids per vial = 0.72 g (0.27 mL)

Total water per vial = 4.70 g (4.72 mL)

	Mass Basis	Volume Basis
% Solids	13.2	5.4
% Bitumen	0.2	0.3
% Water	86.6	94.3

Sample: Sieved SU-TF

	Vial 1	**Vial 2**
Volume of Sample (mL)	5.0	5.0
Volume of Toluene (mL)	5.0	5.0
Mass of Filter Paper B (g)	1.46	1.39
Mass of Filter Paper B + Bitumen (g)	1.47	1.40
Mass of Bitumen (g)	0.01	0.01
Mass of Filter Paper S (g)	1.81	1.81
Mass of Filter Paper S + Solids (g)	2.59	2.51
Mass of Solids (g)	0.78	0.70

Average mass of bitumen = 0.01 g

Average mass of solids = 0.74 g

Total bitumen per vial = 0.03 g (0.03 mL)

Total solids per vial = 0.74 g (0.28 mL)

Total water per vial = 4.68 g (4.70 mL)

	Mass Basis	Volume Basis
% Solids	13.6	5.6
% Bitumen	0.5	0.5
% Water	85.9	93.9

Sample: Sieved SU-TPSC

	Vial 1	**Vial 2**
Volume of Sample (mL)	5.0	5.0
Volume of Toluene (mL)	5.0	5.0
Mass of Filter Paper B (g)	1.36	1.44
Mass of Filter Paper B + Bitumen (g)	1.37	1.45
Mass of Bitumen (g)	0.01	0.01
Mass of Filter Paper S (g)	1.66	1.63
Mass of Filter Paper S + Solids (g)	2.37	2.30
Mass of Solids (g)	0.71	0.67

Average mass of bitumen = 0.01 g

Average mass of solids = 0.69 g

Total bitumen per vial = 0.03 g (0.03 mL)

Total solids per vial = 0.69 g (0.26 mL)

Total water per vial = 4.70 g (4.71 mL)

	Mass Basis	Volume Basis
% Solids	12.7	5.2
% Bitumen	0.5	0.5
% Water	86.8	94.3

Sample: Sieved SU-TSF

	Vial 1	**Vial 2**
Volume of Sample (mL)	5.0	5.0
Volume of Toluene (mL)	5.0	5.0
Mass of Filter Paper B (g)	1.48	1.46
Mass of Filter Paper B + Bitumen (g)	1.50	1.47
Mass of Bitumen (g)	0.02	0.01
Mass of Filter Paper S (g)	1.75	1.65
Mass of Filter Paper S + Solids (g)	2.66	2.57
Mass of Solids (g)	0.91	0.92

Average mass of bitumen = 0.015 g

Average mass of solids = 0.915 g

Total bitumen per vial = 0.04 g (0.04 mL)

Total solids per vial = 0.92 g (0.34 mL)

Total water per vial = 4.60 g (4.62 mL)

	Mass Basis	Volume Basis
% Solids	16.5	6.9
% Bitumen	0.7	0.8
% Water	82.8	92.3

Appendix 3: Water Ion Chromatography Results

Sample	pH	Conductivity (MS/cm)	Na^+ (mg/L)	K^+ (mg/L)	Mg^{2+} (mg/L)
S-M Test 1	8.53	1.51	309.3	15.15	10.40
S-M Test 2	8.82	1.58	315.0	15.861	11.80
S-MFT	8.81	1.54	384.9	14.43	12.71
S-TSRU	9.14	1.17	292.0	13.68	11.01
S-TT	8.99	1.57	377.4	18.63	5.80
SU-M	9.08	3.02	835.3	12.62	19.16
SU-NW	8.73	3.09	872.0	11.52	5.19
SU-RDW	8.76	3.12	836.6	11.49	5.17
SU-T	9.30	3.37	959.0	11.60	5.12
SU-TF	9.02	3.01	769.6	12.42	6.16
SU-TPSC	9.05	3.00	774.0	11.86	4.83
SU-TSF	9.09	2.76	788.7	12.81	4.88
SY-HT	8.63	3.35	849.5	31.80	5.12
SY-M	8.90	3.39	3951	28.25	35.66
SY-T	8.58	3.14	3795	26.99	31.71
T-T	8.58	0.64	536.3	12.52	7.86
T-T(B)	8.53	0.57	513.5	11.72	7.26

Sample	Ca^{2+} (mg/L)	Fe^{3+} (mg/L)	Al^{3+} (mg/L)	Cl^{-} (mg/L)	NO_3^{-} (mg/L)
S-M Test 1	21.03	BDL	BDL	167.72	BDL
S-M Test 2	22.60	BDL	BDL	168.50	BDL
S-MFT	18.95	BDL	BDL	273.42	0.24
S-TSRU	9.50	BDL	BDL	159.66	BDL
S-TT	8.40	BDL	BDL	723.41	BDL
SU-M	7.34	BDL	BDL	768.86	BDL
SU-NW	5.68	BDL	BDL	792.57	BDL
SU-RDW	6.31	BDL	BDL	775.12	BDL
SU-T	6.46	BDL	BDL	807.49	BDL
SU-TF	6.04	BDL	BDL	723.18	BDL
SU-TPSC	7.47	0.49	2.91	707.82	BDL
SU-TSF	7.55	BDL	BDL	730.69	BDL
SY-HT	73.17	BDL	BDL	495.69	BDL
SY-M	42.71	BDL	BDL	412.20	BDL
SY-T	35.49	BDL	BDL	401.40	BDL
T-T	12.55	BDL	BDL	53.96	BDL
T-T(B)	11.03	BDL	BDL	53.56	BDL

Note: BDL = below detectable limit

Sample	SO_4^- (mg/L)	HCO_3^- Test 1 (mg/L)	HCO_3^- Test 2 (mg/L)	CO_3^{2-} (mg/L)	Ionic Strength (mol/L)
S-M Test 1	61.72	416.8	–	24	0.017
S-M Test 2	63.48	416.8	–	36	0.017
S-MFT	20.99	500.1	502.6	36	0.020
S-TSRU	52.63	335.1	330.8	36	0.015
S-TT	71.35	341.2	345.0	36	0.025
SU-M	122.68	686.0	693.9	72	0.042
SU-NW	140.52	666.7	657.1	60	0.041
SU-RDW	129.70	680.1	676.8	48	0.040
SU-T	129.60	739.8	734.9	108	0.045
SU-TF	111.10	658.2	659.4	72	0.038
SU-TPSC	109.60	644.4	641.4	60	0.038
SU-TSF	117.90	671.1	677.9	72	0.039
SY-HT	526.30	311.7	306.0	24	0.044
SY-M	279.90	389.2	388.9	48	0.108
SY-T	279.60	329.6	329.6	24	0.102
T-T	29.70	143.8	147.4	0	0.016
T-T(B)	29.98	126.2	133.2	0	0.015

Note: Ionic strength calculated using Equation 3.1

Appendix 4: AR-G2 Rheometer Calibration Data

Calibration Test 1

Calibration Oil	N100
Standard Viscosity (Pas)	0.2022
Standard Density (kg/m^3)	869.0
ω_{crit} (rad/s)	2085
Temperature (°C)	25
Measured Viscosity (Pas)	0.2033
% Difference	0.53

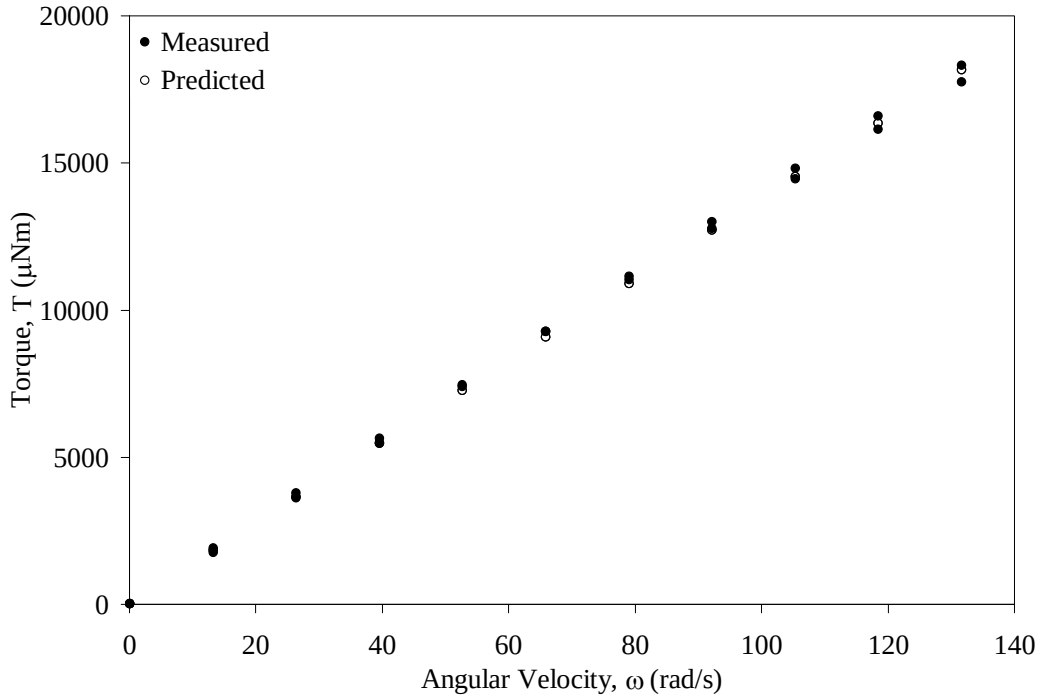

Spindle Speed, ω (rad/s)	**Measured Torque, $T_{meas.}$ (μNm)**	**Predicted Torque, $T_{calc.}$ (μNm)**
0.100005	13.0912	13.80
13.252600	1767.35	1829.07
26.405300	3605.95	3644.35
39.558000	5490.73	5459.64
52.710600	7389.46	7274.91
65.863100	9278.29	9090.16
79.015800	11149.6	10905.45
92.168400	12995.8	12720.72
105.321000	14809.8	14535.99
118.474000	16591.7	16351.31
131.626000	18315.6	18166.50
131.627000	17747.3	18166.64
118.473000	16131.7	16351.17
105.321000	14462.3	14535.99
92.168300	12763.5	12720.70
79.015700	11031.2	10905.43
65.863100	9265.6	9090.16
52.710500	7463.31	7274.89
39.557900	5636.79	5459.62
26.405300	3779.24	3644.35
13.252600	1904.08	1829.07
0.100001	14.4303	13.80

Calibration Test 2

Calibration Oil	N1000
Standard Viscosity (Pas)	2.018
Standard Density (kg/m^3)	846.3
ω_{crit} (rad/s)	21363
Temperature (°C)	25
Measured Viscosity (Pas)	1.939
% Difference	3.92

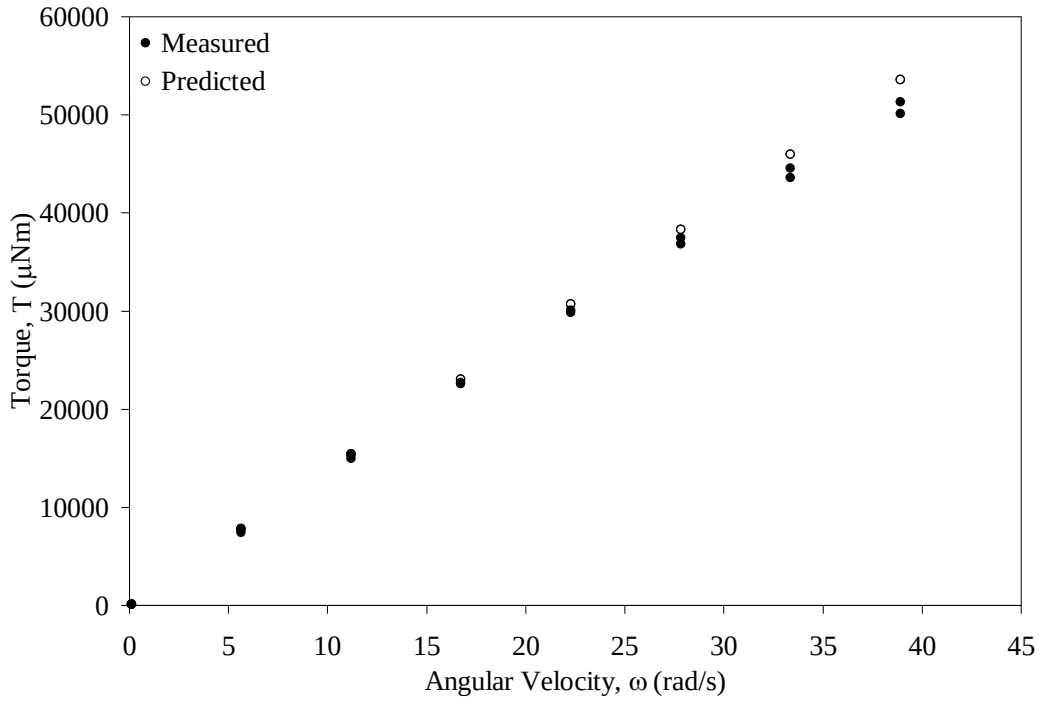

Spindle Speed, ω (rad/s)	**Measured Torque, $T_{meas.}$ (μNm)**	**Predicted Torque, $T_{calc.}$ (μNm)**
0.099999	128.315	137.74
5.644430	7463.78	7774.81
11.188900	15005.9	15411.93
16.733300	22569.1	23048.95
22.277800	30105.3	30686.11
27.822200	37448.9	38323.14
33.366600	44543.2	45960.16
38.911200	51317	53597.46
38.911100	50146.3	53597.32
33.366700	43596.4	45960.30
27.822200	36817.3	38323.14
22.277800	29843.5	30686.11
16.733400	22708	23049.09
11.188900	15338.1	15411.93
5.644450	7806.62	7774.84
0.099994	139.694	137.74

Calibration Test 3

Calibration Oil	S6
Standard Viscosity (Pas)	0.007852
Standard Density (kg/m^3)	877.7
ω_{crit} (rad/s)	80.1
Temperature (°C)	25
Measured Viscosity (Pas)	0.008681
% Difference	10.55

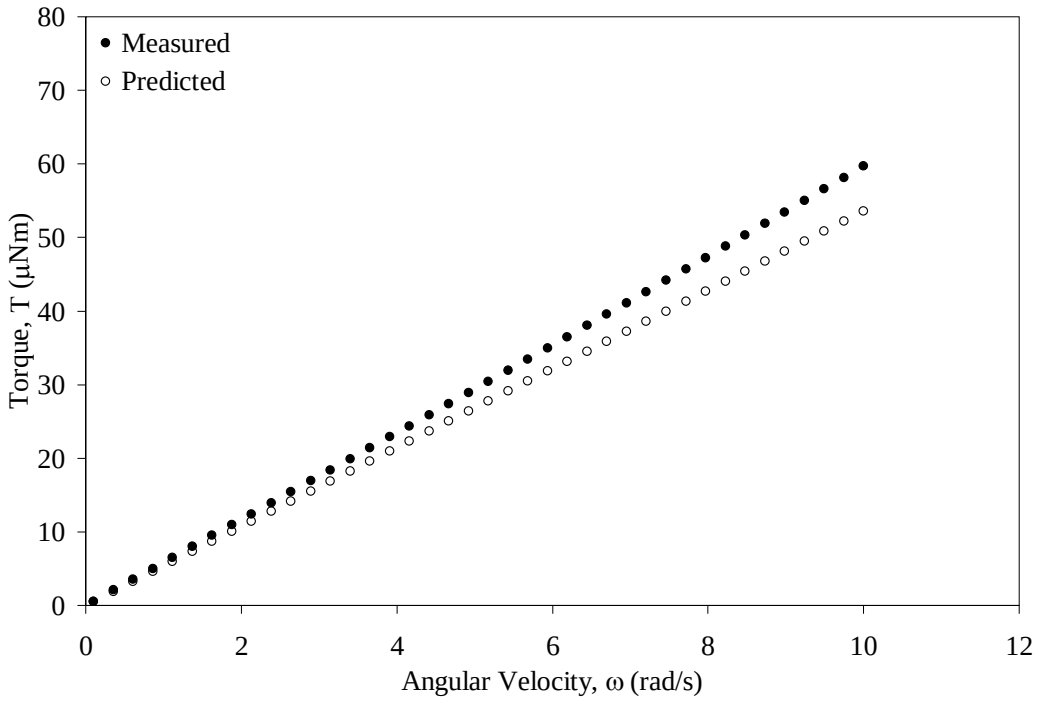

Spindle Speed, ω (rad/s)	Measured Torque, $T_{meas.}$ (μNm)	Predicted Torque, $T_{calc.}$ (μNm)
0.099998	0.528144	0.54
0.353843	2.09023	1.90
0.607698	3.54073	3.26
0.861540	4.98663	4.62
1.115380	6.52466	5.98
1.369240	8.00897	7.34
1.623070	9.51097	8.70
1.876940	10.981	10.06
2.130760	12.4373	11.42
2.384620	13.9357	12.78
2.638460	15.4268	14.14
2.892310	16.9334	15.50
3.146140	18.3891	16.86
3.400020	19.9088	18.22
3.653860	21.4032	19.58
3.907670	22.9	20.94
4.161540	24.398	22.30
4.415390	25.9056	23.66
4.669240	27.4095	25.03
4.923080	28.9207	26.39
5.176930	30.4369	27.75
5.430770	31.9614	29.11
5.684620	33.4722	30.47
5.938460	34.9973	31.83
6.192310	36.5077	33.19
6.446150	38.0387	34.55
6.699990	39.5774	35.91

Test 3 (Continued)

Spindle Speed, ω (rad/s)	**Measured Torque, $T_{meas.}$ (μNm)**	**Predicted Torque, $T_{calc.}$ (μNm)**
6.953850	41.0998	37.27
7.207690	42.6358	38.63
7.461530	44.1804	39.99
7.715390	45.7175	41.35
7.969230	47.2536	42.71
8.223070	48.802	44.07
8.476920	50.3559	45.43
8.730770	51.9011	46.79
8.984620	53.4681	48.15
9.238460	55.0392	49.51
9.492300	56.5834	50.87
9.746160	58.1447	52.24
10	59.7161	53.60

Appendix 5: Rheological Measurements of Carrier Fluid Water

S-M Water

$\mu = 1.12$ mPas $\rho = 997.0$ kg/m^3

$\omega_{crit} = 10.0$ rad/s

Run 1		Run 2	
Angular velocity, ω (rad/s)	**Torque, T (μNm)**	**Angular velocity, ω (rad/s)**	**Torque, T (μNm)**
0.099987	0.0422102	0.100014	0.0896588
0.884267	0.593681	0.884163	0.606177
1.668450	1.21362	1.668450	1.18132
2.452610	1.76489	2.452610	1.76362
3.236870	2.32664	3.236840	2.29871
4.021060	2.98322	4.021050	2.96218
4.805290	3.61311	4.805230	3.57511
5.589430	4.30015	5.589480	4.25951
6.373670	4.95478	6.373680	4.90811
7.157910	5.62526	7.157880	5.58293
7.157890	5.59063	7.157860	5.58383
6.373690	4.92577	6.373670	4.9027
5.589450	4.2605	5.589470	4.24894
4.805250	3.62456	4.805290	3.60565
4.021040	2.97284	4.021050	2.96437
3.236900	2.34793	3.236880	2.31262
2.452620	1.77837	2.452650	1.76517
1.668390	1.20072	1.668440	1.17801
0.884161	0.611831	0.884229	0.601015
–	–	0.100019	0.0851109

T-T Water (continued)

Run 3	
Angular velocity, ω (rad/s)	**Torque, T (μNm)**
0.099997	0.208132
0.884251	0.590251
1.668420	1.16704
2.452660	1.76299
3.236790	2.37602
4.021060	2.96365
4.805220	3.62627
5.589520	4.22935
6.373680	4.93371
7.157890	5.60445
7.157940	5.58792
6.373660	4.92261
5.589430	4.25842
4.805230	3.60758
4.021040	2.96507
3.236860	2.3794
2.452600	1.77858
1.668420	1.16109
0.884195	0.616942
0.09999	0.284841

S-MFT Water

$\mu = 1.17$ mPas $\rho = 997.0$ kg/m^3

$\omega_{crit} = 10.5$ rad/s

Run 1		Run 2	
Angular velocity, ω (rad/s)	**Torque, T (μNm)**	**Angular velocity, ω (rad/s)**	**Torque, T (μNm)**
0.099994	0.149228	0.099991	0.0377012
0.884226	0.82688	0.884202	0.603671
1.668410	1.4179	1.668410	1.1649
2.452640	2.10389	2.452630	1.74533
3.236860	2.84701	3.236840	2.36068
4.021060	3.45006	4.021060	2.98127
4.805260	4.12612	4.805260	3.62135
5.589460	4.77276	5.589470	4.2758
6.373690	5.44235	6.373690	4.95441
7.157900	6.18438	6.373690	4.99927
7.157890	6.07482	5.589480	4.31925
6.373680	5.32372	4.805260	3.65319
5.589470	4.605	4.021050	3.0043
4.805250	3.89817	3.236850	2.36642
4.021060	3.21188	2.452640	1.76404
3.236850	2.53882	1.668430	1.17947
2.452640	1.89858	0.884214	0.609597
1.668430	1.27534	0.100014	0.0930149
0.884219	0.667502	–	–
0.0999958	0.106698	–	–

S-TSRU Water

$\mu = 1.14$ mPas $\rho = 997.0$ kg/m^3

$\omega_{crit} = 10.2$ rad/s

Run 1		Run 2	
Angular velocity, ω (rad/s)	**Torque, T (μNm)**	**Angular velocity, ω (rad/s)**	**Torque, T (μNm)**
6.373700	5.02111	0.100001	0.0814614
5.589460	4.34507	0.884212	0.608127
4.805240	3.68648	1.668420	1.19172
4.021050	3.04259	2.452640	1.78964
3.236880	2.41159	3.236850	2.40557
2.452640	1.81881	4.021060	3.03824
1.668420	1.20967	4.805270	3.68498
6.373680	5.04077	5.589470	4.35883
5.589470	4.36246	6.373680	5.03759
4.805250	3.69927	7.157890	5.73192
4.021050	3.04213	7.157900	5.76412
3.236840	2.44467	6.373690	5.05724
2.452620	1.82731	5.589480	4.37211
1.668410	1.21748	4.805260	3.69944
0.884187	0.646626	4.021060	3.05096
–	–	3.236850	2.41787
–	–	2.452630	1.80022
–	–	1.668420	1.19669
–	–	0.884211	0.622429
–	–	0.100003	0.0635173

S-TT Water

$\mu = 1.13$ mPa $\rho = 997.0$ kg/m^3

$\omega_{crit} = 10.1$ rad/s

Run 1		Run 2	
Angular velocity, ω (rad/s)	**Torque, T (μNm)**	**Angular velocity, ω (rad/s)**	**Torque, T (μNm)**
7.157890	5.78326	0.884248	0.58678
6.373690	5.08177	1.668440	1.16163
5.589460	4.39462	2.452670	1.74205
4.805250	3.72362	3.236800	2.38569
4.021050	3.07002	4.021050	2.96009
3.236880	2.44912	4.805220	3.61844
2.452630	1.82891	5.589490	4.23292
1.668390	1.21285	6.373680	4.91844
0.884184	0.640157	6.373690	4.93615
0.100006	0.166052	5.589480	4.24522
7.157910	5.78977	4.805270	3.58488
6.373690	5.10334	4.021060	2.96927
5.589480	4.40099	3.236780	2.3661
4.805270	3.72652	2.452630	1.7164
4.021050	3.07977	1.668400	1.1645
3.236830	2.47312	0.884175	0.599078
2.452620	1.81543	0.0999959	0.00066388
1.668430	1.18409	–	–
0.884214	0.629766	–	–

SU-M Water

$\mu = 1.132$ mPas $\rho = 997.0$ kg/m^3

$\omega_{crit} = 10.2$ rad/s

Run 1		**Run 2**	
Angular velocity, ω (rad/s)	**Torque, T (μNm)**	**Angular velocity, ω (rad/s)**	**Torque, T (μNm)**
0.100008	0.0583263	0.100013	0.179612
0.884242	0.60066	0.884227	0.598656
1.668420	1.20473	1.668450	1.17346
2.452610	1.76588	2.452630	1.79267
3.236870	2.34299	3.236820	2.36688
4.021050	2.9951	4.021050	3.01329
4.805280	3.62553	4.805250	3.65426
5.589460	4.30871	5.589480	4.33754
6.373680	4.98526	6.373680	5.0084
7.157890	5.67213	7.157900	5.71564
7.157890	5.69742	7.157910	5.72167
6.373700	4.99448	6.373700	5.01407
5.589470	4.31929	5.589490	4.33014
4.805270	3.64451	4.805310	3.65726
4.021060	3.00059	4.021050	3.01633
3.236880	2.39757	3.236820	2.36423
2.452620	1.78605	2.452640	1.75939
1.668400	1.16399	1.668440	1.18575
0.884168	0.60841	0.884249	0.608256
0.1	0.0897817	0.0999896	0.0538589

SU-NW Water

$\mu = 1.13$ mPas $\rho = 997.0$ kg/m^3

$\omega_{crit} = 10.2$ rad/s

Run 1		Run 2	
Angular velocity, ω (rad/s)	**Torque, T (μNm)**	**Angular velocity, ω (rad/s)**	**Torque, T (μNm)**
0.100010	0.113588	0.099995	0.15268
0.884201	0.623737	0.884196	0.598697
1.668430	1.17177	1.668420	1.14805
2.452640	1.79334	2.452630	1.76153
3.236830	2.41626	3.236810	2.35439
4.021040	3.03637	4.021050	2.97156
4.805260	3.69192	4.805250	3.61349
5.589480	4.34559	5.589480	4.27935
6.373680	5.04274	6.373690	4.95569
7.157900	5.74789	7.157890	5.64443
7.157910	5.7702	7.157870	5.64664
6.373680	5.06523	6.373690	4.95361
5.589490	4.36389	5.589490	4.28879
4.805270	3.69169	4.805300	3.62868
4.021060	3.04981	4.021060	2.9864
3.236810	2.41416	3.236850	2.35038
2.452620	1.77977	2.452630	1.76627
1.668430	1.18433	1.668430	1.18454
0.884224	0.62016	0.884218	0.610665
–	–	0.100038	0.0761934

SU-RDW Water

$\mu = 1.16$ mPas $\rho = 997.0$ kg/m^3

$\omega_{crit} = 10.4$ rad/s

Run 1		Run 2	
Angular velocity, ω (rad/s)	**Torque, T (μNm)**	**Angular velocity, ω (rad/s)**	**Torque, T (μNm)**
0.884175	0.680912	0.100011	0.130747
1.668390	1.30545	0.884196	0.599938
2.452660	1.92612	1.668430	1.16105
3.236840	2.66342	2.452630	1.76579
4.021060	3.29921	3.236830	2.36816
4.805250	4.02967	4.021050	2.99309
5.589480	4.717	4.805250	3.63658
6.373680	5.48305	5.589470	4.29192
6.373680	5.4716	6.373680	4.97036
5.589480	4.76846	7.157900	5.66385
4.805250	4.03339	7.157880	5.66786
4.021050	3.31905	6.373670	4.96471
3.236920	2.58474	5.589480	4.2942
2.452660	1.98258	4.805280	3.63134
1.668460	1.30319	4.021060	2.98905
0.884247	0.684948	3.236830	2.35078
0.100003	0.116219	2.452650	1.74637
–	–	1.668440	1.16367
–	–	0.884233	0.601617
–	–	0.0999953	0.0636059

SU-RDW Water (continued)

Run 3	
Angular velocity, ω (rad/s)	**Torque, T (μNm)**
0.100001	0.122504
0.884219	0.600168
1.668410	1.16578
2.452640	1.77068
3.236830	2.36724
4.021050	2.9961
4.805230	3.63971
5.589480	4.30189
6.373670	4.97392
7.157900	5.66687
7.157880	5.66246
6.373670	4.96713
5.589470	4.29519
4.805270	3.63784
4.021060	2.99226
3.236840	2.35753
2.452640	1.75243
1.668420	1.17072
0.884224	0.603221
0.100003	0.0722814

SU-T Water

$\mu = 1.20$ mPas $\rho = 997.0$ kg/m^3

$\omega_{crit} = 10.8$ rad/s

Run 1		Run 2	
Angular velocity, ω (rad/s)	**Torque, T (μNm)**	**Angular velocity, ω (rad/s)**	**Torque, T (μNm)**
0.884269	0.639284	0.100015	0.155512
1.668470	1.26992	0.884157	0.673826
2.452620	1.92052	1.668460	1.29947
3.236830	2.50414	2.452600	1.94077
4.021050	3.22377	3.236840	2.52162
4.805240	3.89981	4.021050	3.25215
5.589510	4.63062	4.805250	3.93174
5.589510	4.60732	5.589490	4.66167
4.805300	3.90911	6.373680	5.3862
4.021060	3.22056	7.157860	6.14222
3.236810	2.49963	7.157920	6.16212
2.452680	1.88122	6.373690	5.40766
1.668460	1.2865	5.589470	4.66648
0.884231	0.656754	4.805280	3.9753
0.10004	0.130615	4.021050	3.26577
–	–	3.236910	2.55459
–	–	2.452630	1.9553
–	–	1.668470	1.28386
–	–	0.884248	0.670113
–	–	0.100001	0.0987491

SU-TF Water

$\mu = 1.14$ mPas $\rho = 997.0$ kg/m^3

$\omega_{crit} = 10.3$ rad/s

Run 1		Run 2	
Angular velocity, ω (rad/s)	**Torque, T (μNm)**	**Angular velocity, ω (rad/s)**	**Torque, T (μNm)**
0.099994	0.0886508	0.099997	0.112798
0.884233	0.604851	0.884176	0.616484
1.668430	1.20093	1.668420	1.16162
2.452620	1.78569	2.452640	1.78384
3.236850	2.36754	3.236820	2.41808
4.021060	3.01961	4.021050	3.03449
4.805270	3.66122	4.805250	3.69657
5.589460	4.34555	5.589510	4.34709
6.373690	5.01436	6.373690	5.05206
7.157910	5.71418	7.157900	5.75577
7.157870	5.75981	7.157920	5.76037
6.373680	5.04392	6.373670	5.05354
5.589490	4.35197	5.589500	4.35125
4.805290	3.67572	4.805280	3.68118
4.021070	3.03534	4.021050	3.03791
3.236820	2.3989	3.236820	2.39269
2.452640	1.76627	2.452640	1.77509
1.668430	1.17313	1.668430	1.18506
0.884233	0.607951	0.884233	0.612716
–	–	0.100004	0.0353388

SU-TPSC Water

$\mu = 1.14$ mPas $\rho = 997.0$ kg/m^3

$\omega_{crit} = 10.3$ rad/s

Run 1		Run 2	
Angular velocity, ω (rad/s)	**Torque, T (μNm)**	**Angular velocity, ω (rad/s)**	**Torque, T (μNm)**
0.099982	0.210727	0.100003	0.0722816
0.884310	0.631885	0.884232	0.599378
1.668470	1.25832	1.668440	1.18125
2.452650	1.9357	2.452620	1.75813
3.236740	2.56483	3.236870	2.34071
4.021050	3.1792	4.021050	2.97565
4.805230	3.86253	4.805290	3.60546
5.589520	4.54618	5.589470	4.2752
6.373690	5.2643	6.373690	4.93982
7.157810	6.0235	7.157890	5.61841
7.157850	5.98825	7.157900	5.61731
6.373700	5.24884	6.373680	4.938
5.589410	4.54862	5.589460	4.25583
4.805200	3.85781	4.805240	3.61869
4.021070	3.16437	4.021040	2.97702
3.236780	2.56333	3.236840	2.34026
2.452590	1.83237	2.452640	1.74449
1.668370	1.25352	1.668440	1.16562
0.884116	0.663423	0.884228	0.601526
0.0999914	0.223991	0.100006	0.0294307

SU-TPSC Water (continued)

Run 3	
Angular velocity, ω (rad/s)	**Torque, T (μNm)**
0.100005	0.034332
0.884196	0.608785
1.668400	1.1592
2.452630	1.74372
3.236850	2.37434
4.021050	2.98061
4.805270	3.62845
5.589480	4.26732
6.373690	4.9378
7.157900	5.63759
7.157890	5.62927
6.373680	4.94204
5.589490	4.27423
4.805260	3.62682
4.021050	2.98348
3.236870	2.35396
2.452640	1.75758
1.668410	1.18146
0.884204	0.608252
0.100012	0.137282

SU-TSF Water

μ = 1.16 mPas ρ = 997.0 kg/m^3

ω_{crit} = 10.4 rad/s

Run 1		**Run 2**	
Angular velocity, ω (rad/s)	**Torque, T (μNm)**	**Angular velocity, ω (rad/s)**	**Torque, T (μNm)**
0.100004	0.0657509	0.099993	0.112691
0.884189	0.627305	0.884199	0.618815
1.668430	1.20417	1.668420	1.21132
2.452630	1.80457	2.452620	1.83027
3.236850	2.43424	3.236830	2.4654
4.021050	3.07076	4.021050	3.1062
4.805270	3.72929	4.805250	3.77025
5.589480	4.39692	5.589490	4.43842
6.373680	5.08962	6.373690	5.14209
7.157910	5.80675	7.157900	5.86842
7.157910	5.83762	7.157890	5.86926
6.373690	5.12298	6.373680	5.15045
5.589470	4.42515	5.589470	4.45517
4.805270	3.75041	4.805250	3.77296
4.021050	3.09076	4.021050	3.10739
3.236840	2.45087	3.236850	2.45828
2.452630	1.81441	2.452610	1.83494
1.668420	1.20405	1.668420	1.22719
0.884235	0.628566	0.884198	0.639173
0.0999808	0.0437482	0.100021	0.119594

SY-HT

μ = 1.17 mPas ρ = 997.0 kg/m^3

ω_{crit} = 10.5 rad/s

Run 1		**Run 2**	
Angular velocity, ω (rad/s)	**Torque, T (μNm)**	**Angular velocity, ω (rad/s)**	**Torque, T (μNm)**
0.099987	0.0981777	0.100004	0.17939
0.884200	0.619301	0.884214	0.628486
1.668410	1.19095	1.668440	1.22156
2.452630	1.80165	2.452660	1.85256
3.236840	2.41508	3.236840	2.45552
4.021060	3.05209	4.021040	3.1267
4.805260	3.70774	4.805260	3.79082
5.589480	4.38688	5.589480	4.49132
6.373700	5.08166	6.373680	5.19204
7.157880	5.79986	7.157880	5.9294
7.157900	5.83908	7.157900	5.97794
6.373680	5.11348	6.373690	5.2365
5.589470	4.41372	5.589480	4.52455
4.805270	3.73487	4.805280	3.83605
4.021050	3.07638	4.021040	3.1558
3.236810	2.42966	3.236810	2.51466
2.452630	1.80861	2.452620	1.84725
1.668430	1.20596	1.668410	1.20662
0.884214	0.627161	0.884223	0.638604
0.0999859	0.0712068	0.0999909	-0.023706

SY-M

μ = 1.15 mPas ρ = 997.0 kg/m^3

ω_{crit} = 10.3 rad/s

Run 1		**Run 2**	
Angular velocity, ω (rad/s)	**Torque, T (μNm)**	**Angular velocity, ω (rad/s)**	**Torque, T (μNm)**
0.099995	0.0025486	0.884192	0.631368
0.884227	0.629477	1.668400	1.23151
1.668400	1.2563	2.452670	1.83314
2.452600	1.81702	3.236820	2.54153
3.236900	2.43096	4.021040	3.13047
4.021070	3.09252	4.805260	3.83941
4.805280	3.74302	5.589460	4.49513
5.589430	4.36515	6.373690	5.21953
6.373680	5.04504	6.373680	5.23828
6.373650	4.98381	5.589470	4.52319
5.589490	4.30194	4.805220	3.8208
4.805280	3.64409	4.021030	3.1487
4.021070	3.00188	3.236800	2.55073
3.236830	2.36357	2.452600	1.85105
2.452660	1.75617	1.668380	1.23934
1.668430	1.1766	0.884134	0.653932
0.884255	0.606811	–	–
0.100009	0.0581834	–	–

SY-T

μ = 1.14 mPas ρ = 997.0 kg/m^3

ω_{crit} = 10.3 rad/s

Run 1		**Run 2**	
Angular velocity, ω (rad/s)	**Torque, T (μNm)**	**Angular velocity, ω (rad/s)**	**Torque, T (μNm)**
0.099999	0.0807468	0.100007	0.0955588
0.884198	0.601422	0.884205	0.61715
1.668420	1.16868	1.668420	1.21622
2.452630	1.76317	2.452620	1.81293
3.236840	2.37486	3.236840	2.40799
4.021060	2.99944	4.021060	3.06258
4.805270	3.64447	4.805270	3.70723
5.589480	4.30241	5.589480	4.39811
6.373680	4.97821	6.373680	5.08009
7.157890	5.68816	7.157890	5.79217
7.157890	5.72252	7.157890	5.80764
6.373680	5.01427	6.373690	5.09898
5.589470	4.33884	5.589460	4.40903
4.805250	3.67693	4.805270	3.72833
4.021050	3.02108	4.021050	3.06807
3.236850	2.3848	3.236840	2.4308
2.452640	1.77278	2.452620	1.81452
1.668420	1.17816	1.668410	1.22243
0.884217	0.612765	0.884203	0.629271
0.0999902	0.0601874	0.100023	0.145614

T-T Water

μ = 1.15 mPas ρ = 997.0 kg/m^3

ω_{crit} = 10.30 rad/s

Run 1		Run 2	
Angular velocity, ω (rad/s)	**Torque, T (μNm)**	**Angular velocity, ω (rad/s)**	**Torque, T (μNm)**
7.157900	5.76378	0.099998	0.0817231
6.373690	5.06642	0.884219	0.655104
5.589480	4.39127	1.668430	1.28932
4.805280	3.71969	2.452630	1.97691
4.021060	3.07527	3.236820	2.61858
3.236830	2.42954	4.021050	3.21946
2.452630	1.81731	4.805260	3.82554
1.668430	1.22549	5.589470	4.49204
0.884208	0.644558	6.373690	5.1409
0.099995	0.121289	7.157880	5.83579
7.157870	5.78804	7.157890	5.78846
6.373690	5.08479	6.373680	5.0731
5.589470	4.40178	5.589480	4.38791
4.805270	3.73182	4.805260	3.71231
4.021050	3.08063	4.021050	3.05263
3.236850	2.44426	3.236840	2.4077
2.452630	1.82937	2.452640	1.79305
1.668400	1.22246	1.668430	1.19936
0.884174	0.644681	0.884200	0.619941
0.100007	0.131006	0.100011	0.0991292

T-T Water (continued)

Run 3		Run 4	
Angular velocity, ω (rad/s)	**Torque, T (μNm)**	**Angular velocity, ω (rad/s)**	**Torque, T (μNm)**
0.100018	0.0382419	0.099987	0.0221502
0.884180	0.614781	0.884233	0.619312
1.668410	1.17771	1.668430	1.2019
2.452640	1.76595	2.452610	1.76874
3.236840	2.39318	3.236860	2.38339
4.021050	3.01044	4.021060	3.01396
4.805250	3.65938	4.805270	3.65075
5.589470	4.31102	5.589470	4.32962
6.373680	4.99783	6.373680	5.01157
7.157900	5.70204	7.157920	5.70052
7.157890	5.77139	7.157910	5.75236
6.373690	5.05603	6.373670	5.04824
5.589470	4.37335	5.589500	4.34956
4.805270	3.69685	4.805270	3.68039
4.021050	3.05359	4.021050	3.03465
3.236850	2.42095	3.236840	2.39806
2.452620	1.79061	2.452630	1.77269
1.668430	1.18345	1.668420	1.17593
0.884209	0.619587	0.884217	0.61227
0.0999975	0.0315393	0.0999893	0.0127641

T-T(B) Water

$\mu = 1.13$ mPas $\rho = 997.0$ kg/m^3

$\omega_{crit} = 10.1$ rad/s

Run 1		Run 2	
Angular velocity, ω (rad/s)	**Torque, T (μNm)**	**Angular velocity, ω (rad/s)**	**Torque, T (μNm)**
6.373690	5.08556	0.099994	0.0904659
5.589490	4.36228	0.884204	0.598838
4.805280	3.69351	1.668420	1.18254
4.021050	3.02941	2.452630	1.78646
3.236820	2.38213	3.236830	2.39798
2.452630	1.75899	4.021060	3.03508
1.668440	1.17222	4.805260	3.6859
0.884209	0.601856	5.589470	4.35078
0.099999	0.0494593	6.373690	5.04006
6.373680	4.97791	6.373680	5.08201
5.589470	4.29704	5.589460	4.38897
4.805260	3.63699	4.805280	3.70992
4.021050	2.99284	4.021070	3.05641
3.236850	2.37597	3.236840	2.41649
2.452640	1.76264	2.452620	1.79057
1.668420	1.15892	1.668410	1.19164
0.884199	0.604152	0.884208	0.605861
0.0999995	0.0442522	0.100026	0.0631072

Appendix 6: Rheological Measurements of Carrier Fluid Slurries

S-M1

$\mu = 2.50$ mPas $\tau_0 = 0.1$ Pa $\rho = 1096.3$ kg/m^3

$\omega_{crit} = 20.4$ rad/s $T_{min} = 6.1$ μNm

Run 1		**Run 2**	
Angular velocity, ω (rad/s)	**Torque, T (μNm)**	**Angular velocity, ω (rad/s)**	**Torque, T (μNm)**
16.857900	34.4145	16.857800	34.3411
15.810500	32.6207	15.810500	32.784
14.763100	30.6891	14.763300	30.8724
13.715800	28.9009	13.715800	28.8186
12.668300	27.1145	12.668400	27.2389
11.621100	25.2269	11.621100	25.258
10.573700	23.5801	10.573700	23.4397
9.526370	21.8233	9.526280	22.0393
8.478940	20.231	8.478880	19.9896
7.431600	18.418	7.431520	18.4507
6.384160	16.4193	6.384250	16.4937
5.336750	14.578	5.336800	14.6257
4.289500	12.7602	4.289390	12.9844
3.242120	10.9578	3.242120	11.2954

S-M2

μ = 2.26 mPas τ_0 = 0.1 Pa ρ = 1102.2 kg/m^3

ω_{crit} = 18.4 rad/s T_{min} = 5.3 μNm

Run 1		**Run 2**	
Angular velocity, ω (rad/s)	**Torque, T (μNm)**	**Angular velocity, ω (rad/s)**	**Torque, T (μNm)**
14.763100	27.5539	14.763100	27.9194
13.715800	25.951	13.715900	26.2784
12.668500	24.5372	12.668400	24.4576
11.621100	22.8194	11.621000	22.5703
10.573700	20.8254	10.573700	21.0182
9.526300	19.2256	9.526410	20.2587
8.478920	17.8342	8.479020	17.9332
7.431480	15.9095	7.431550	16.2968
6.384190	14.5366	6.384210	14.3729
5.336860	12.5841	5.336870	12.9889
4.289460	11.2298	4.289530	11.7972
3.242280	9.99881	3.241130	10.6482
2.194800	8.29304	2.194910	8.06902
1.147350	6.76457	1.147200	6.71247

S-MFT1

μ = 5.78 mPas τ_0 = 1.0 Pa ρ = 1238.6 kg/m^3

ω_{crit} = 41.8 rad/s T_{min} = 59.3 μNm

Run 1		**Run 2**	
Angular velocity, ω (rad/s)	**Torque, T (μNm)**	**Angular velocity, ω (rad/s)**	**Torque, T (μNm)**
20.000000	129.647	20.000000	135.358
18.952600	126.145	18.952600	131.38
17.905300	122.526	17.905300	127.238
16.857900	118.692	16.857900	123.017
15.810500	114.909	15.810500	118.878
14.763200	111.173	14.763100	114.671
13.715800	107.376	13.715800	110.556
12.668400	103.575	12.668400	106.529
11.621000	99.5961	11.621000	102.427
10.573700	95.6207	10.573700	98.2736
9.526310	91.5431	9.526410	94.041
8.478920	87.312	8.478940	89.7
7.431560	82.9607	7.431570	85.3063
6.384230	78.5918	6.384210	80.8392
5.336830	73.8925	5.336810	76.1831
4.289460	69.2727	4.289480	71.5406
–	–	3.242120	66.4759

S-MFT2

μ = 5.88 mPas τ_0 = 0.9 Pa ρ = 1238.6 kg/m^3

ω_{crit} = 42.5 rad/s T_{min} = 57.0 μNm

Run 1		**Run 2**	
Angular velocity, ω (rad/s)	**Torque, T (μNm)**	**Angular velocity, ω (rad/s)**	**Torque, T (μNm)**
20.000000	126.25	20.000000	137.523
18.952600	122.463	18.952600	133.61
17.905300	118.545	17.905200	129.47
16.858000	114.568	16.857900	125.333
15.810500	110.587	15.810500	121.216
14.763100	106.661	14.763200	117.039
13.715800	102.768	13.715800	112.932
12.668400	98.801	12.668400	108.736
11.621200	94.8164	11.621100	104.514
10.573700	90.7614	10.573700	100.255
9.526290	86.6231	9.526310	95.8909
8.478930	82.3111	8.478930	91.3827
7.431610	78.322	7.431560	86.868
6.384200	73.5569	6.384200	82.1909
5.336830	68.8361	5.336830	77.3549
4.289460	64.2404	4.289470	72.5224

S-TSRU1

$\mu = 1.96$ mPas $\tau_0 = 0.0$ Pa $\rho = 1046.6$ kg/m^3

$\omega_{crit} = 17.4$ rad/s $T_{min} = 1.7$ μNm

Run 1	
Angular velocity, ω (rad/s)	**Torque, T (μNm)**
10.573700	15.7478
9.526290	14.4962
8.478970	12.7265
7.431540	11.2819
6.384260	10.1129
5.336840	8.58449
4.289460	6.91609
3.241970	5.80155
2.194740	4.54103
1.147310	3.2994

S-TSRU2

μ = 2.54 mPas τ_0 = 0.0 Pa ρ = 1075.7 kg/m^3

ω_{crit} = 21.1 rad/s T_{min} = 2.5 μNm

Run 1	
Angular velocity, ω (rad/s)	**Torque, T (μNm)**
16.857900	32.2304
15.810500	29.7439
14.763200	27.8082
13.715800	25.9945
12.668400	24.0937
11.621100	22.252
10.573700	20.4258
9.526320	18.7318
8.478930	16.8182
7.431560	15.1657
6.384220	13.3278
5.336820	11.6181
4.289470	9.81987
3.242090	7.9718
2.194660	6.54578

S-TSRU3

μ = 2.04 mPas τ_0 = 0.0 Pa ρ = 1046.6 kg/m^3

ω_{crit} = 17.4 rad/s T_{min} = 0.6 μNm

Run 1		**Run 2**	
Angular velocity, ω (rad/s)	**Torque, T (μNm)**	**Angular velocity, ω (rad/s)**	**Torque, T (μNm)**
12.668400	18.3923	12.668400	18.9884
11.621100	16.1915	11.621200	17.1213
10.573600	14.6782	10.573700	15.3667
9.526310	13.5397	9.526400	14.1846
8.479050	12.1349	8.478960	12.6531
7.431460	10.3961	7.431430	11.2132
6.384180	8.91329	6.384150	9.5284
5.336810	7.53531	5.336880	8.49036
4.289450	6.24571	4.289490	6.73895
3.242170	4.89859	3.242100	5.41951
2.194720	3.57477	2.194700	4.28212

S-TT1

$\mu = 4.82$ mPas $\tau_0 = 1.1$ Pa $\rho = 1147.9$ kg/m^3

$\omega_{crit} = 37.6$ rad/s $T_{min} = 68.0$ μNm

Run 1		Run 2	
Angular velocity, ω (rad/s)	**Torque, T (μNm)**	**Angular velocity, ω (rad/s)**	**Torque, T (μNm)**
20.000000	129.068	20.000000	127.501
18.952600	125.592	18.952600	124.211
17.905300	121.96	17.905200	120.877
16.857900	118.382	16.857900	117.428
15.810500	114.804	15.810500	113.963
14.763200	111.457	14.763200	110.531
13.715800	107.959	13.715800	107.066
12.668400	104.521	12.668400	103.638
11.621000	101.127	11.621100	100.366
10.573700	97.7673	10.573800	96.9803
9.526300	94.3259	9.526320	93.6366
8.478940	90.9433	8.478930	90.2723
7.431560	87.5629	7.431570	86.9474
6.384200	84.0684	6.384200	83.4805
5.336820	80.5509	5.336840	79.8858
4.289470	76.9635	4.289470	76.1473
3.242100	73.0316	3.242120	72.2339

S-TT2

μ = 2.99 mPas τ_0 = 0.3 Pa ρ = 1131.1 kg/m^3

ω_{crit} = 23.6 rad/s T_{min} = 19.3 μNm

Run 1	
Angular velocity, ω (rad/s)	**Torque, T (μNm)**
20.000000	58.3497
18.952600	56.0641
17.905300	53.9813
16.857900	51.8686
15.810500	49.9646
14.763200	48.0089
13.715800	46.0363
12.668400	44.0124
11.621000	41.896
10.573700	39.6323
9.526310	37.6438
8.478940	35.3348
7.431560	33.1134
6.384220	30.8636
5.336830	28.5863
4.289480	26.1227
3.242080	23.6891

S-TT3

μ = 5.10 mPas τ_0 = 1.1 Pa ρ = 1147.9 kg/m^3

ω_{crit} = 39.8 rad/s T_{min} = 68.5 μNm

Run 1		**Run 2**	
Angular velocity, ω (rad/s)	**Torque, T (μNm)**	**Angular velocity, ω (rad/s)**	**Torque, T (μNm)**
20.000000	132.637	20.000000	131.879
18.952600	129.171	18.952600	128.455
17.905300	125.449	17.905300	124.894
16.857900	121.637	16.857900	121.395
15.810500	117.858	15.810600	117.876
14.763200	114.17	14.763100	114.271
13.715800	110.464	13.715700	110.669
12.668400	106.793	12.668400	107.105
11.621000	103.24	11.621000	103.551
10.573700	99.7051	10.573700	100.062
9.526310	96.128	9.526320	96.6651
8.478930	92.5176	8.478930	93.1268
7.431590	89.0075	7.431580	89.5696
6.384170	85.2725	6.384180	85.9322
5.336840	81.4506	5.336850	82.2579
4.289500	77.4051	4.289460	78.1632
3.242110	73.1388	3.242090	74.0501

S-TT3 (continued)

Run 3	
Angular velocity, ω (rad/s)	**Torque, T (μNm)**
20.000000	132.96
18.952600	129.52
17.905300	125.88
16.857900	122.153
15.810600	118.643
14.763200	114.954
13.715800	111.318
12.668500	107.672
11.621000	103.957
10.573700	100.09
9.526310	96.4398
8.478930	92.8731
7.431610	89.3081
6.384210	85.6235
5.336840	81.8065
4.289460	77.8123
3.242130	73.5476

SU-M1

μ = 3.90 mPas τ_0 = 0.4 Pa ρ = 1122.4 kg/m^3

ω_{crit} = 31.1 rad/s T_{min} = 23.3 μNm

Run 1		**Run 2**	
Angular velocity, ω (rad/s)	**Torque, T (μNm)**	**Angular velocity, ω (rad/s)**	**Torque, T (μNm)**
19.999900	75.4	19.999800	73.1326
18.952600	72.8994	18.952700	70.5777
17.905300	70.181	17.905300	68.1225
16.857900	67.2881	16.857900	65.2304
15.810500	64.5203	15.810400	62.8671
14.763200	61.7999	14.763100	59.9089
13.715800	58.8714	13.715700	57.4654
12.668400	56.0342	12.668400	54.3767
11.621000	53.1693	11.621100	51.9122
10.573700	50.4415	10.573700	48.7401
9.526300	47.3428	9.526290	45.9313
8.478940	44.7025	8.478860	43.3048
7.431570	41.2695	7.431550	40.3377

SU-NW1

μ = 3.19 mPas τ_0 = 0.0 Pa ρ = 1070.2 kg/m^3

ω_{crit} = 26.7 rad/s T_{min} = 1.4 μNm

Run 1		**Run 2**	
Angular velocity, ω (rad/s)	**Torque, T (μNm)**	**Angular velocity, ω (rad/s)**	**Torque, T (μNm)**
18.952600	43.0894	18.952600	43.2843
17.905300	40.2976	17.905300	40.1801
16.857900	37.9352	16.857900	37.747
15.810500	35.7314	15.810500	35.3862
14.763100	33.4263	14.763200	33.0508
13.715800	31.0258	13.715800	30.6904
12.668400	28.835	12.668500	28.4108
11.621000	26.5442	11.621100	26.1535
10.573700	24.3384	10.573700	23.9098
9.526380	22.1534	9.526320	21.8588
8.478930	20.2397	8.478940	19.5348
7.431550	17.9363	7.431590	17.5594
6.384250	15.5692	6.384210	15.2119

SU-RDW1

μ = 2.57 mPas τ_0 = 0.0 Pa ρ = 1031.3 kg/m^3

ω_{crit} = 22.3 rad/s T_{min} = 1.3 μNm

Run 1		**Run 2**	
Angular velocity, ω (rad/s)	**Torque, T (μNm)**	**Angular velocity, ω (rad/s)**	**Torque, T (μNm)**
15.810500	28.9426	15.810500	29.5197
14.763200	27.0243	14.763100	27.1839
13.715800	25.1031	13.715800	25.1487
12.668400	23.2823	12.668400	23.2686
11.621100	21.3898	11.621100	21.468
10.573700	19.5896	10.573700	19.6743
9.526340	17.9457	9.526320	17.9016
8.478940	16.044	8.478940	16.0422
7.431570	14.158	7.431580	14.1654
6.384220	12.4518	6.384190	12.4169
5.336850	10.6078	5.336850	10.6246
4.289490	8.78406	4.289490	8.85249

SU-T1

μ = 2.64 mPas τ_0 = 0.0 Pa ρ = 1077.7 kg/m^3

ω_{crit} = 21.9 rad/s T_{min} = 3.0 μNm

Run 1		**Run 2**	
Angular velocity, ω (rad/s)	**Torque, T (μNm)**	**Angular velocity, ω (rad/s)**	**Torque, T (μNm)**
14.763100	29.555	14.763200	29.5321
13.715900	27.3427	13.715800	27.2102
12.668500	25.8209	12.668400	25.2782
11.621100	24.2626	11.621000	23.4142
10.573700	21.8476	10.573700	21.651
9.526290	19.8055	9.526290	19.7654
8.478950	18.1343	8.478960	17.8336
7.431580	16.4656	7.431590	16.1559
6.384220	14.3922	6.384200	13.7937
5.336810	12.7197	5.336810	12.3578
4.289440	10.8627	–	–

SU-TF1

μ = 3.22 mPas τ_0 = 0.2 Pa ρ = 1091.9 kg/m^3

ω_{crit} = 26.4 rad/s T_{min} = 11.0 μNm

Run 1		**Run 2**	
Angular velocity, ω (rad/s)	**Torque, T (μNm)**	**Angular velocity, ω (rad/s)**	**Torque, T (μNm)**
18.952600	51.7444	20.000000	53.1863
17.905200	49.7288	18.952600	51.3611
16.858000	47.4203	17.905300	48.9869
15.810600	45.1105	16.857800	46.6991
14.763200	42.9278	15.810500	44.5831
13.715700	40.5374	14.763200	42.4796
12.668400	38.3711	13.715800	40.0651
11.621100	35.9294	12.668400	37.8218
10.573700	33.5683	11.621000	35.4998
9.526290	31.374	10.573700	33.2637
8.479000	29.0876	9.526330	31.0326
7.431570	26.7998	8.478960	28.6422
6.384270	24.3459	7.431600	26.225
5.336860	21.9053	6.384300	24.0519
–	–	5.336860	21.4883
–	–	4.289450	18.9426
–	–	3.242090	16.2882

SU-TF2

μ = 3.67 mPas τ_0 = 0.4 Pa ρ = 1127.8 kg/m^3

ω_{crit} = 29.2 rad/s T_{min} = 22.2 μNm

Run 1		**Run 2**	
Angular velocity, ω (rad/s)	**Torque, T (μNm)**	**Angular velocity, ω (rad/s)**	**Torque, T (μNm)**
20.000000	70.1443	20.000000	70.0786
18.952600	67.4996	18.952600	67.8609
17.905300	65.0272	17.905200	65.4861
16.857900	62.408	16.858000	63.0994
15.810600	59.9257	15.810500	60.6358
14.763100	57.6531	14.763100	57.859
13.715800	54.6905	13.715800	55.1164
12.668400	52.0585	12.668400	52.5434
11.621100	49.1075	11.621100	49.809
10.573700	46.6232	10.573700	47.252
9.526010	44.2696	9.526290	44.4353
8.479060	41.7754	8.478920	41.5095
7.431620	38.8223	7.431620	38.8613
6.384300	36.1267	6.384230	36.1272

SU-TPSC1

μ = 3.16 mPas τ_0 = 0.2 Pa ρ = 1087.0 kg/m^3

ω_{crit} = 26.0 rad/s T_{min} = 12.5 μNm

Run 1		**Run 2**	
Angular velocity, ω (rad/s)	**Torque, T (μNm)**	**Angular velocity, ω (rad/s)**	**Torque, T (μNm)**
20.000000	54.4027	20.000000	53.7035
18.952600	52.7178	18.952600	51.8097
17.905300	50.6248	17.905200	49.6852
16.857900	48.3837	16.857900	47.6538
15.810500	46.2106	15.810500	45.3839
14.763200	43.9596	14.763200	43.0967
13.715800	41.7	13.715800	40.8421
12.668400	39.2761	12.668400	38.5888
11.621100	36.8954	11.621100	36.2975
10.573700	34.5352	10.573700	34.2278
9.526300	32.2731	9.526320	31.9015
8.478940	29.9022	8.478950	29.6136
7.431570	27.4615	7.431570	27.2757
6.384190	25.073	6.384230	24.8021

SU-TSF1

μ = 3.59 mPas τ_0 = 0.3 Pa ρ = 1114.9 kg/m^3

ω_{crit} = 28.9 rad/s T_{min} = 19.3 μNm

Run 1		**Run 2**	
Angular velocity, ω (rad/s)	**Torque, T (μNm)**	**Angular velocity, ω (rad/s)**	**Torque, T (μNm)**
20.000000	66.3809	20.000000	65.7459
18.952700	64.4338	18.952600	63.6108
17.905200	62.0516	17.905200	61.4558
16.857800	59.8679	16.857900	58.7582
15.810700	57.3373	15.810600	56.3981
14.763100	54.7079	14.763100	53.986
13.715800	51.9273	13.715700	51.3078
12.668400	49.2864	12.668400	48.6802
11.621000	46.3308	11.621100	46.1037
10.573700	43.9429	10.573700	43.5901
9.526280	41.1681	9.526290	41.13
8.478920	38.75	8.478980	38.3235
7.431610	35.9819	7.431600	35.8225
6.384210	33.0595	6.384200	32.9194

SY-HT1

μ = 5.36 mPas τ_0 = 3.2 Pa ρ = 1300.7 kg/m^3

ω_{crit} = 36.9 rad/s T_{min} = 194.1 μNm

Run 1		**Run 2**	
Angular velocity, ω (rad/s)	**Torque, T (μNm)**	**Angular velocity, ω (rad/s)**	**Torque, T (μNm)**
20.000000	243.88	20.000100	259.08
18.952600	240.695	18.952600	255.103
17.905200	237.288	17.905200	251.281
16.857900	233.799	16.857900	247.48
15.810500	230.109	15.810500	243.355
14.763200	226.453	14.763100	239.349
13.715800	223.124	13.715800	234.97
12.668400	220.118	12.668400	230.566
11.621000	215.369	11.621000	225.633
10.573700	211.13	10.573700	221.577
9.526280	207.855	9.526310	217.702
8.478970	204.503	8.479020	214.07
7.431560	201.516	7.431570	210.297
6.384180	198.354	6.384190	207.014
5.336830	194.986	5.336830	201.969

SY-M1

μ = 3.18 mPas τ_0 = 0.4 Pa ρ = 1150.8 kg/m^3

ω_{crit} = 24.8 rad/s T_{min} = 27.4 μNm

Run 1		**Run 2**	
Angular velocity, ω (rad/s)	**Torque, T (μNm)**	**Angular velocity, ω (rad/s)**	**Torque, T (μNm)**
17.905200	67.3888	19.999900	64.2728
16.857900	65.4846	18.952600	62.1163
15.810500	63.257	17.905300	60.0517
14.763200	61.1968	16.857800	57.9517
13.715800	59.0984	15.810500	55.9739
12.668400	56.6818	14.763200	53.5702
11.621100	54.4507	13.715800	51.4766
10.573700	52.1772	12.668400	49.2891
9.526330	49.7584	11.621100	46.9909
8.478940	47.5438	10.573700	44.8583
7.431560	45.2252	9.526270	42.5857
6.384220	42.6651	8.478920	40.0693
5.336810	40.1649	7.431570	37.6373
4.289450	37.6086	6.384220	35.2024
–	–	5.336820	32.5559
–	–	4.289460	30.6521

SY-T1

μ = 3.00 mPas τ_0 = 0.4 Pa ρ = 1172.1 kg/m^3

ω_{crit} = 22.9 rad/s T_{min} = 26.8 μNm

Run 1		**Run 2**	
Angular velocity, ω (rad/s)	**Torque, T (μNm)**	**Angular velocity, ω (rad/s)**	**Torque, T (μNm)**
20.000000	62.5038	20.000000	67.8308
18.952600	60.6207	18.952700	66.1458
17.905300	58.7344	17.905200	63.8796
16.857900	56.7661	16.857800	61.8913
15.810500	54.8537	15.810600	59.661
14.763100	52.7929	14.763100	57.4189
13.715800	50.8194	13.715800	55.1859
12.668500	48.7647	12.668500	52.993
11.621000	46.6538	11.621000	50.6027
10.573700	44.4647	10.573700	48.3544
9.526310	42.1533	9.526300	45.9164
8.478960	40.0018	8.478930	43.5156
–	–	7.431590	40.9778

T-T1

μ = 1.54 mPas τ_0 = 0.0 Pa ρ = 1027.4 kg/m^3

ω_{crit} = 13.4 rad/s T_{min} = 0.0 μNm

Run 1		Run 2	
Angular velocity, ω (rad/s)	**Torque, T (μNm)**	**Angular velocity, ω (rad/s)**	**Torque, T (μNm)**
9.526330	10.603	9.526310	9.74757
8.478940	9.30528	8.478950	8.54917
7.431570	8.06396	7.431570	7.38622
6.384210	6.87784	6.384210	6.2619
5.336840	5.68164	5.336830	5.1559
4.289470	4.52291	4.289470	4.07986
3.242090	3.3857	3.242110	3.02249
2.194740	2.30044	2.194730	2.03548
1.147350	1.264	1.147350	1.07166
0.099998	0.13941	0.100008	0.173013
0.100011	0.114546	0.099997	0.206062
1.147380	1.25752	1.147370	1.08477
2.194730	2.3032	2.194720	2.03952
3.242090	3.38563	3.242120	3.01523
4.289480	4.52272	4.289470	4.07003
5.336830	5.69622	5.336840	5.15615
6.384210	6.9136	6.384210	6.28493
7.431560	8.15974	7.431570	7.48091
8.478950	9.46912	8.478950	8.66708
9.526320	10.8151	9.526300	9.93349

T-T2

μ = 1.96 mPas τ_0 = 0.0 Pa ρ = 1071.0 kg/m^3

ω_{crit} = 16.4 rad/s T_{min} = 0.0 μNm

Run 1	
Angular velocity, ω (rad/s)	**Torque, T (μNm)**
10.573700	14.188
9.526310	12.6927
8.478950	11.191
7.431590	9.72665
6.384210	8.33981
5.336850	7.03374
4.289500	5.64052
3.242090	4.30762
2.194720	3.07134
1.147380	1.9034
0.100013	0.227746
0.100011	0.257387
1.147380	1.79476
2.194750	2.99815
3.242110	4.2254
4.289470	5.58445
5.336850	6.97799
6.384210	8.40925
7.431570	9.91674
8.478950	11.4791
9.526320	13.0246
10.573700	14.6141

T-T3

μ = 1.55 mPas τ_0 = 0.0 Pa ρ = 1027.4 kg/m^3

ω_{crit} = 13.5 rad/s T_{min} = 0.0 μNm

Run 1		**Run 2**	
Angular velocity, ω (rad/s)	**Torque, T (μNm)**	**Angular velocity, ω (rad/s)**	**Torque, T (μNm)**
9.526330	10.2445	9.526300	10.2858
8.478950	9.08036	8.478940	8.97649
7.431570	7.86959	7.431620	7.84841
6.384230	6.65105	6.384210	6.63266
5.336810	5.5045	5.336860	5.50656
4.289460	4.35664	4.289430	4.3463
3.242110	3.25165	3.242050	3.25981
2.194740	2.19431	2.194740	2.17883
1.147390	1.28849	1.147310	1.13294
0.099997	0.143871	0.099995	0.365611

T-T(B)1

μ = 1.46 mPas τ_0 = 0.0 Pa ρ = 1033.7 kg/m^3

ω_{crit} = 12.7 rad/s T_{min} = 0.0 μNm

Run 1	
Angular velocity, ω (rad/s)	**Torque, T (μNm)**
9.526260	9.73861
8.478950	8.54861
7.431590	7.37601
6.384210	6.2545
5.336830	5.19032
4.289470	4.08553
3.242090	3.03882
2.194740	2.08808
1.147380	1.03596
0.100012	0.0612292
0.100007	0.0952445
1.147360	1.07024
2.194740	2.01789
3.242120	3.01929
4.289470	4.0394
5.336840	5.11181
6.384210	6.23591
7.431580	7.41307
8.478950	8.58711
9.526310	9.81328
9.526260	9.73861

Appendix 7: FPIA Settings and Sample Dispersion Information

Sheath Fluid Information

Aqueous ‘Particle Sheath Reagent” solution contains:

–7.1 g/L sodium chloride

–0.6 g/L surfactant

–2.0 g/L tris buffer

–0.2 g/L EDTA-2K

Shear Sensitivity Measurements

Kaolin-water suspension mixed at 400 RPM for 90 minutes.

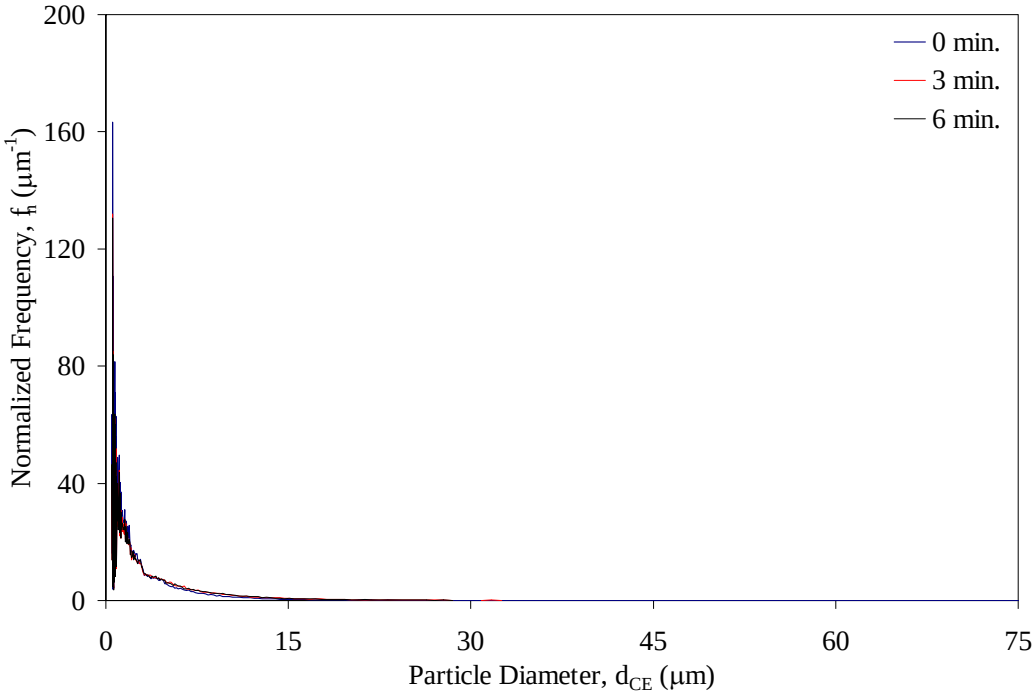

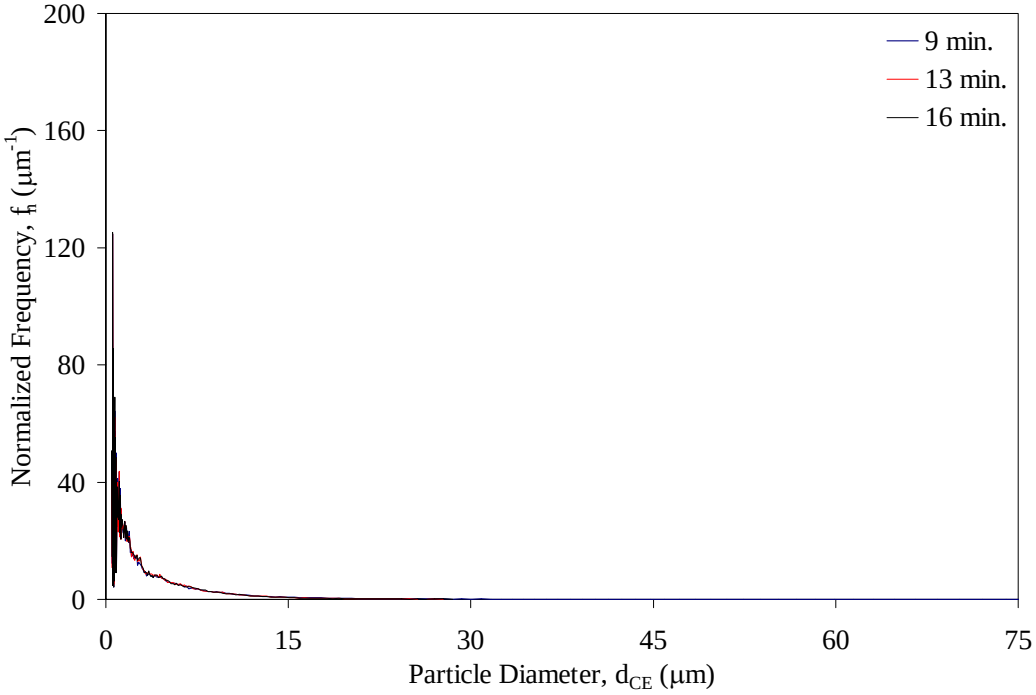

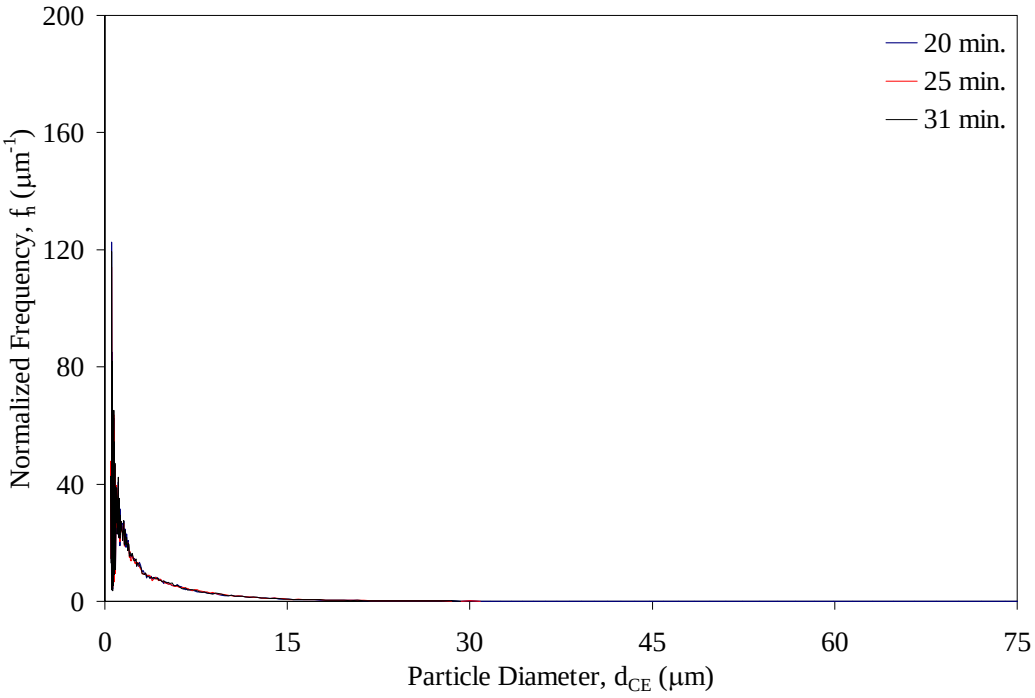
20 min.
25 min.
31 min.
Normalized Frequency, f (µm-1)
Particle Diameter, dCE (µm)
0
40
80
120
160
200
0
15
30
45
60
75

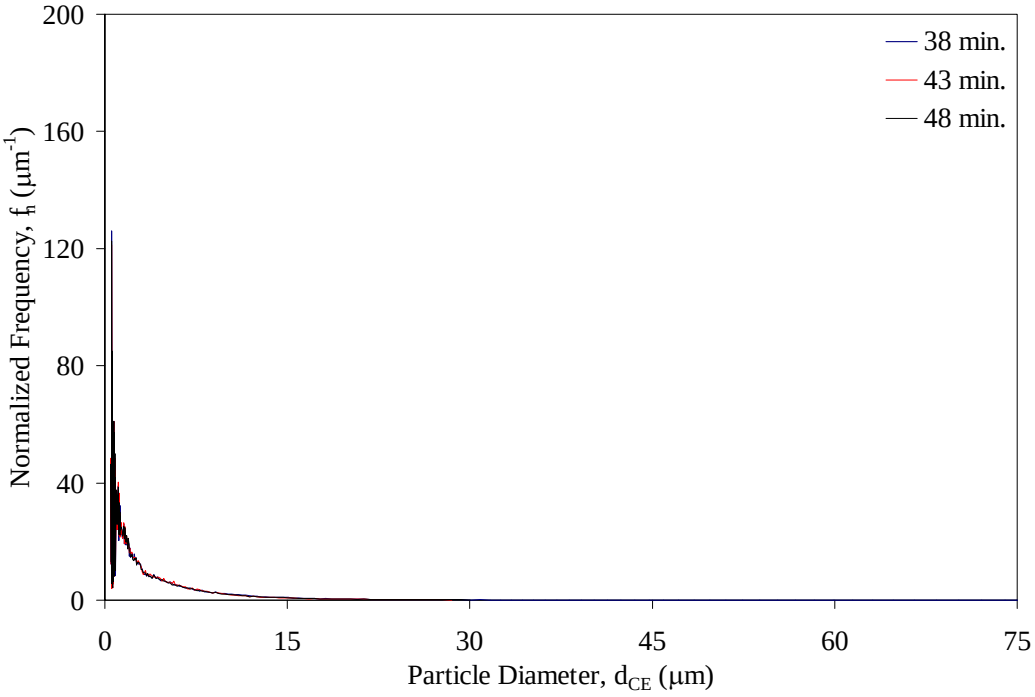
38 min.
43 min.
48 min.
Normalized Frequency, f (µm-1)
Particle Diameter, dCE (µm)
0
40
80
120
160
200
0
15
30
45
60
75

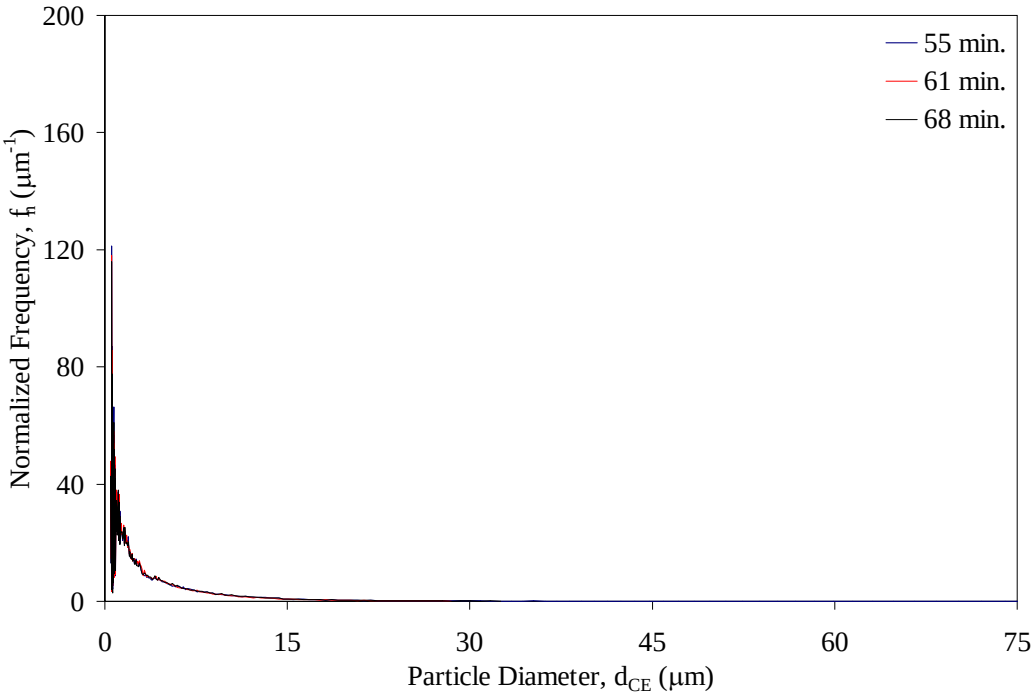
55 min.
61 min.
68 min.
Normalized Frequency, f_t (μm^{-1})
0
40
80
120
160
200
0
15
30
45
60
75
Particle Diameter, d_{CE} (μm)

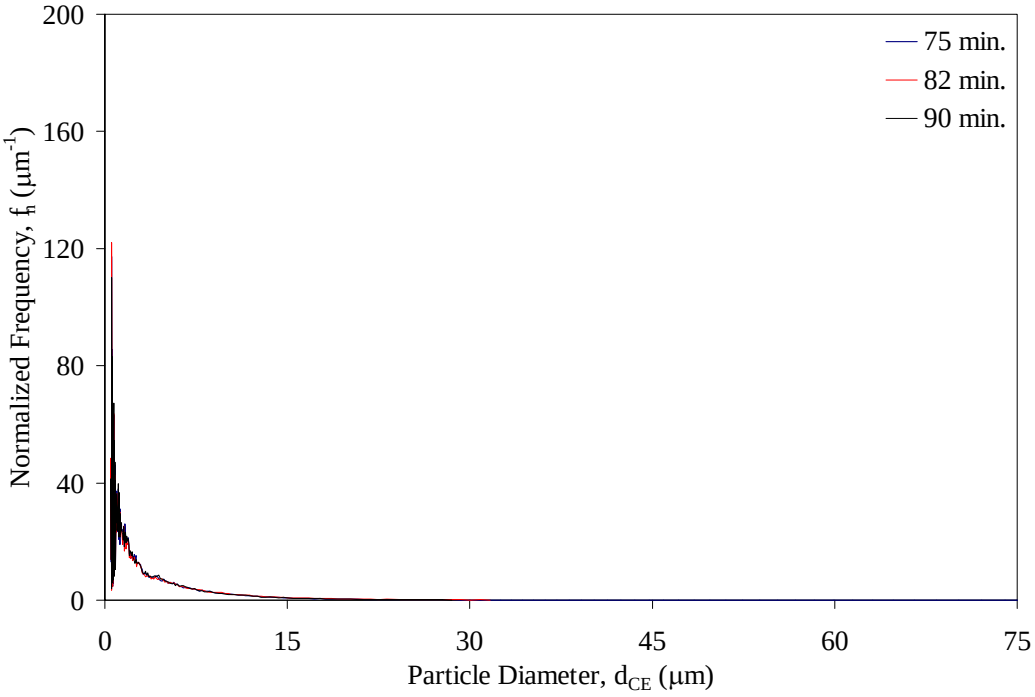
75 min.
82 min.
90 min.
Normalized Frequency, f_t (μm^{-1})
0
40
80
120
160
200
0
15
30
45
60
75
Particle Diameter, d_{CE} (μm)

S-M

Mass of TSPP = 0.05 g

Volume of 0.25 M NaOH = 4 mL

FPIA Ultrasonic Power = 5%

FPIA Pre-Test Irradiation Time = 10 s

Dispersion Information

Run	Sonication Time (min:sec)	Sonication Energy (J)	Sample Temperature (°C)
1	2:50	14220	19
2	6:20	30000	21
3	9:55	47000	22

S-MFT

Mass of TSPP = 0.04 g

Volume of 0.25 M NaOH = ?

FPIA Ultrasonic Power = 5%

FPIA Pre-Test Irradiation Time = 10 s

Dispersion Information

Run	Sonication Time (min:sec)	Sonication Energy (J)	Sample Temperature (°C)
1	1:30	6900	15
2	4:40	21500	21
3	7:50	35700	22

S-TSRU

Mass of TSPP = 0.05 g

Volume of 0.25 M NaOH = 4 mL

FPIA Ultrasonic Power = 50%

FPIA Pre-Test Irradiation Time = 10 s

Dispersion Information

Run	Sonication Time (min:sec)	Sonication Energy (J)	Sample Temperature (°C)
1	1:40	7700	15
2	4:50	22200	21
3	8:00	36500	22

S-TT

Mass of TSPP = 0.05 g

Volume of 0.25 M NaOH = 2.0 mL

FPIA Ultrasonic Power = 5%

FPIA Pre-Test Irradiation Time = 10 s

Dispersion Information

Run	Sonication Time (min:sec)	Sonication Energy (J)	Sample Temperature (°C)
1	1:20	6500	15
2	4:30	21100	21
3	7:40	35500	22

SU-M

Mass of TSPP = 0.05 g

Volume of 0.25 M NaOH = 4.5 mL

FPIA Ultrasonic Power = 5%

FPIA Pre-Test Irradiation Time = 20 s

Dispersion Information

Run	Sonication Time (min:sec)	Sonication Energy (J)	Sample Temperature (°C)
1	24:40	115500	22
2	28:05	129900	22
3	30:45	141200	23

SU-NW

Mass of TSPP = 0.05 g

Volume of 0.10 M NaOH = 5 mL

FPIA Ultrasonic Power = 50%

FPIA Pre-Test Irradiation Time = 10 s

Dispersion Information

Run	Sonication Time (min:sec)	Sonication Energy (J)	Sample Temperature (°C)
1	1:15	6000	19
2	4:25	21200	24
3	7:35	35200	24

SU-RDW

Mass of TSPP = 0.05 g

Volume of 0.25 M NaOH = 4 mL

FPIA Ultrasonic Power = 5%

FPIA Pre-Test Irradiation Time = 10 s

Dispersion Information

Run	Sonication Time (min:sec)	Sonication Energy (J)	Sample Temperature (°C)
1	2:25	11900	19
2	5:30	26800	22
3	8:50	41900	22

SU-T

Mass of TSPP = 0.05 g

Volume of 0.25 M NaOH = 4 mL

FPIA Ultrasonic Power = 5%

FPIA Pre-Test Irradiation Time = 10 s

Dispersion Information

Run	Sonication Time (min:sec)	Sonication Energy (J)	Sample Temperature (°C)
1	2:20	12100	19
2	5:30	26900	22
3	8:40	42000	22

SU-TF

Mass of TSPP = 0.05g

Volume of 0.25 M NaOH = 4 mL

FPIA Ultrasonic Power = 5%

FPIA Pre-Test Irradiation Time = 10 s

Dispersion Information

Run	Sonication Time (min:sec)	Sonication Energy (J)	Sample Temperature (°C)
1	2:20	11400	19
2	5:30	26500	22
3	8:40	40300	22

SU-TPSC

Mass of TSPP = 0.05 g

Volume of 0.25 M NaOH = 4.5 mL

FPIA Ultrasonic Power = 5%

FPIA Pre-Test Irradiation Time = 20 s

Dispersion Information

Run	Sonication Time (min:sec)	Sonication Energy (J)	Sample Temperature (°C)
1	29:20	130800	21
2	32:30	144000	21
3	36:15	159900	21

SU-TSF

Mass of TSPP = 0.05 g

Volume of 0.25 M NaOH = 3.0 mL

FPIA Ultrasonic Power = 5%

FPIA Pre-Test Irradiation Time = 20 s

Dispersion Information

Run	Sonication Time (min:sec)	Sonication Energy (J)	Sample Temperature (°C)
1	12:20	56500	21
2	15:50	72000	21
3	19:10	85900	21

SY-HT

Mass of TSPP = 0.05 g

Volume of 0.25 M NaOH = 3.0 mL

FPIA Ultrasonic Power = 50%

FPIA Pre-Test Irradiation Time = 10 s

Dispersion Information

Run	Sonication Time (min:sec)	Sonication Energy (J)	Sample Temperature (°C)
1	20:10	93500	22

SY-M

Mass of TSPP = 0.05 g

Volume of 0.25 M NaOH = 2.0 mL

FPIA Ultrasonic Power = 5%

FPIA Pre-Test Irradiation Time = 10 s

Dispersion Information

Run	Sonication Time (min:sec)	Sonication Energy (J)	Sample Temperature (°C)
1	5:40	27500	20
2	8:50	41300	21
3	12:00	55700	21

SY-T

Mass of TSPP = 0.07 g

Volume of 0.25 M NaOH = 2.0 mL

FPIA Ultrasonic Power = 5%

FPIA Pre-Test Irradiation Time = 10 s

Dispersion Information

Run	Sonication Time (min:sec)	Sonication Energy (J)	Sample Temperature (°C)
1	8:10	39000	20
2	11:20	53500	22

T-T

Mass of TSPP = 0.05 g

Volume of 0.25 M NaOH = 1.0 mL

FPIA Ultrasonic Power = 5%

FPIA Pre-Test Irradiation Time = 10 s

Dispersion Information

Run	Sonication Time (min:sec)	Sonication Energy (J)	Sample Temperature (°C)
1	1:20	4800	14
2	4:30	19500	21
3	7:40	33900	21

T-T(B)

Mass of TSPP = 0.05 g

Volume of 0.25 M NaOH = 1.0 mL

FPIA Ultrasonic Power = 5%

FPIA Pre-Test Irradiation Time = 10 s

Dispersion Information

Run	Sonication Time (min:sec)	Sonication Energy (J)	Sample Temperature (°C)
1	1:00	5500	15
2	4:10	20600	21
3	7:20	35400	22

Appendix 8: Particle Size Distributions of Carrier Fluid Samples

S-M

Aggregated

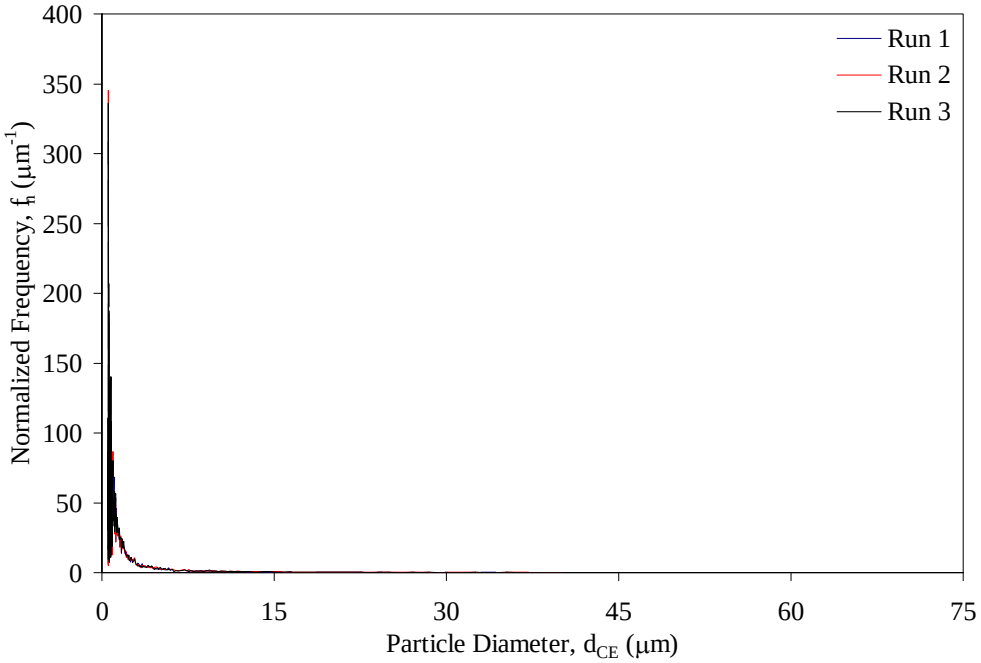

Dispersed

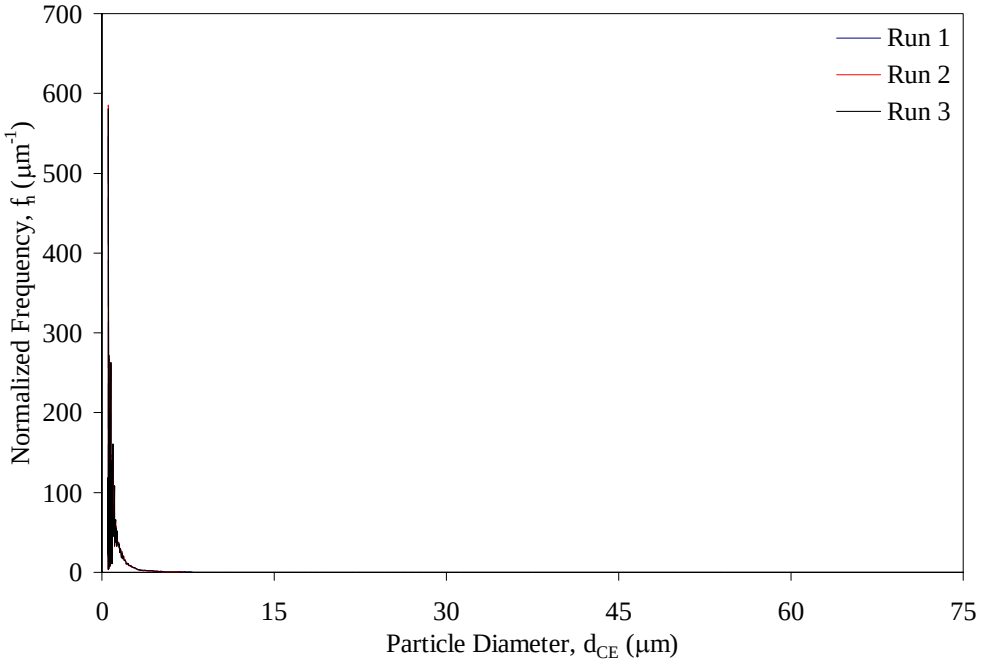

S-MFT

Aggregated

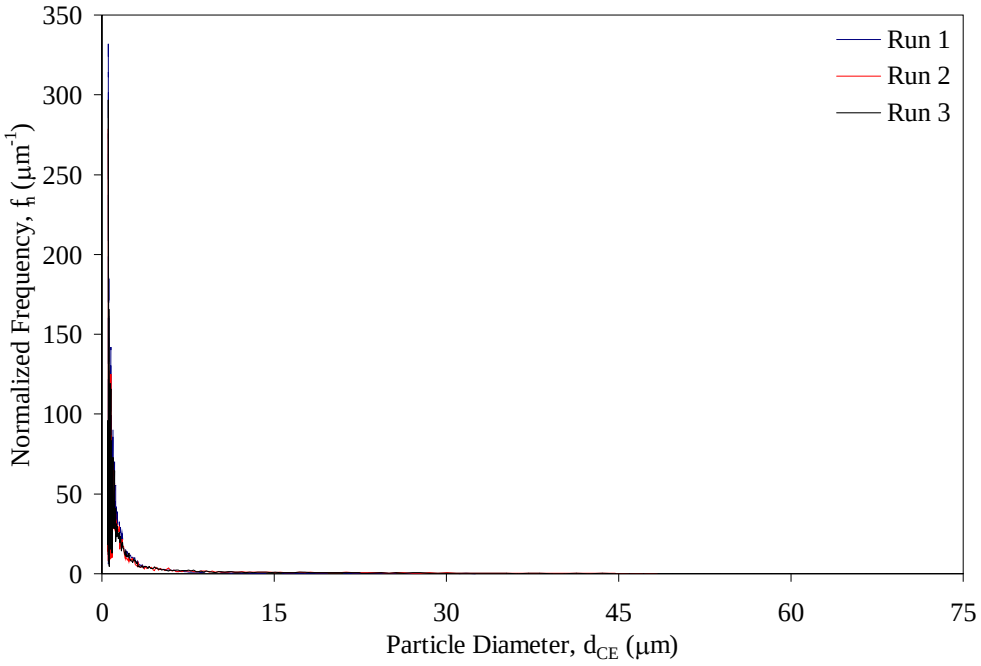

Dispersed

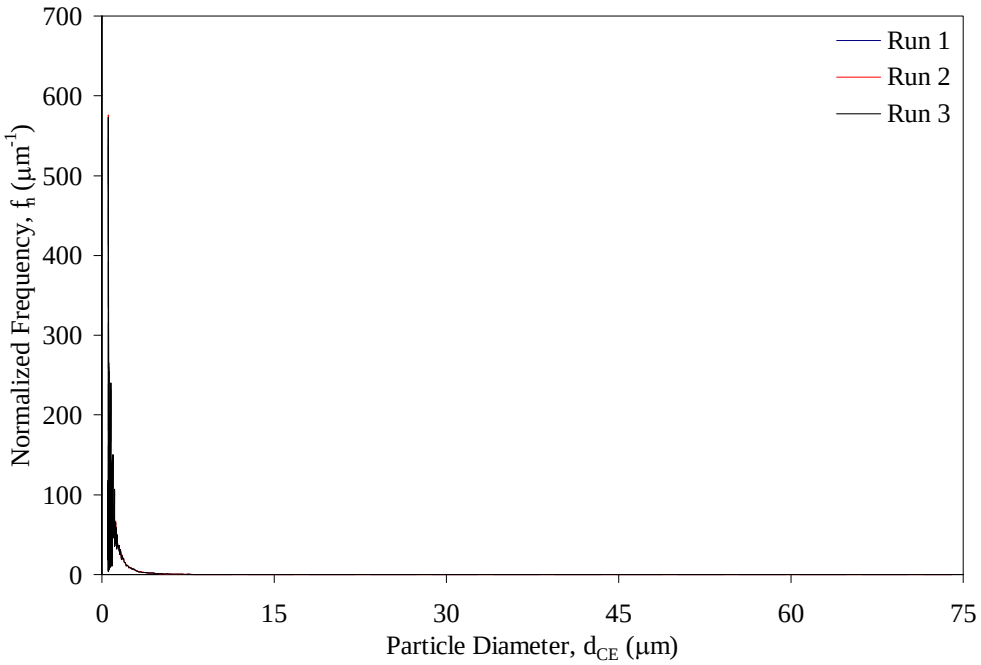

S-TSRU

Aggregated

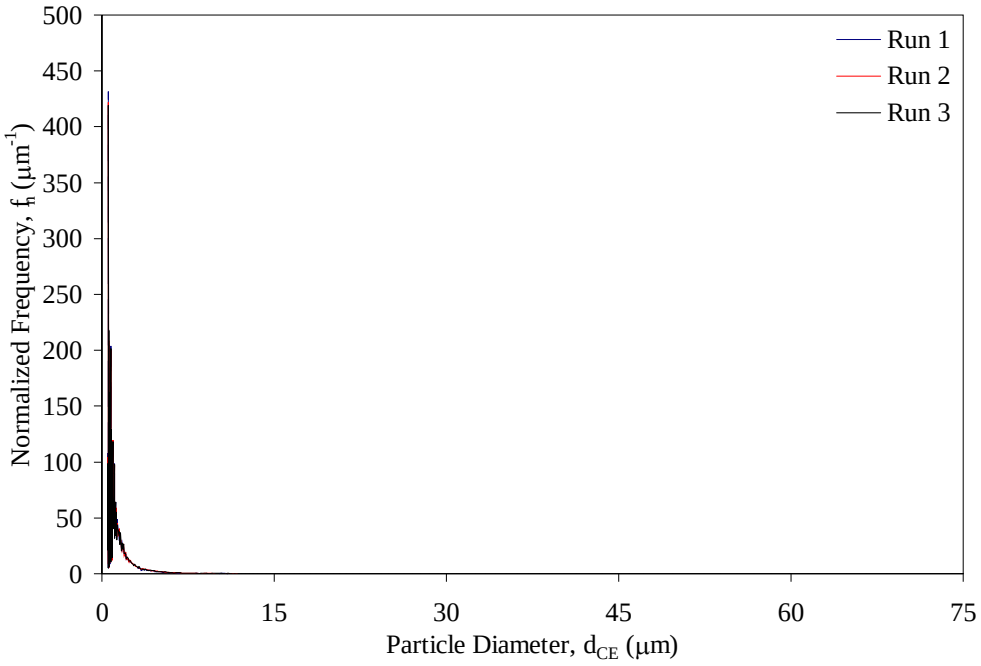

Dispersed

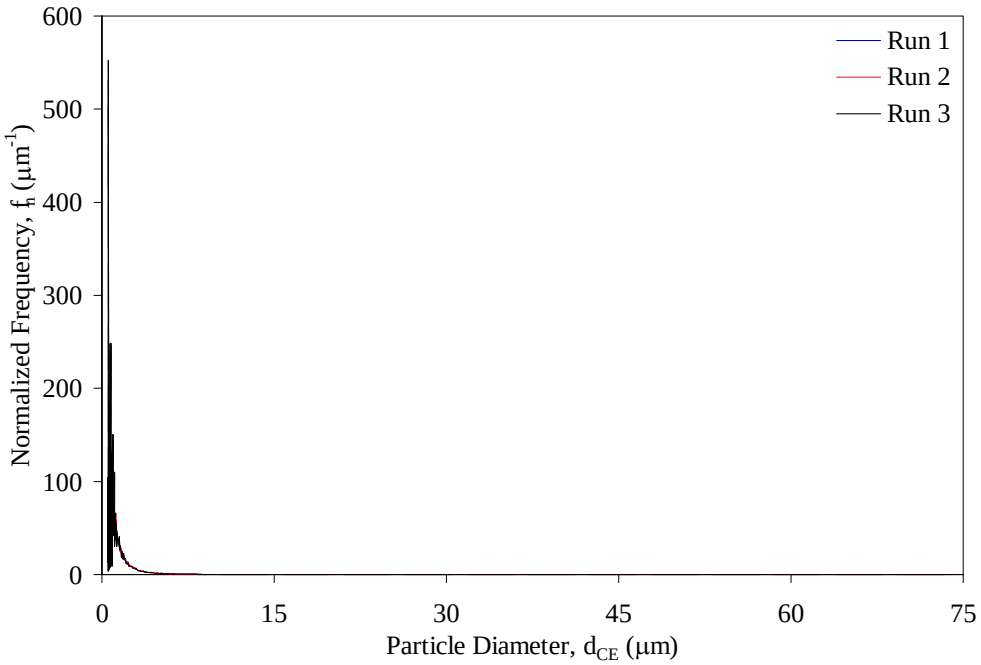

S-TT

Aggregated

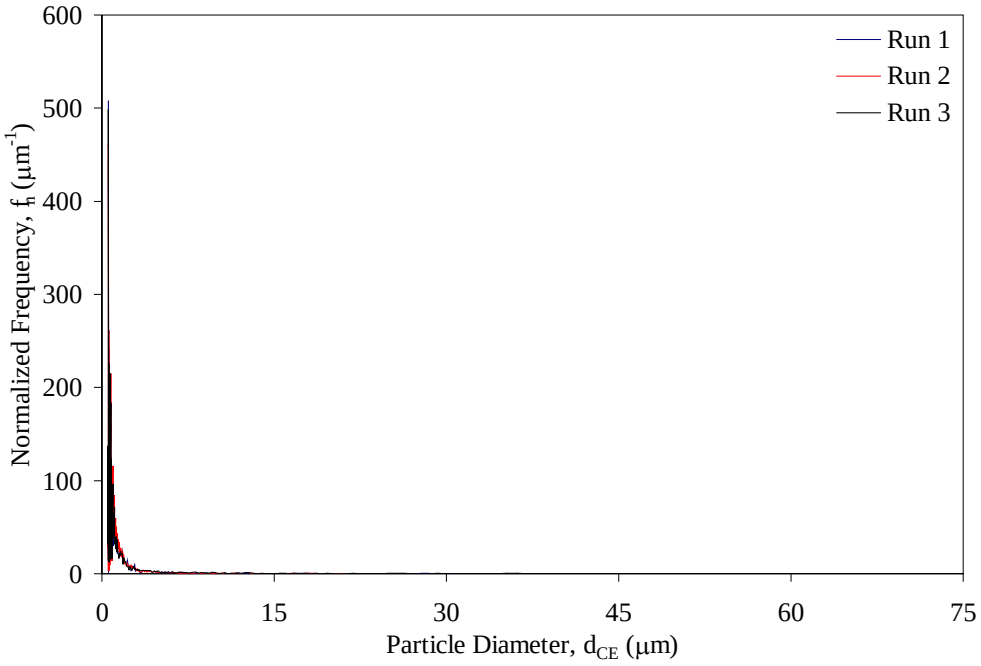

Dispersed

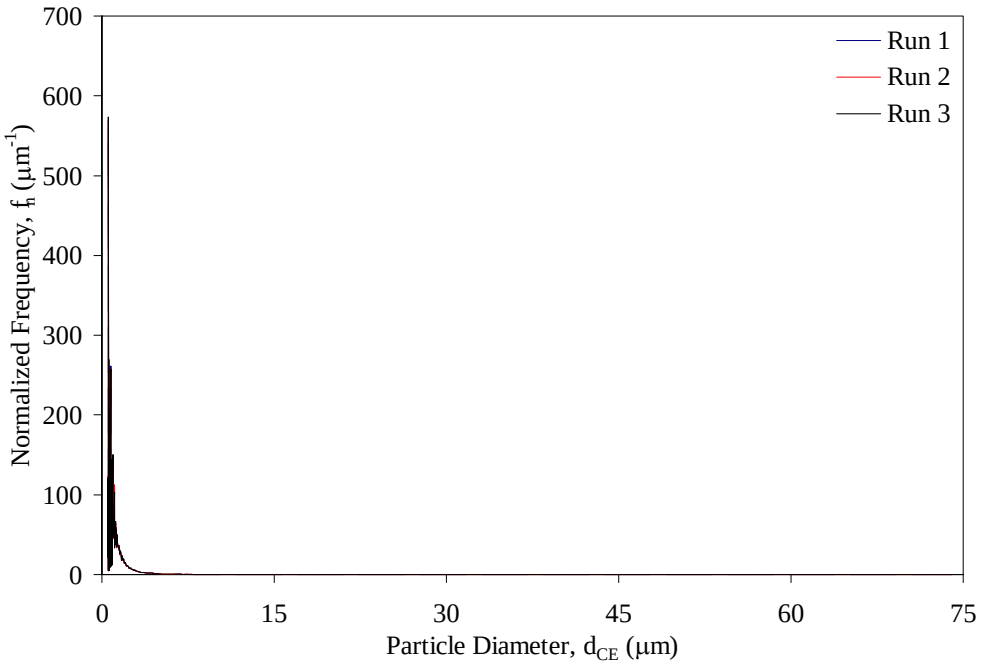

SU-M

Aggregated

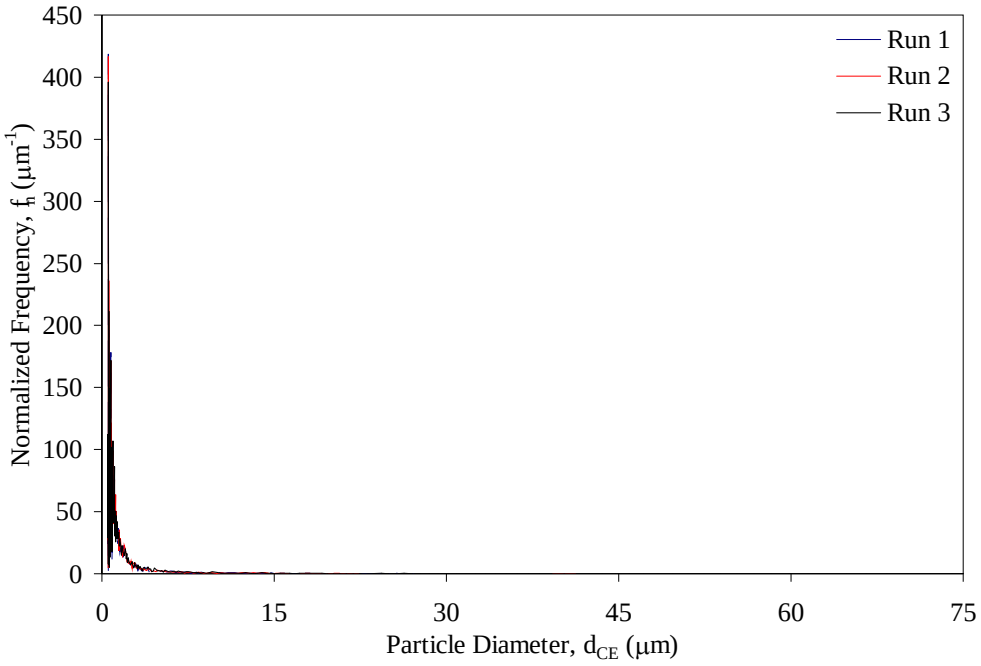

Dispersed

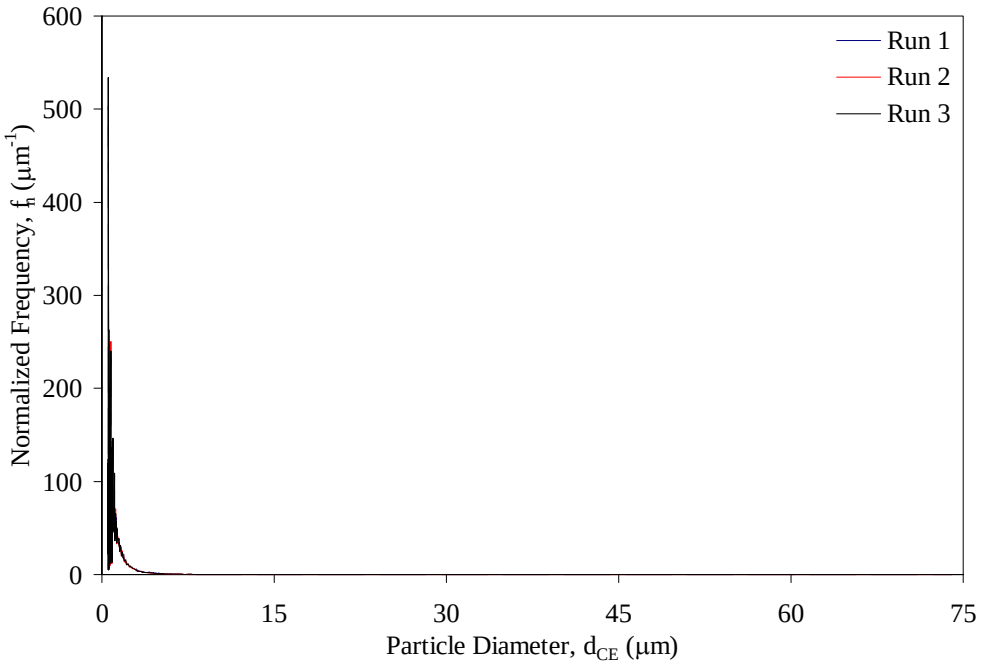

SU-NW

Aggregated

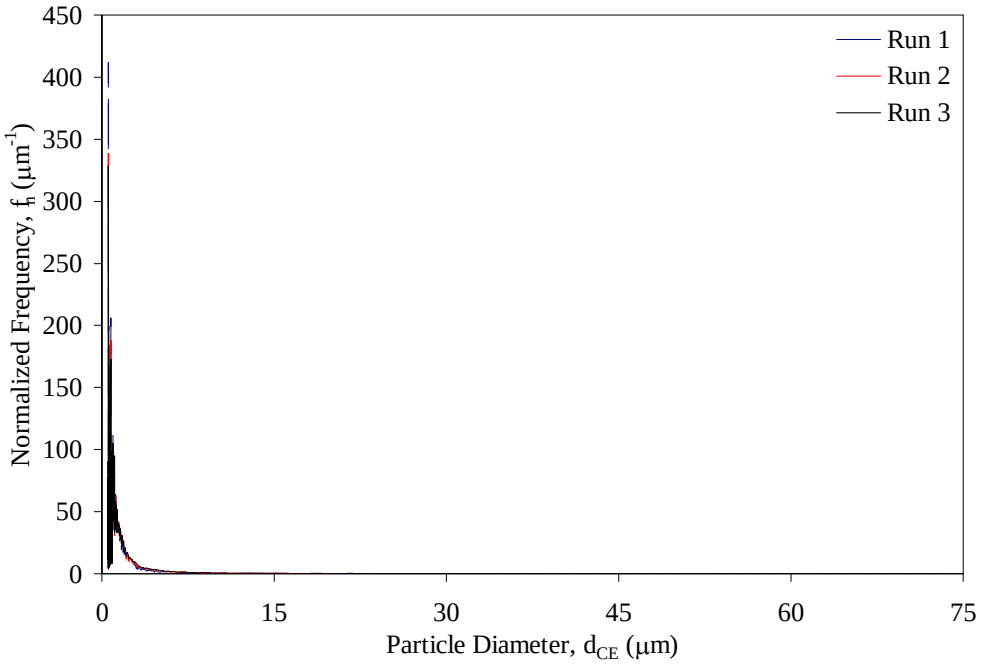

Dispersed

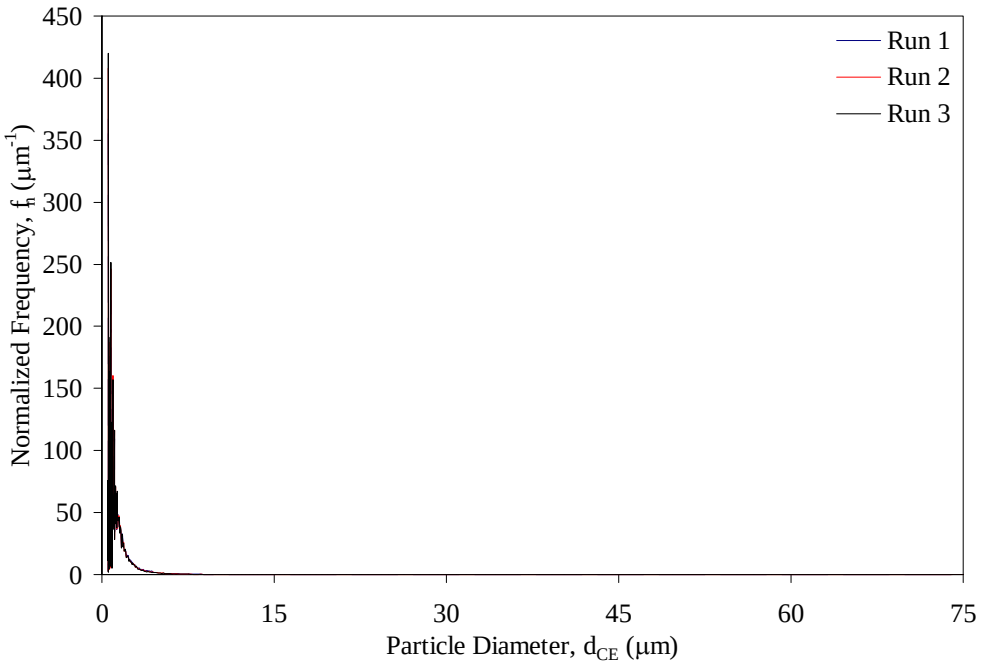

SU-RDW

Aggregated

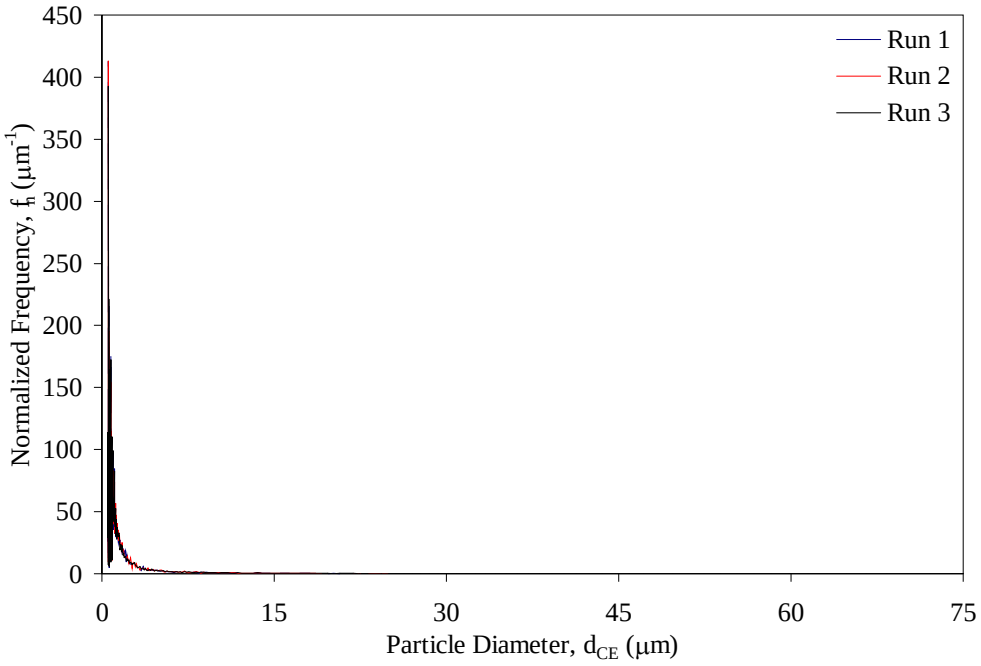

Dispersed

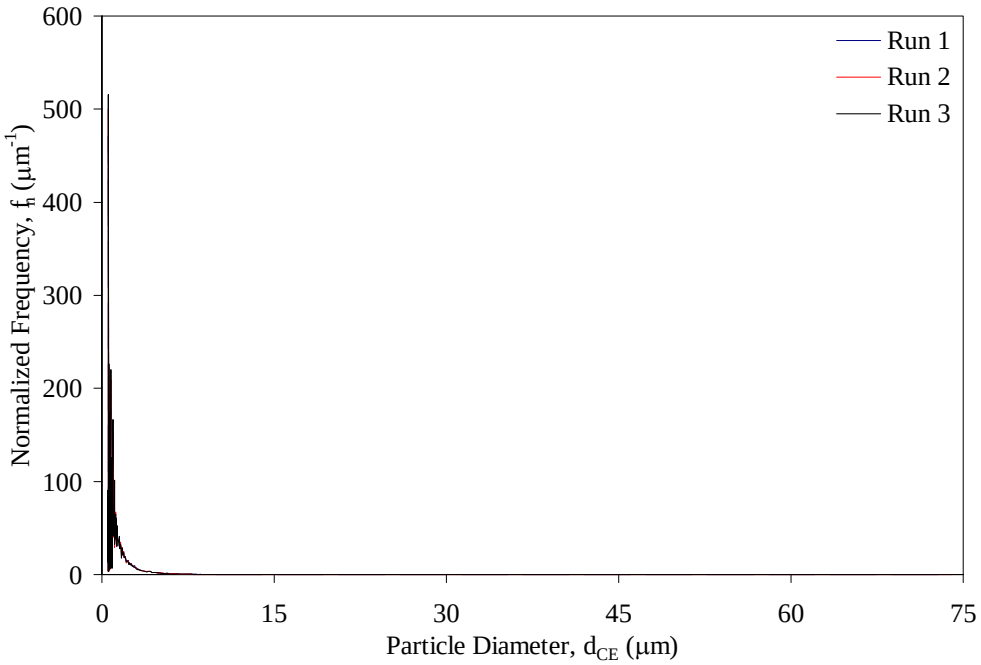

SU-T

Aggregated

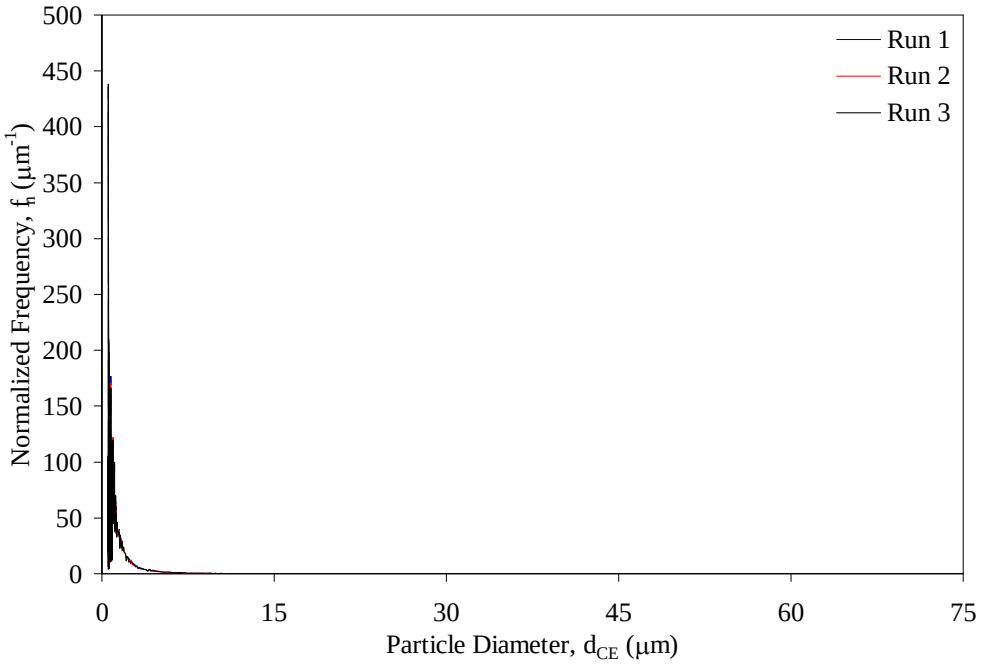

Dispersed

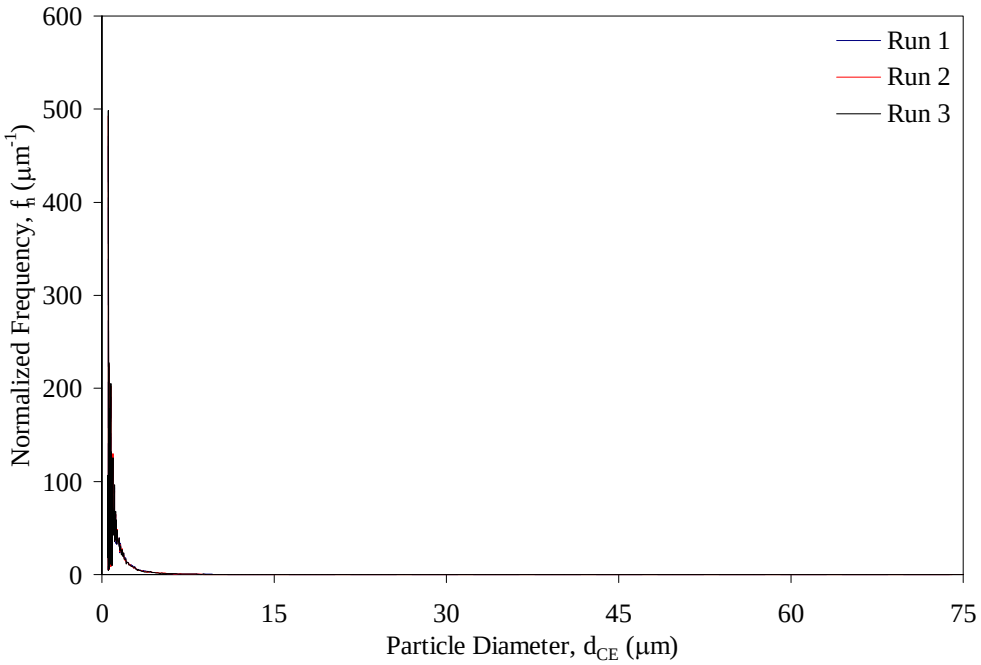

SU-TF

Aggregated

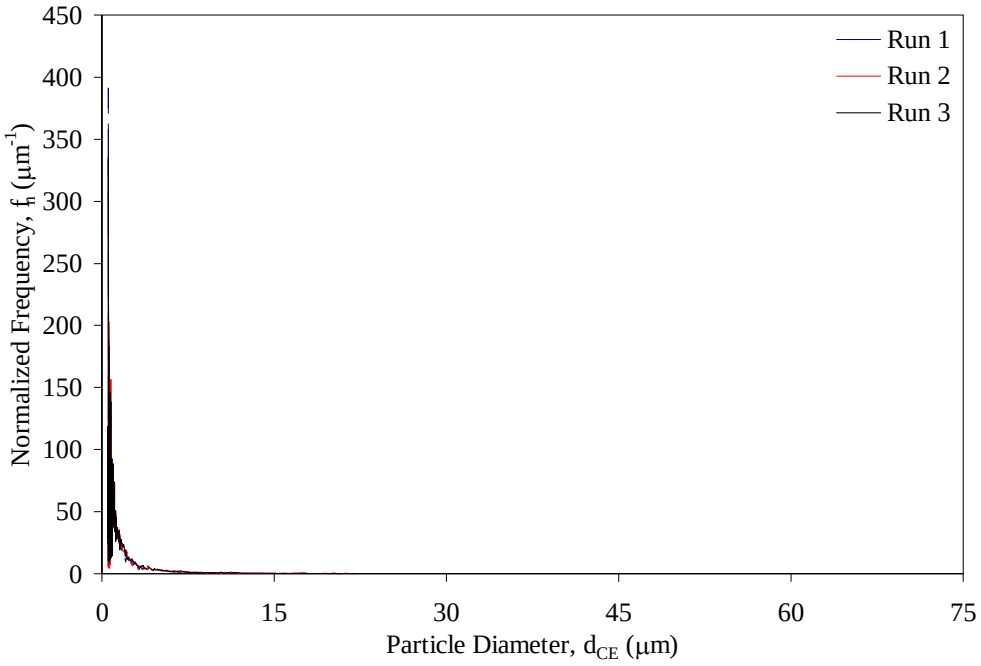

Dispersed

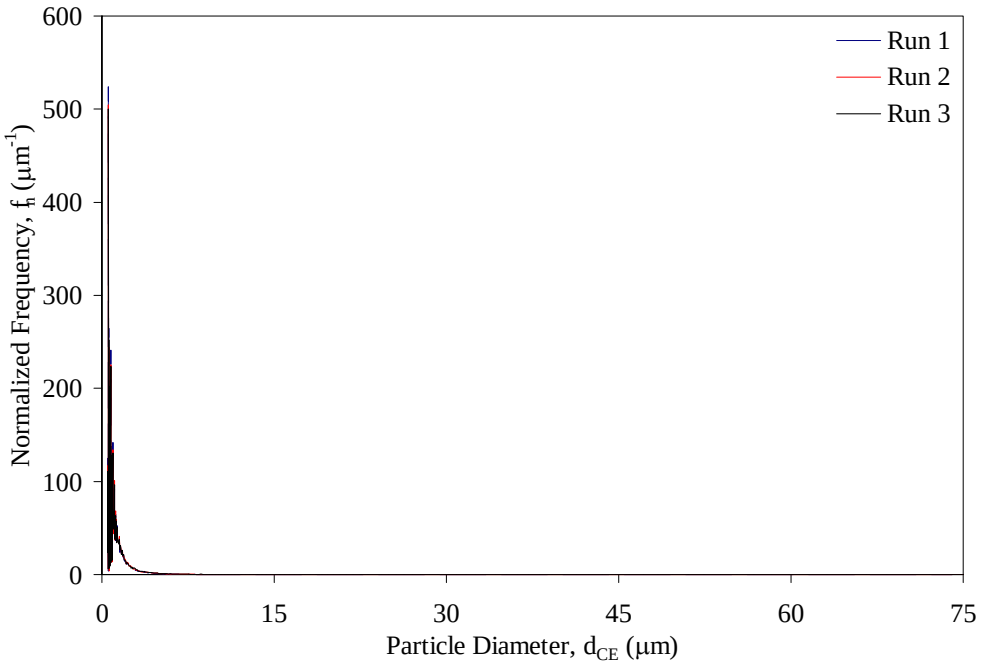

SU-TPSC

Aggregated

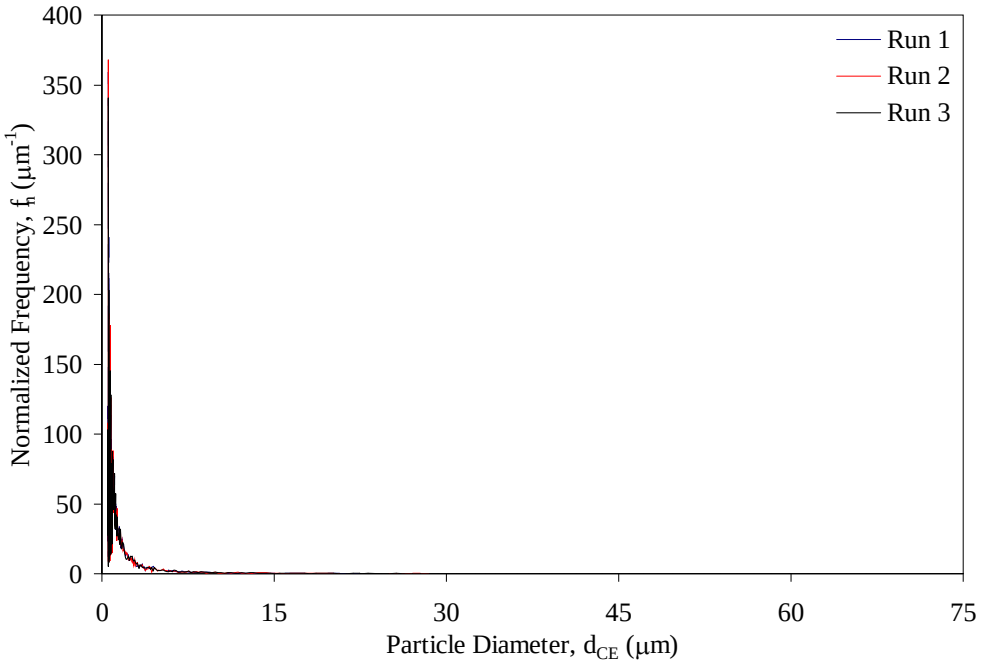

Dispersed

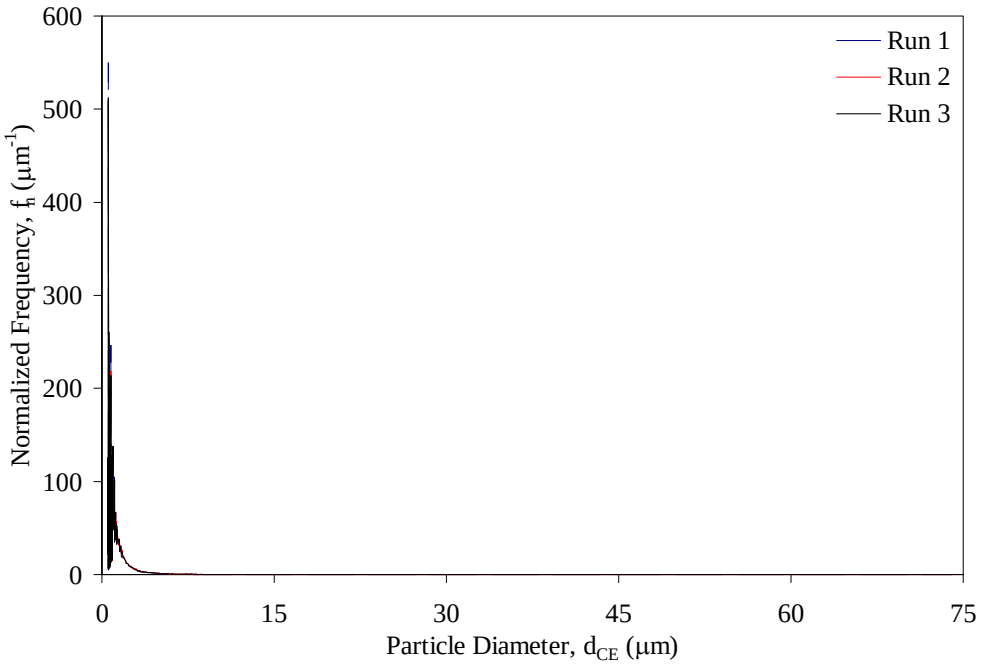

SU-TSF

Aggregated

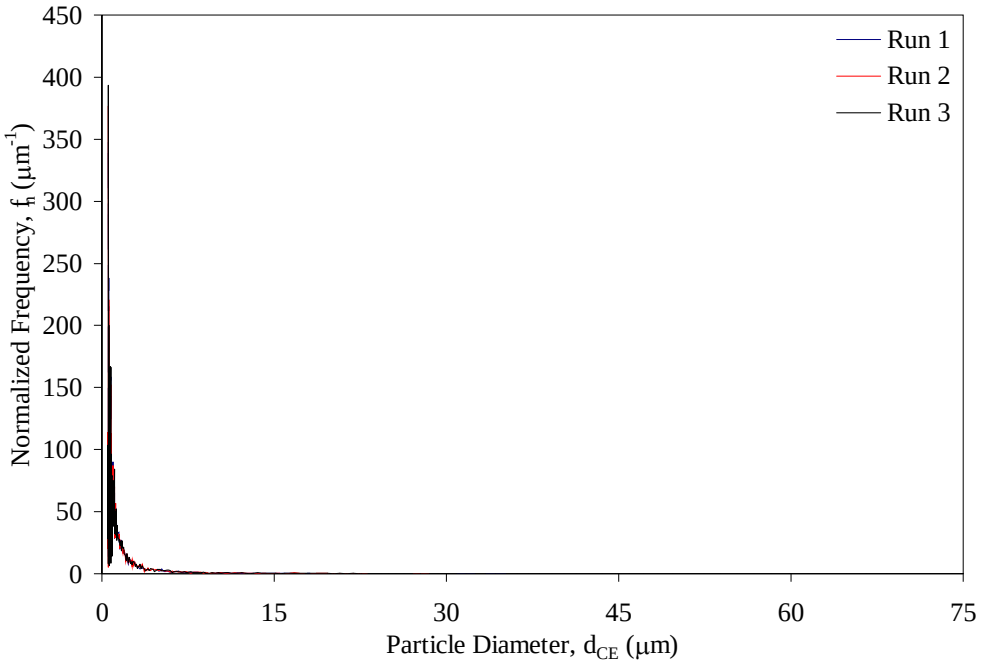

Dispersed

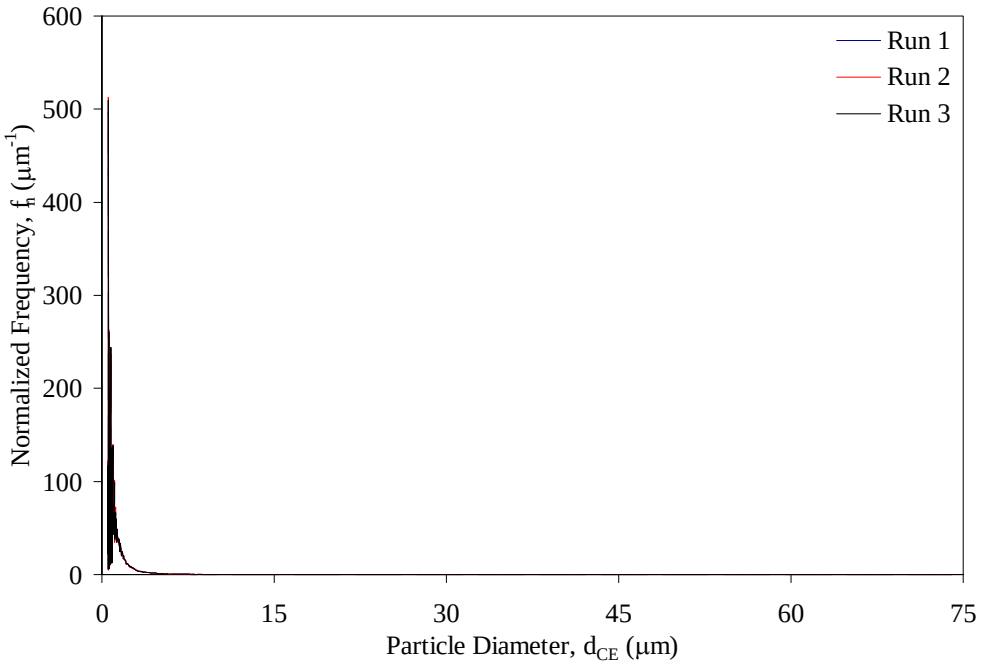

SY-HT

Aggregated

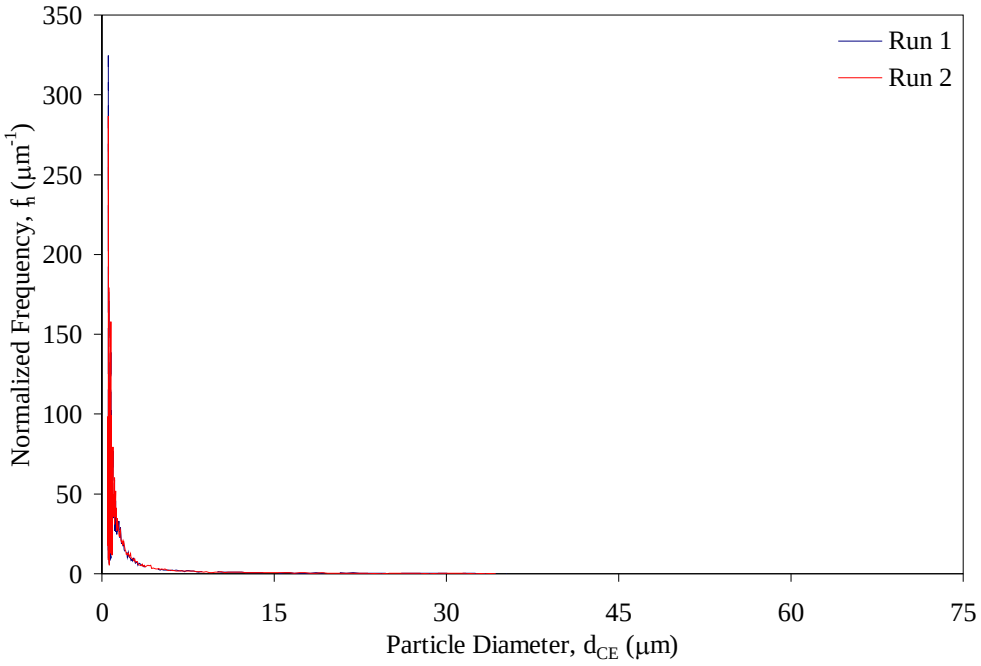

Dispersed

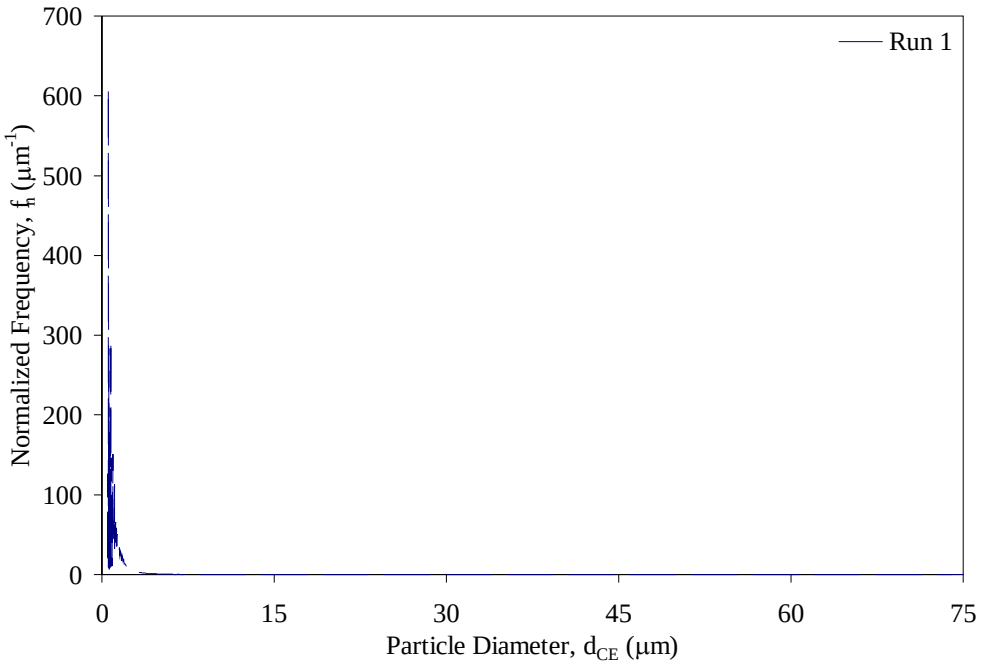

SY-M

Aggregated

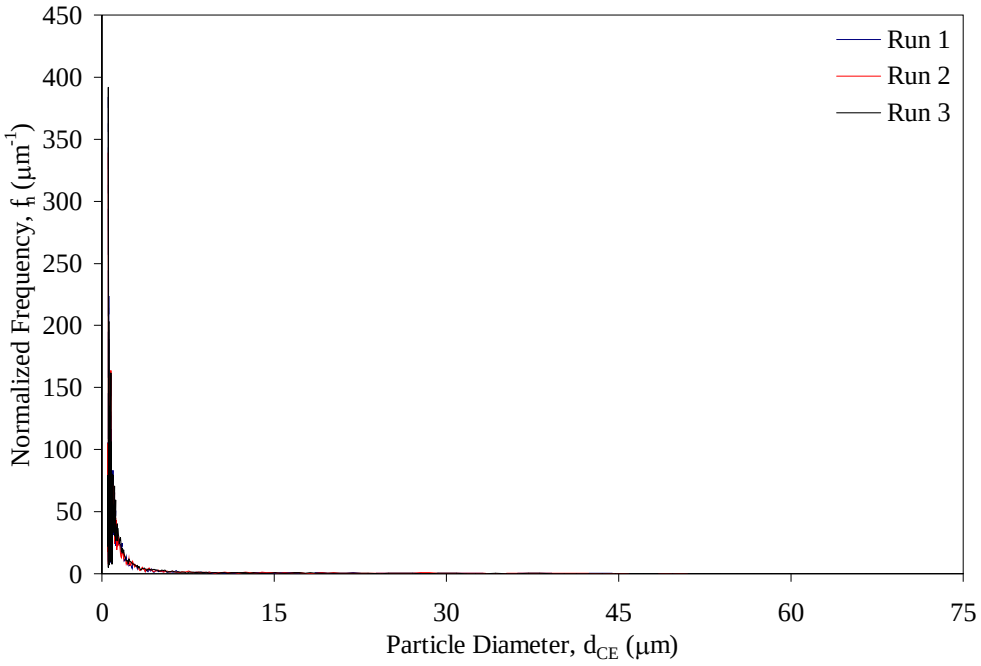

Dispersed

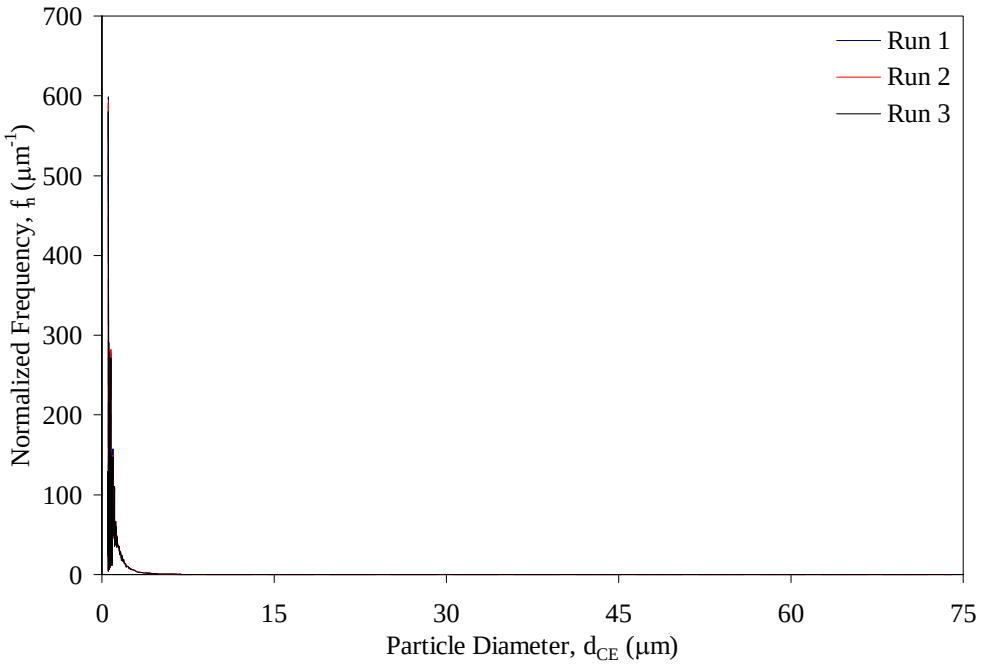

SY-T

Aggregated

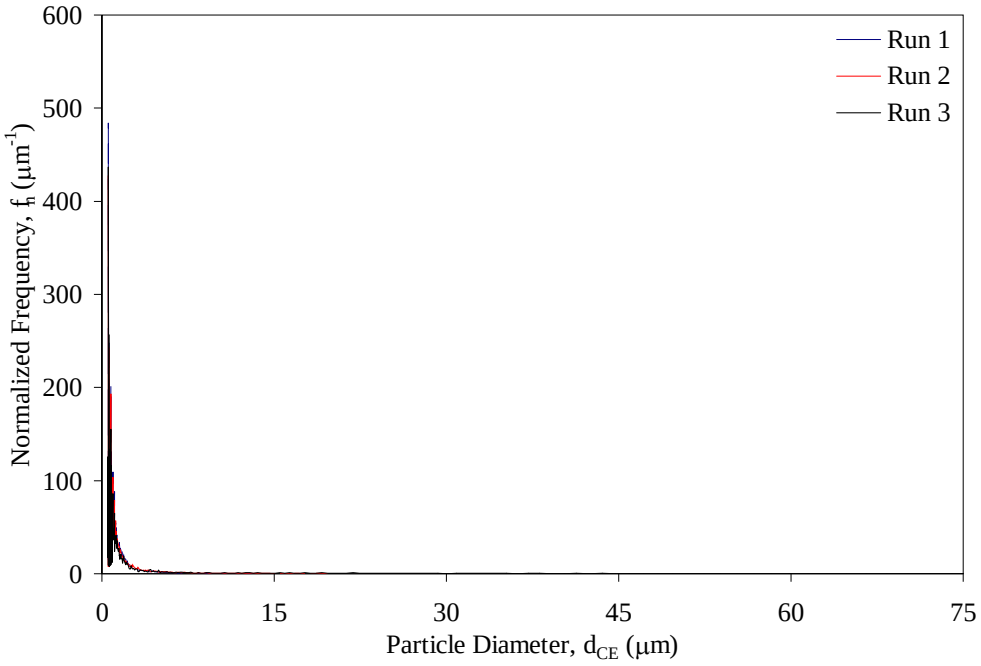

Dispersed

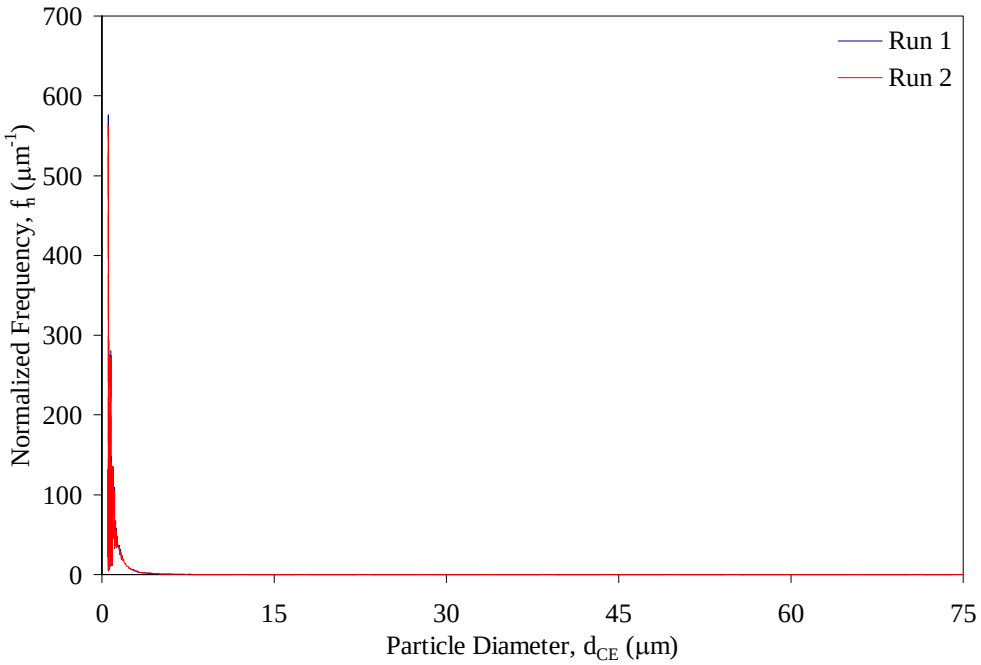

T-T

Aggregated

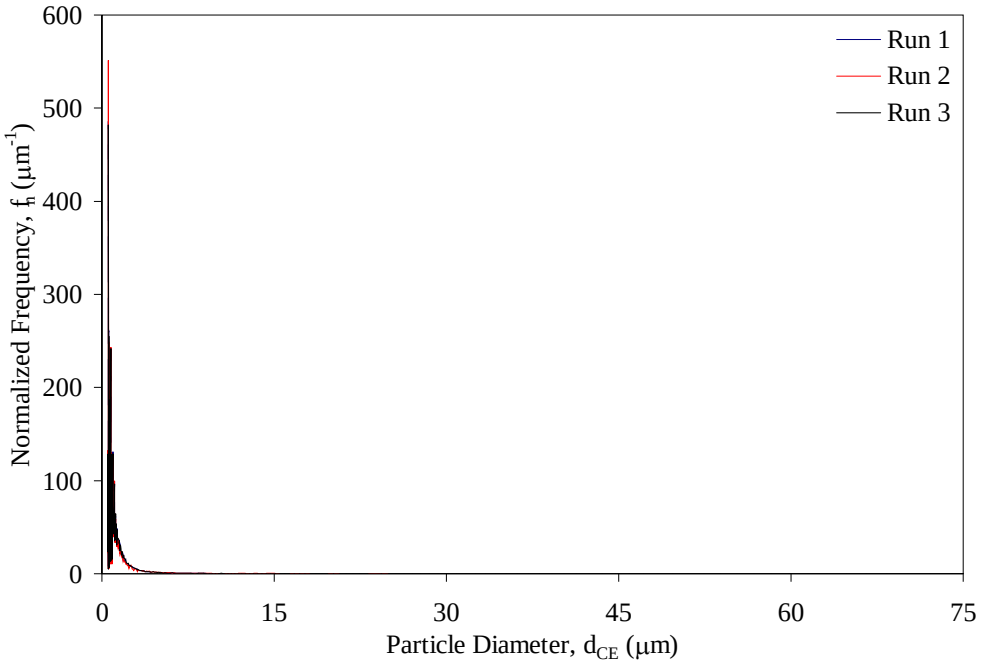

Dispersed

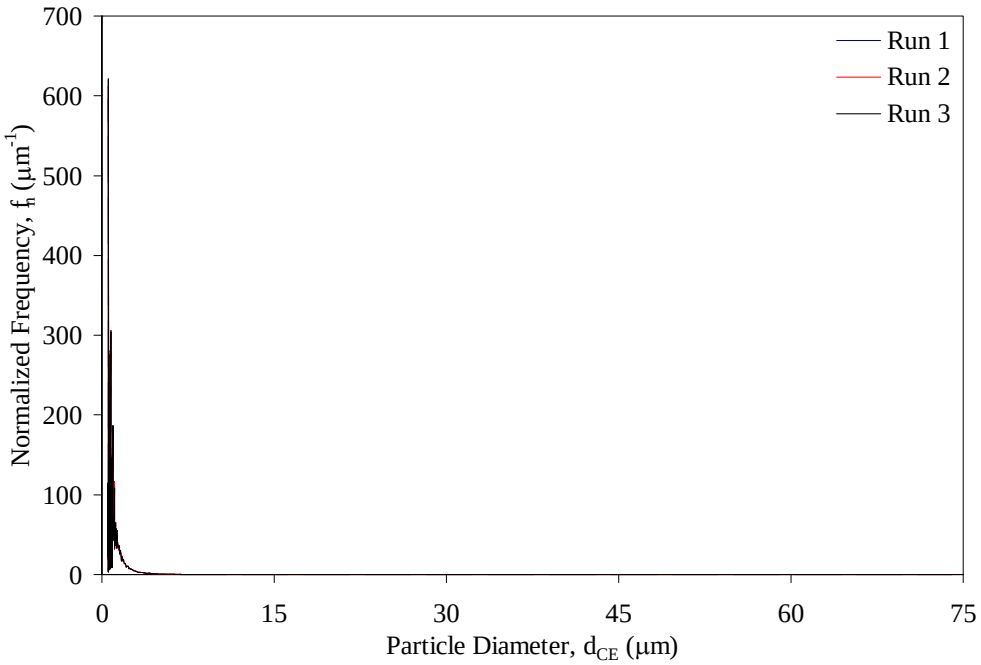

T-T(B)

Aggregated

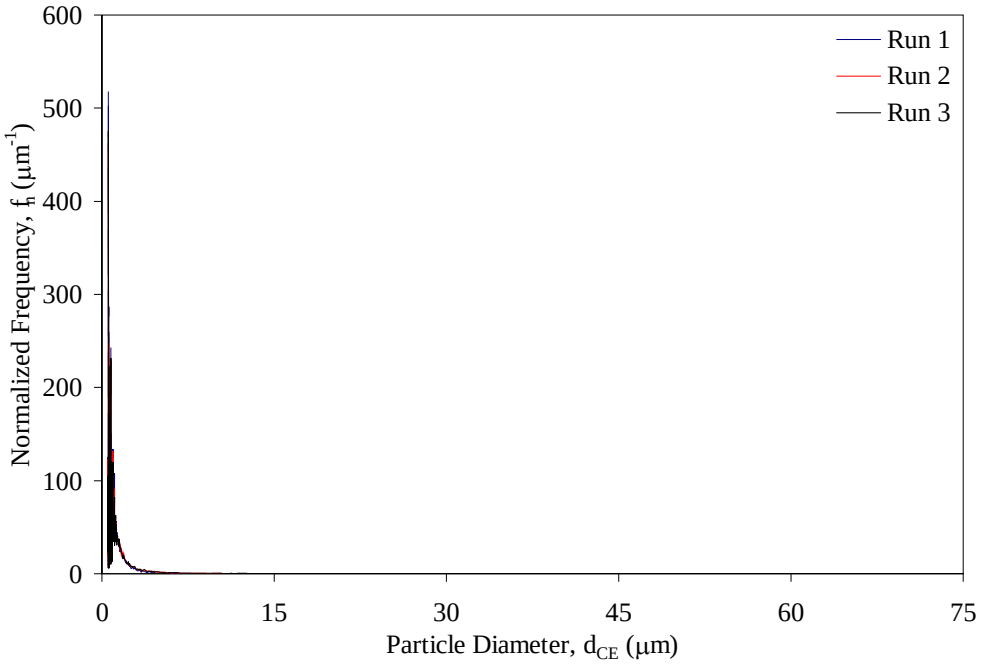

Dispersed

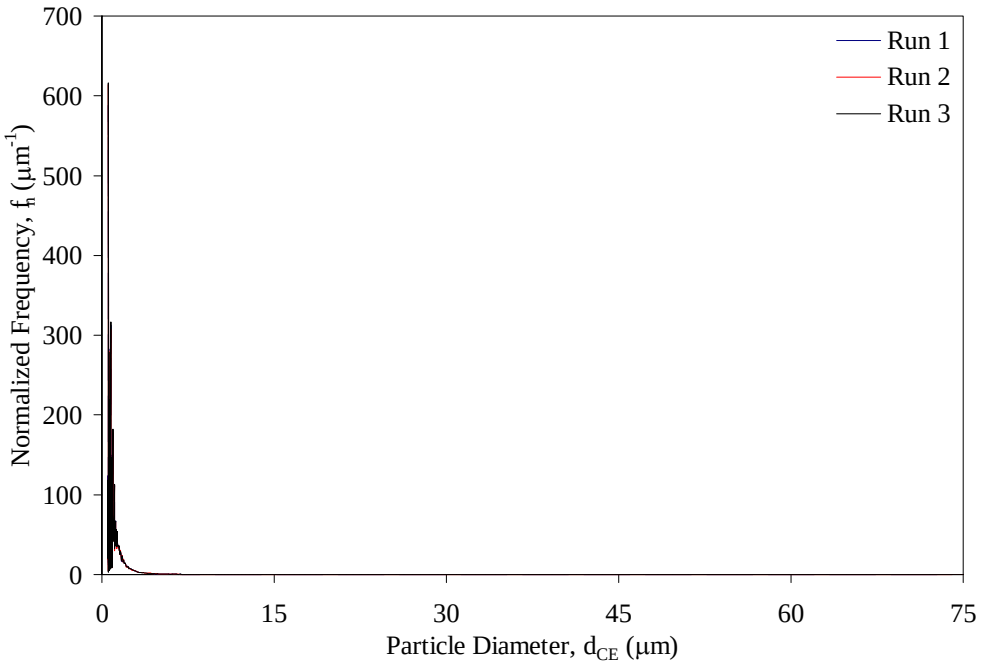

Appendix 9: Shape Distributions of Carrier Fluid Samples

S-M

Aggregated

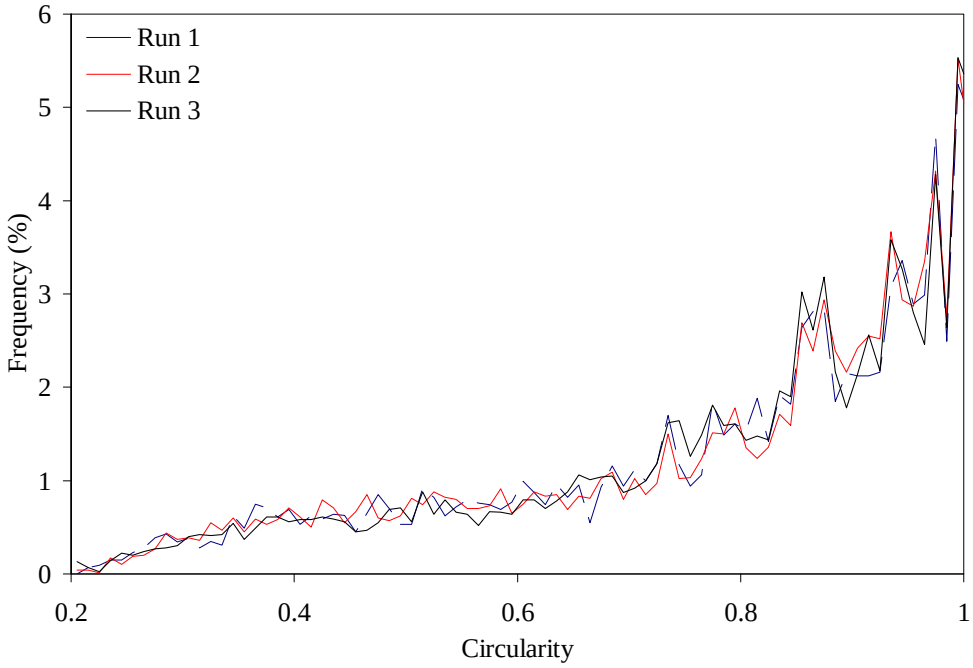

Dispersed

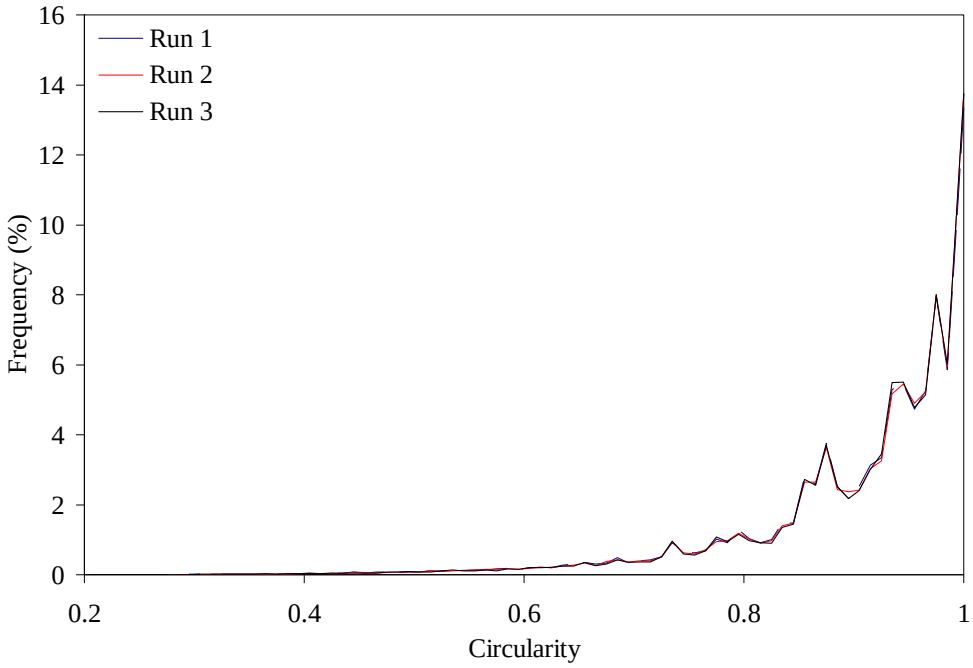

S-MFT

Aggregated

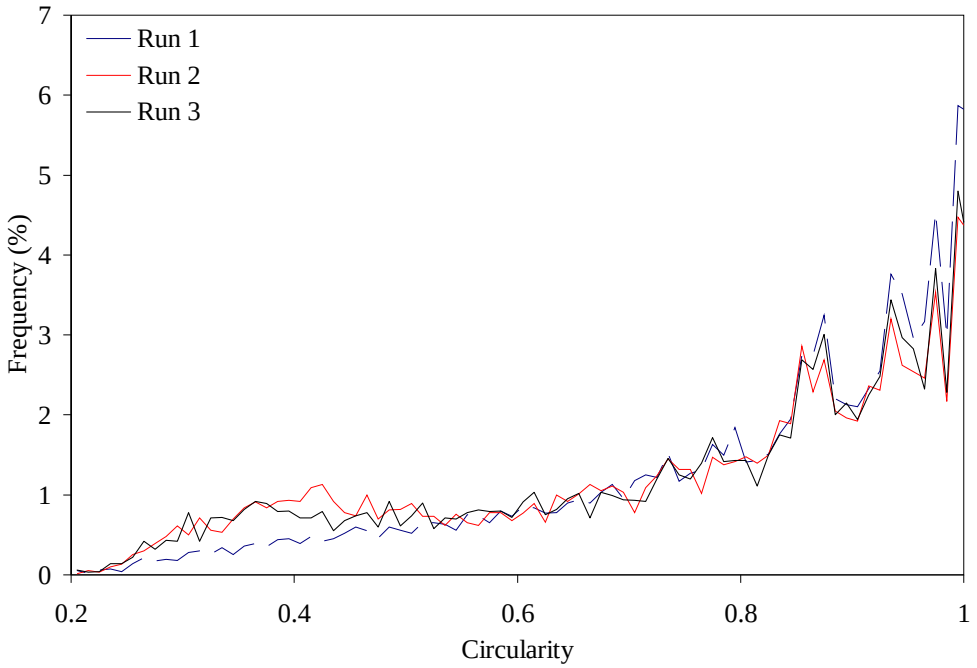

Dispersed

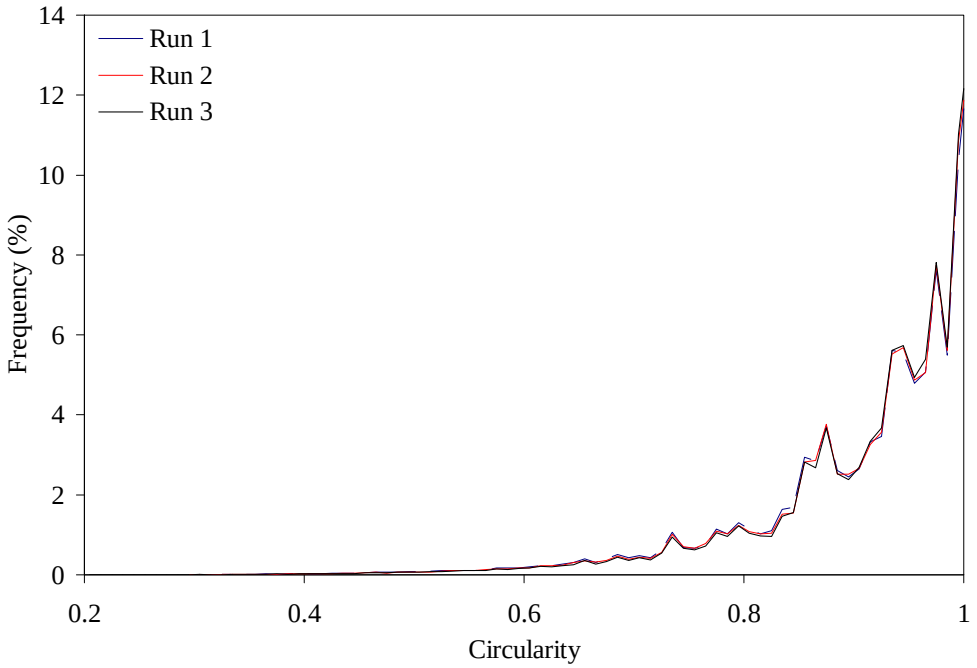

S-TSRU

Aggregated

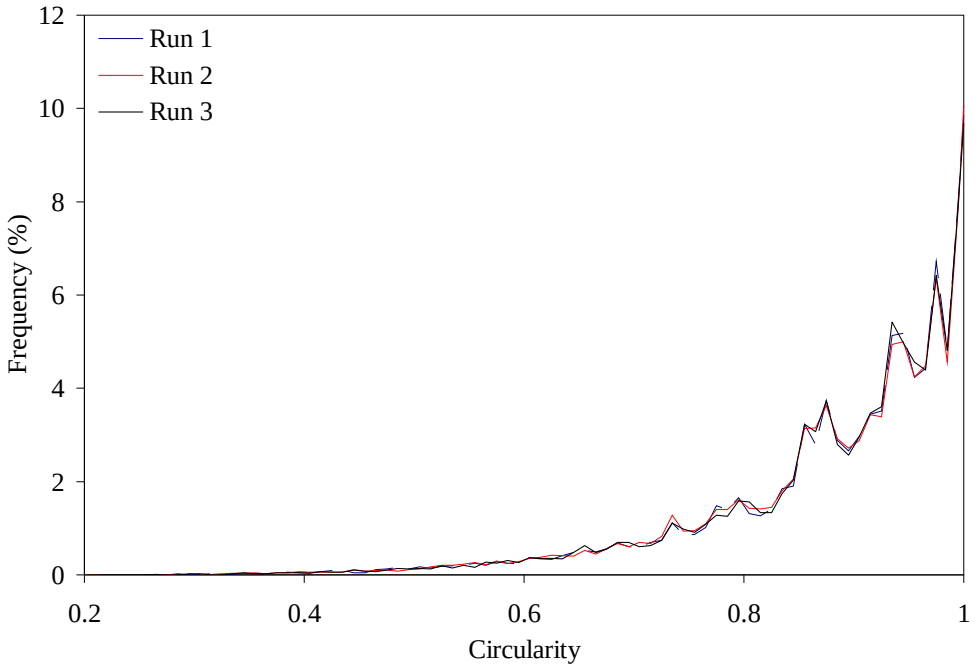

Dispersed

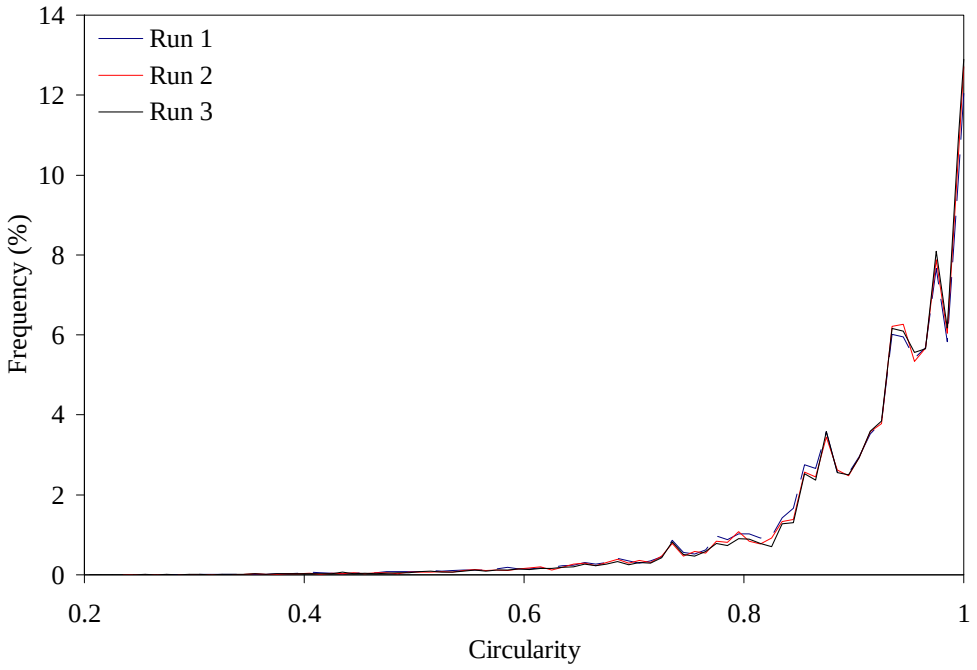

S-TT

Aggregated

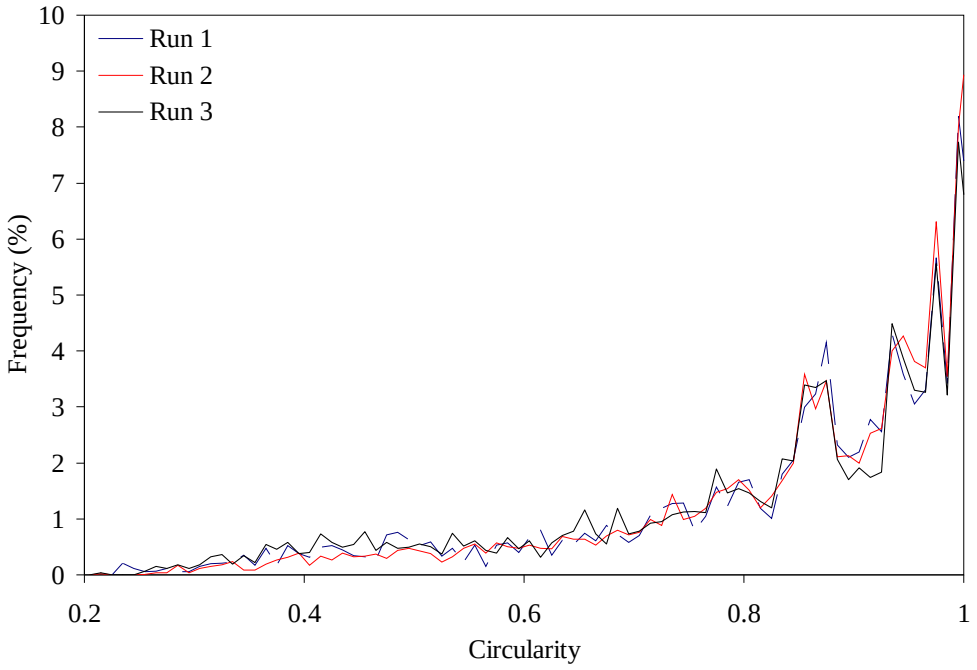

Dispersed

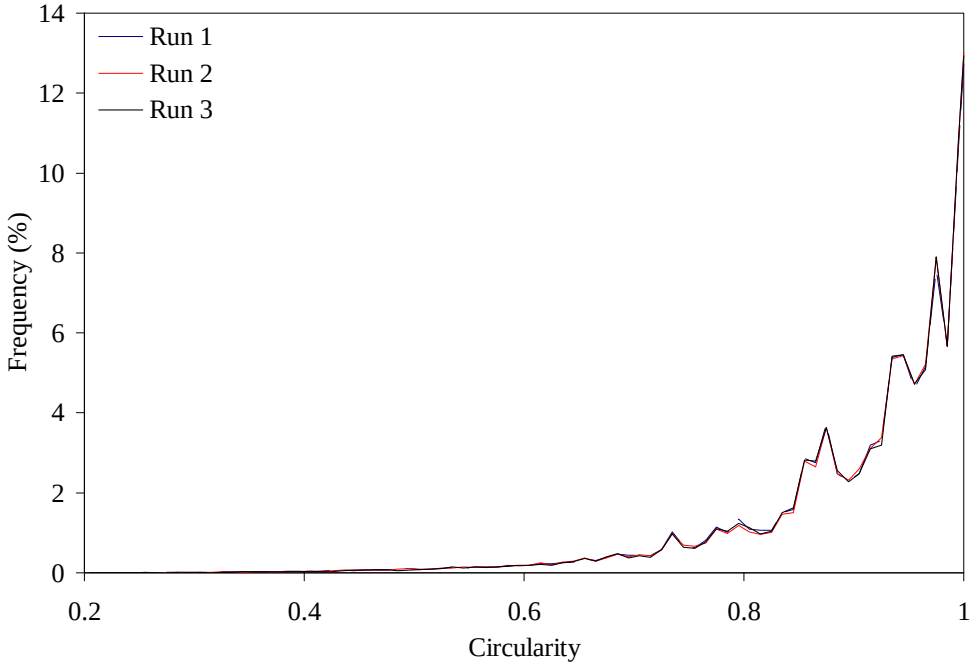

SU-M

Aggregated

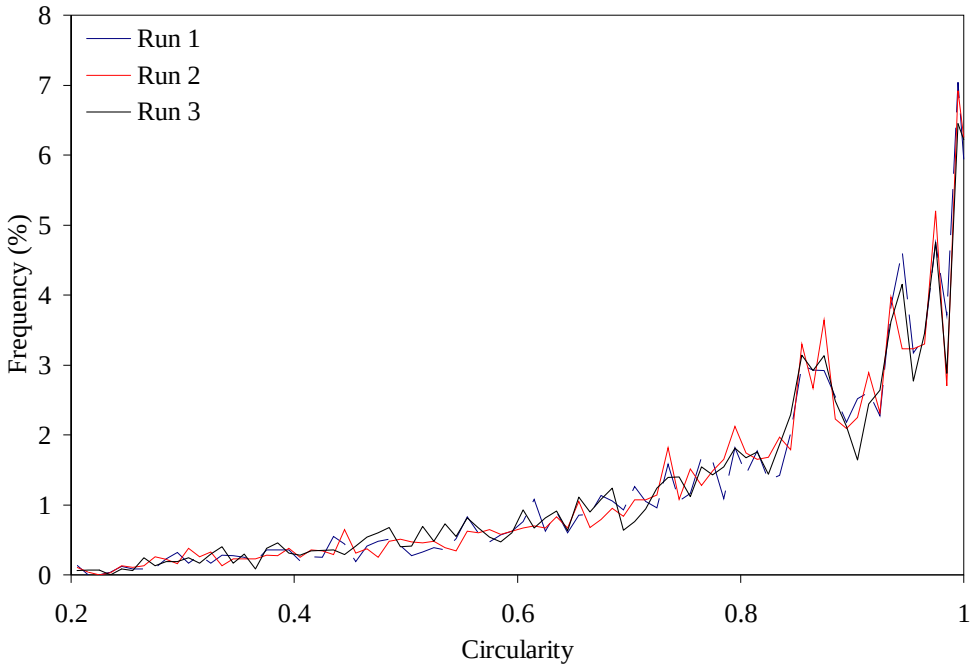

Dispersed

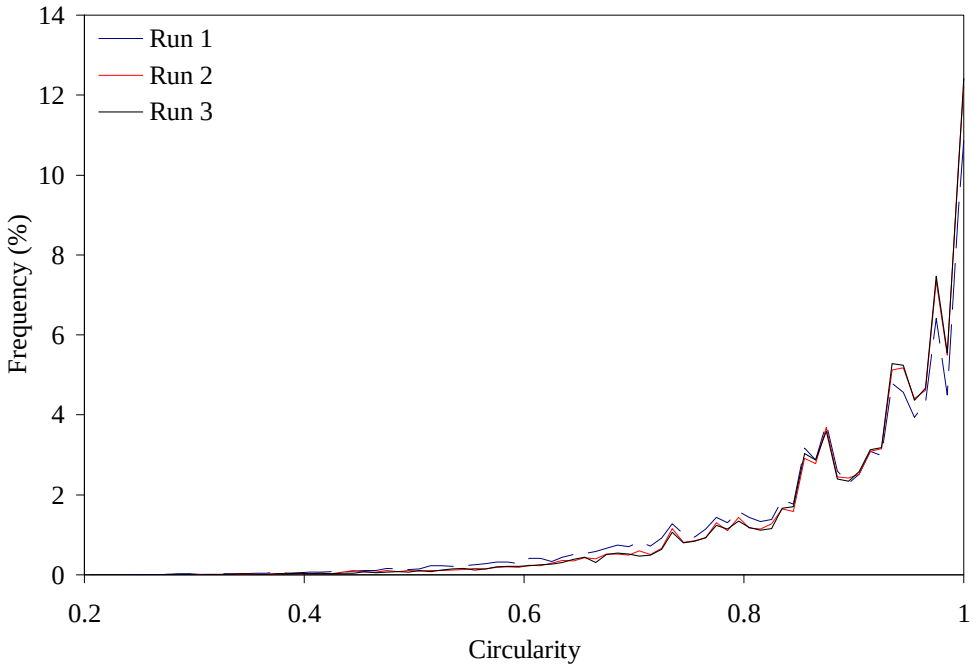

SU-NW

Aggregated

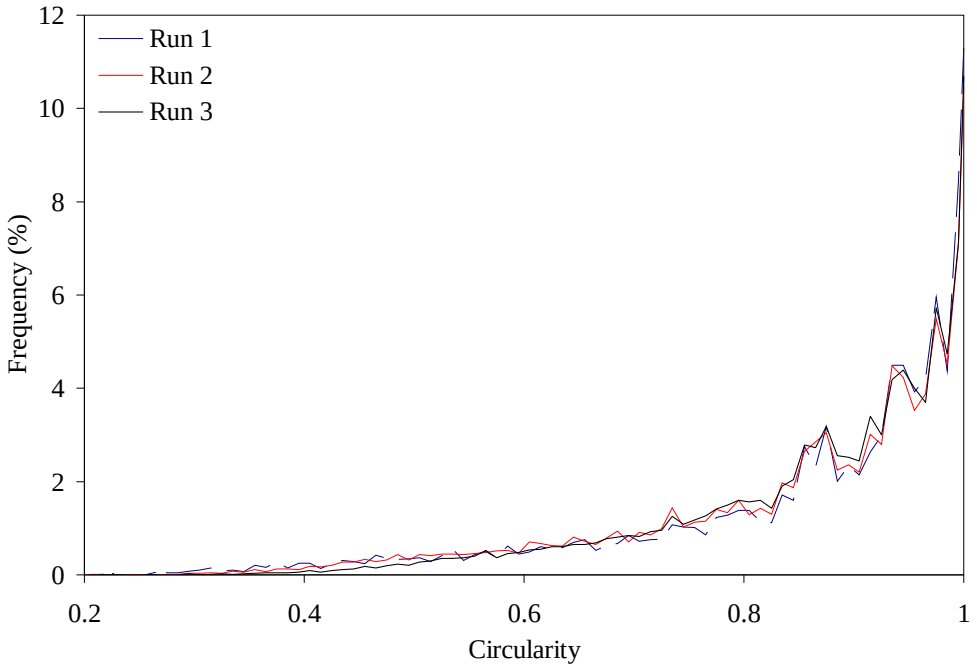

Dispersed

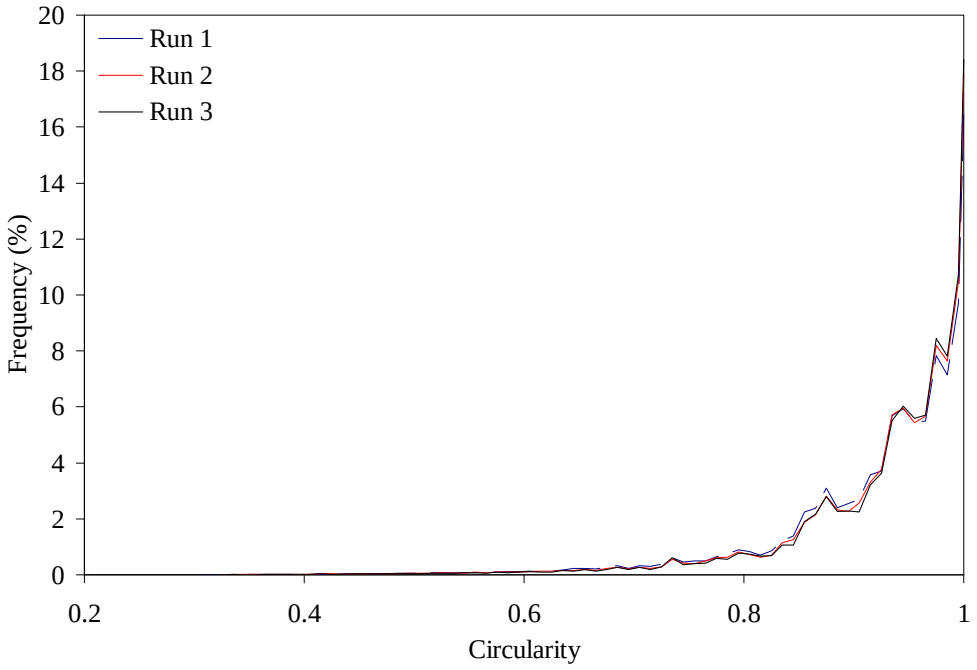

SU-RDW

Aggregated

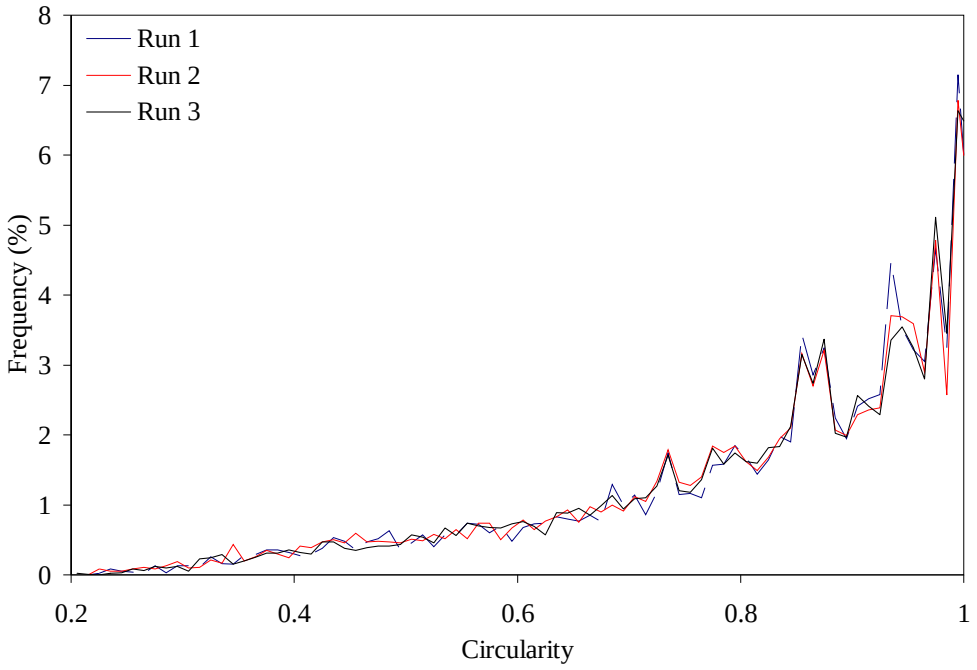

Dispersed

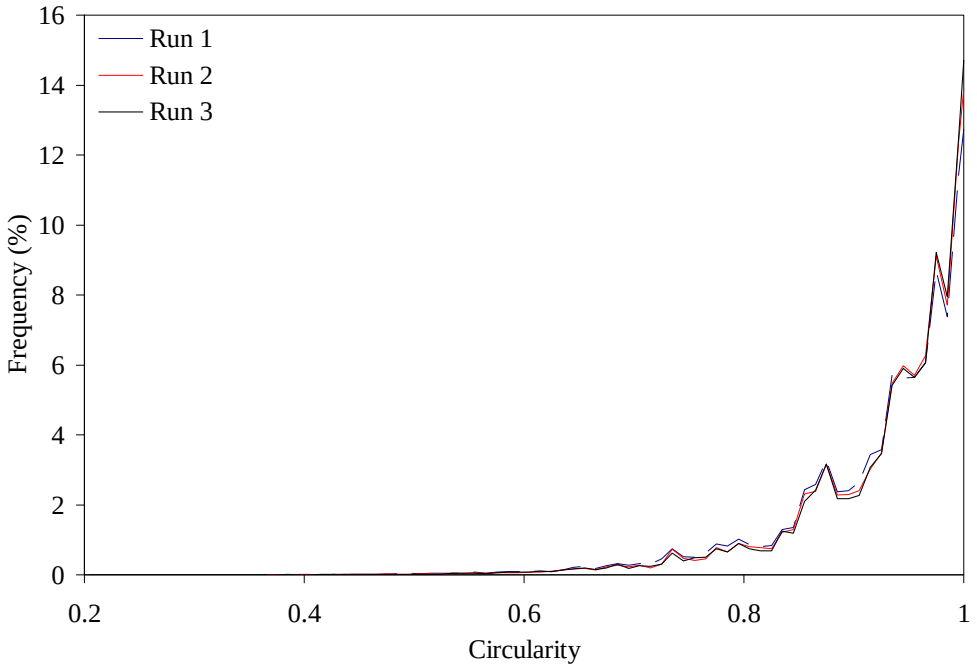

SU-T

Aggregated

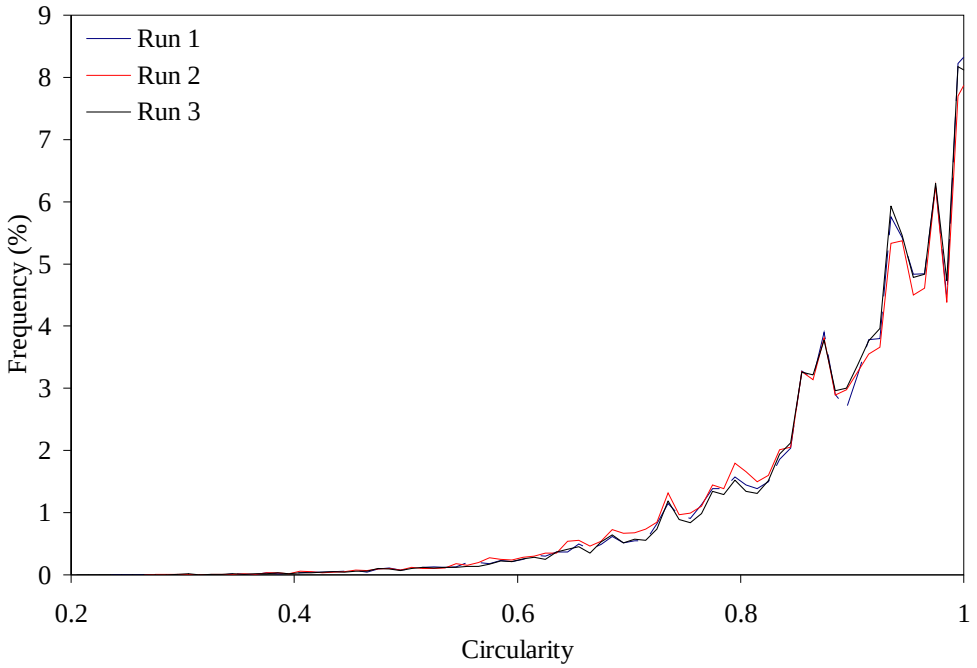

Dispersed

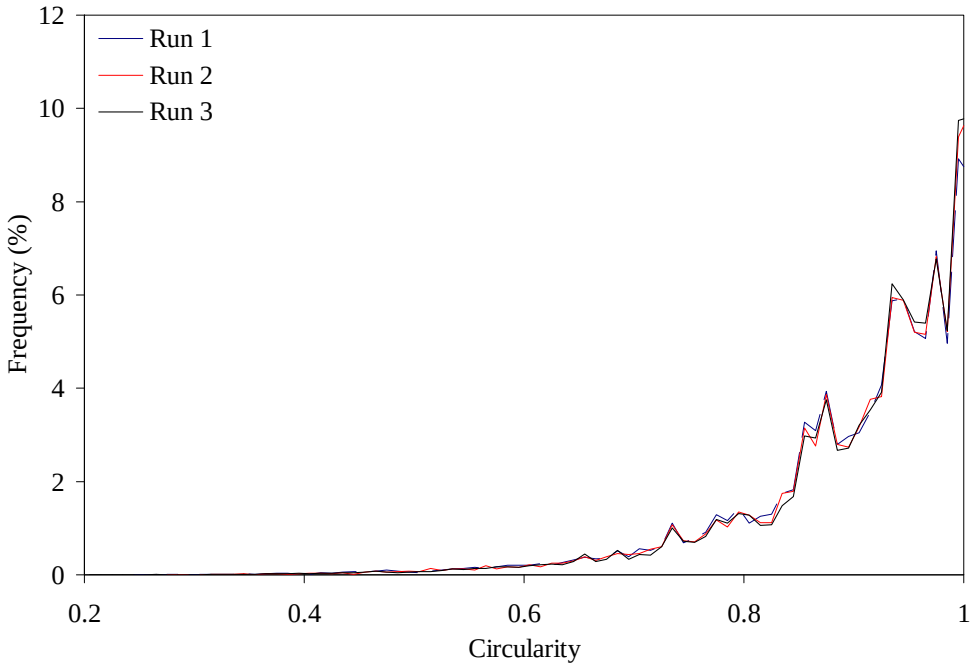

SU-TF

Aggregated

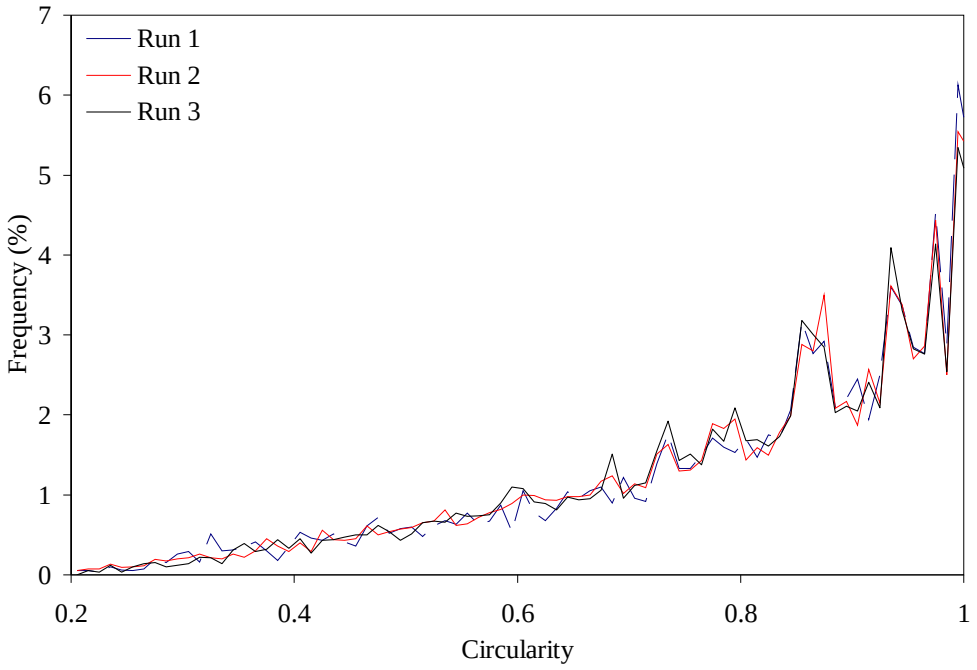

Dispersed

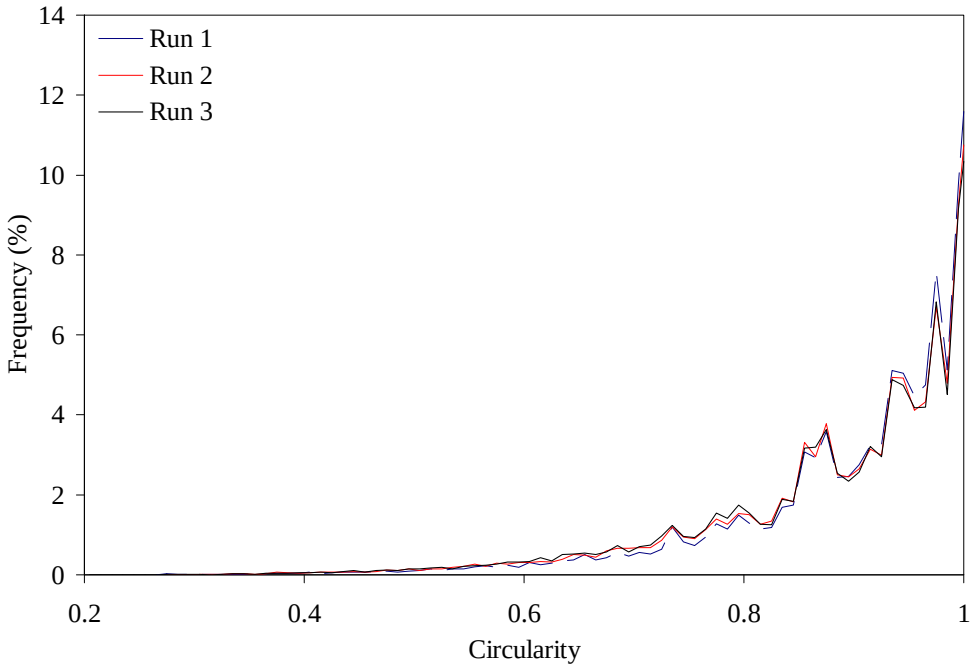

SU-TPSC

Aggregated

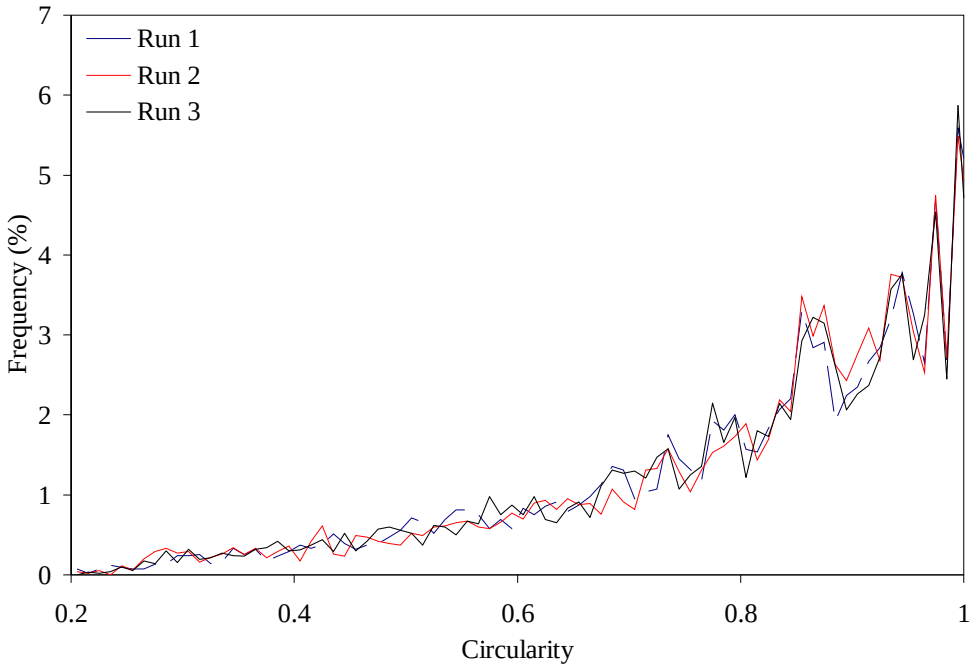

Dispersed

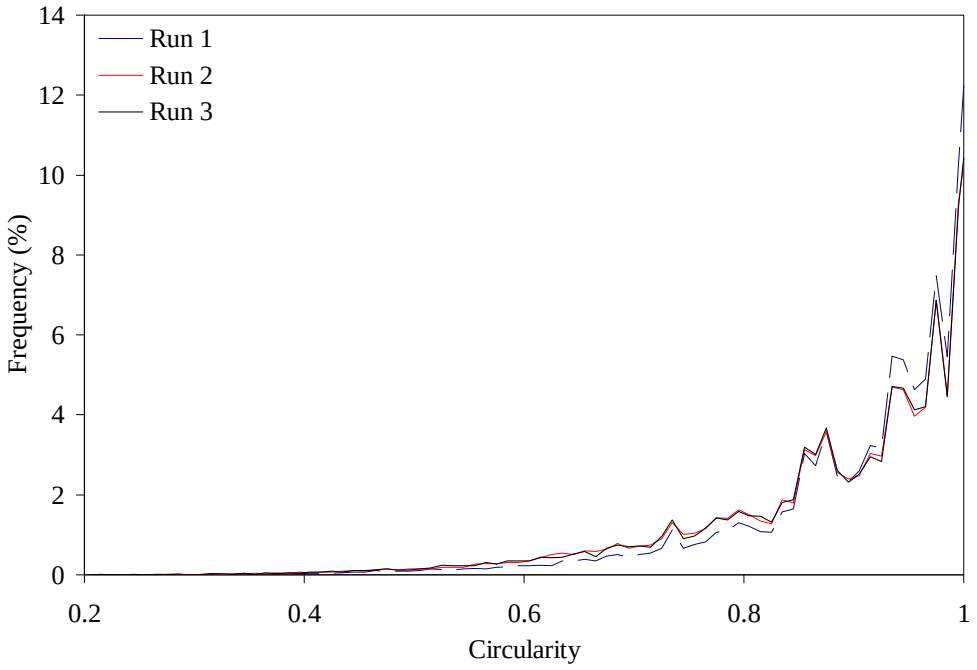

SU-TSF

Aggregated

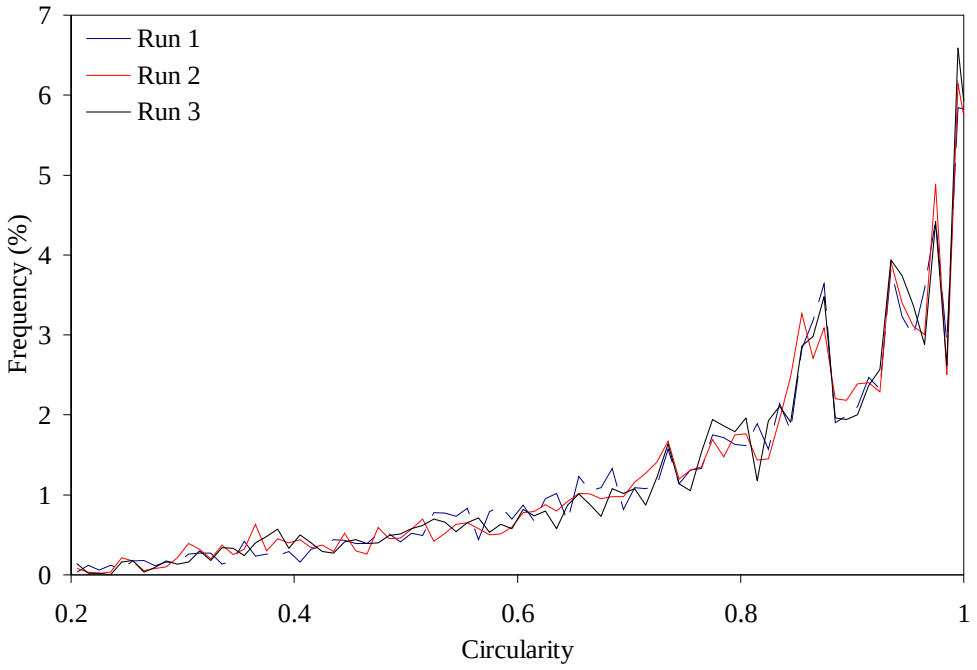

Dispersed

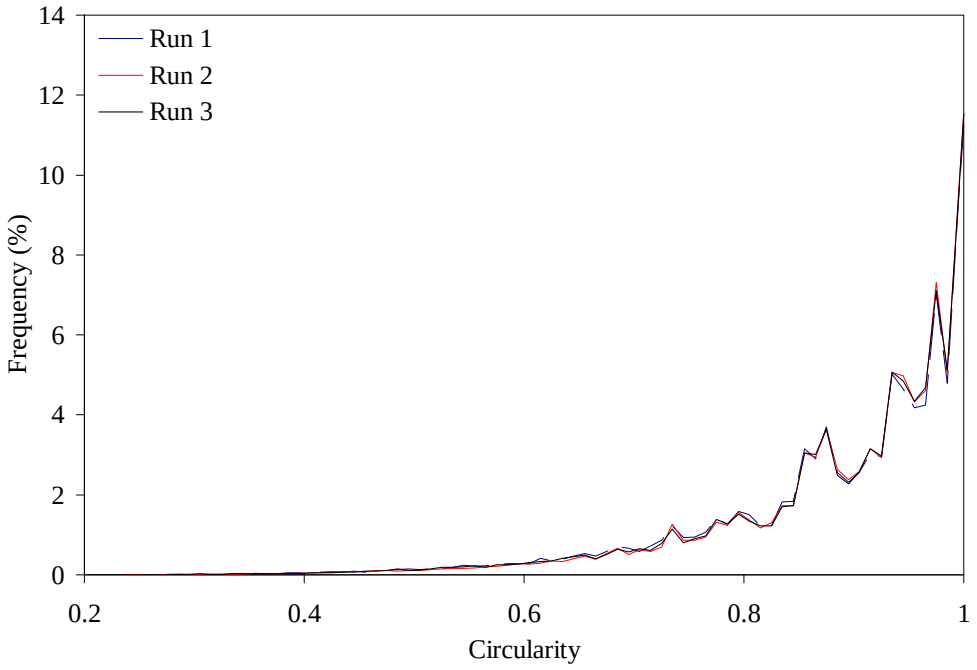

SY-HT

Aggregated

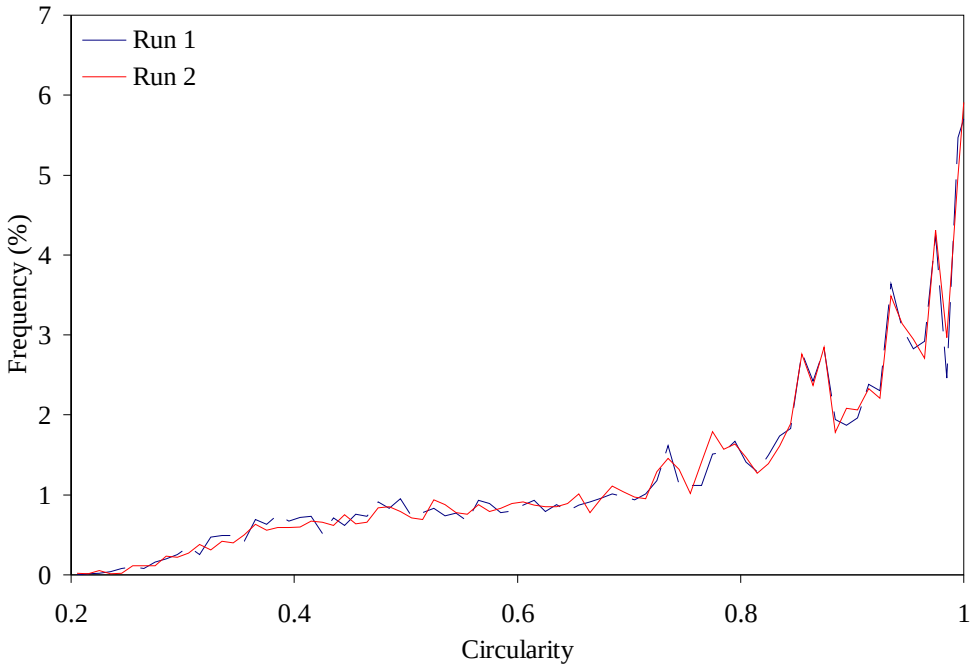

Dispersed

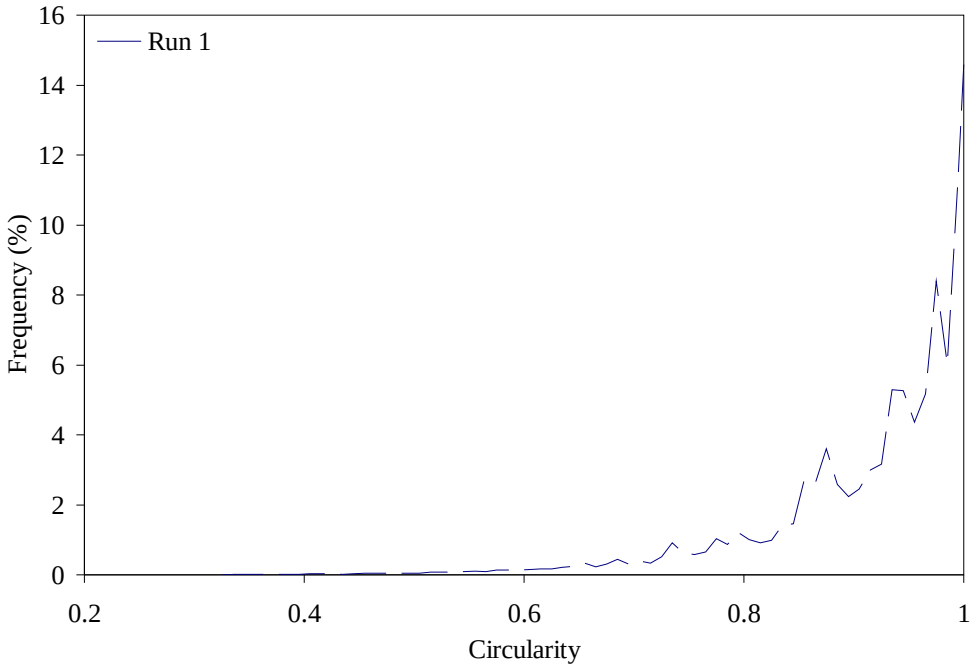

SY-M

Aggregated

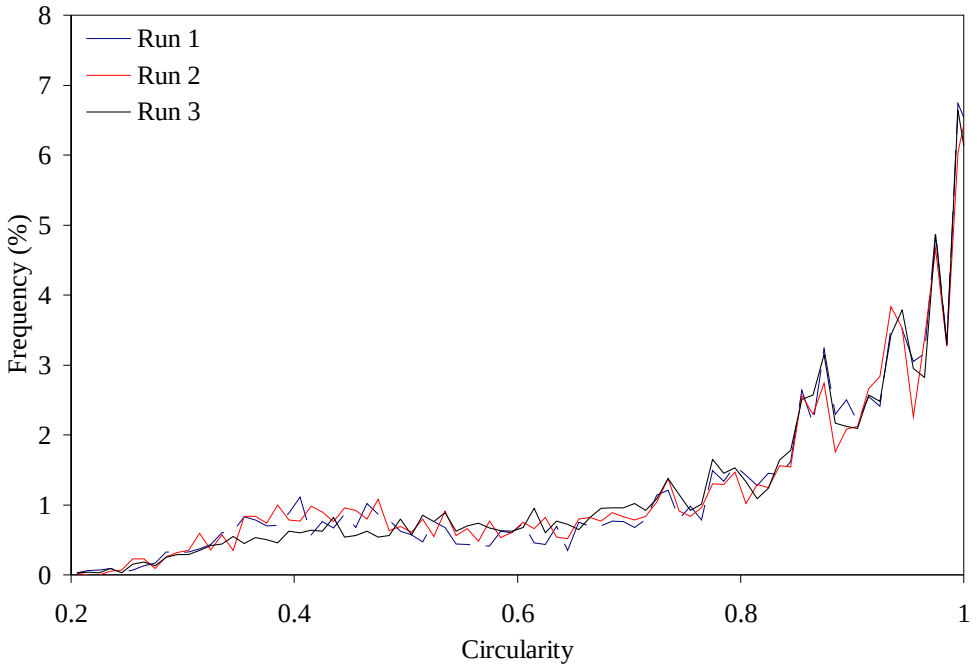

Dispersed

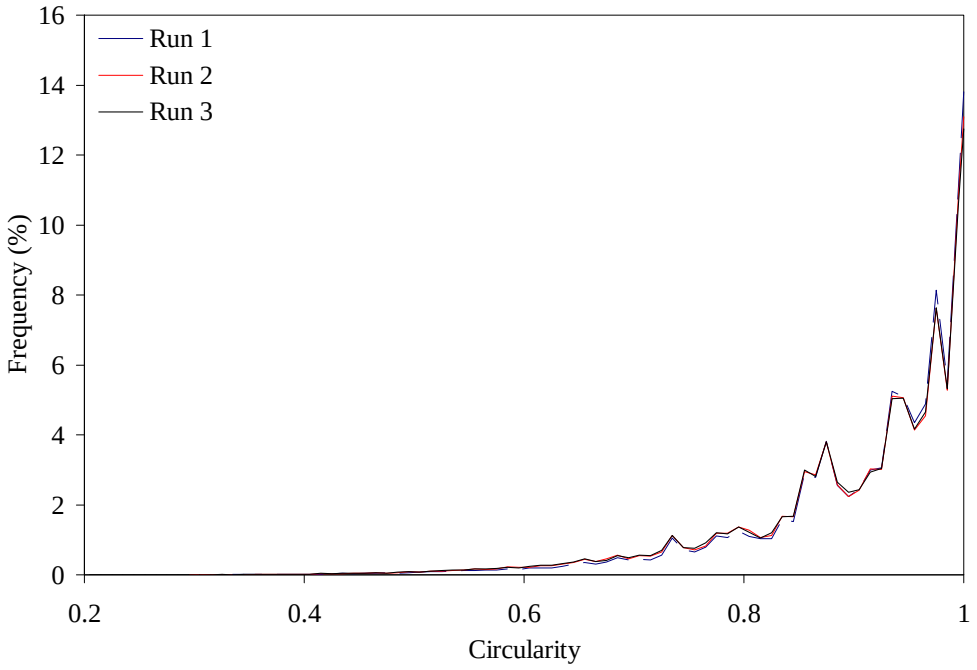

SY-T

Aggregated

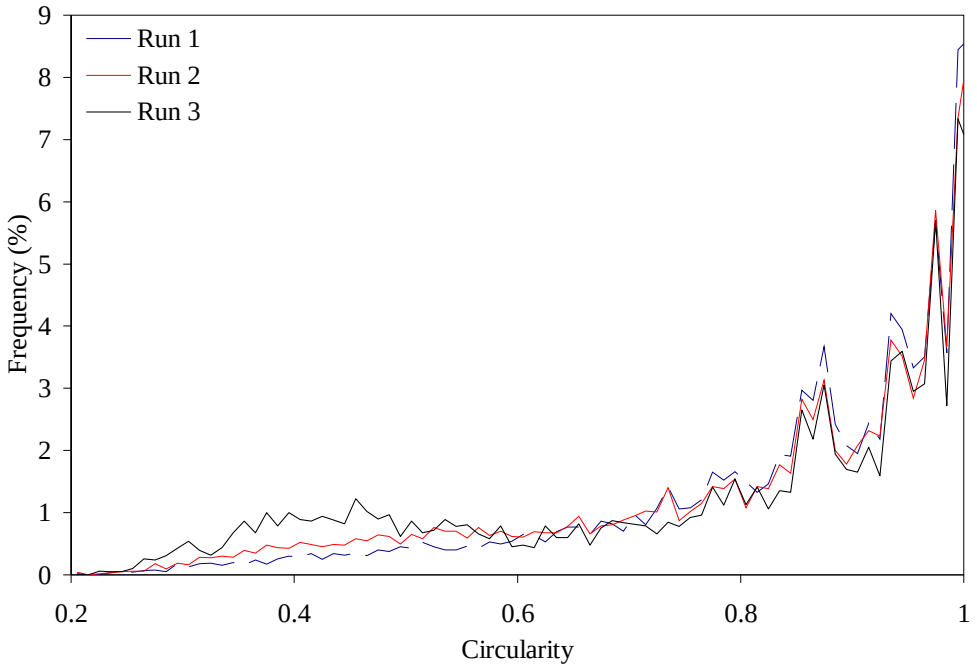

Dispersed

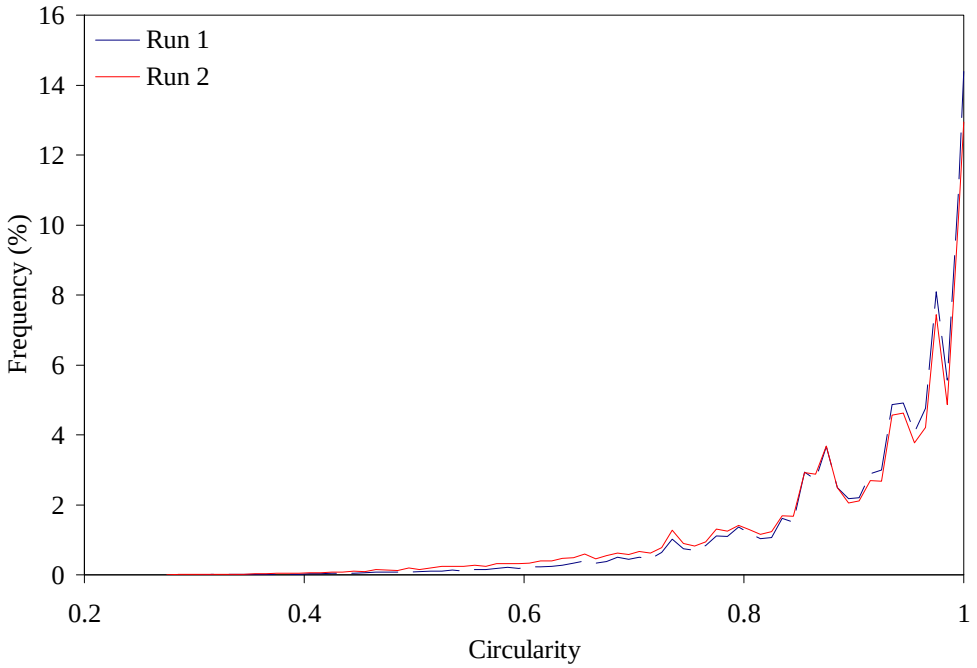

T-T

Aggregated

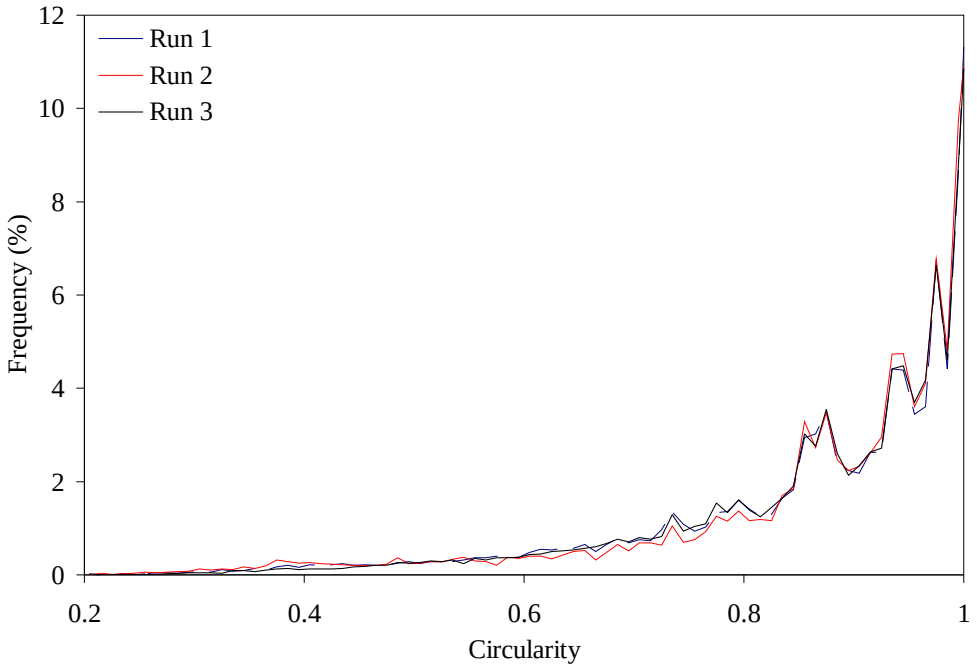

Dispersed

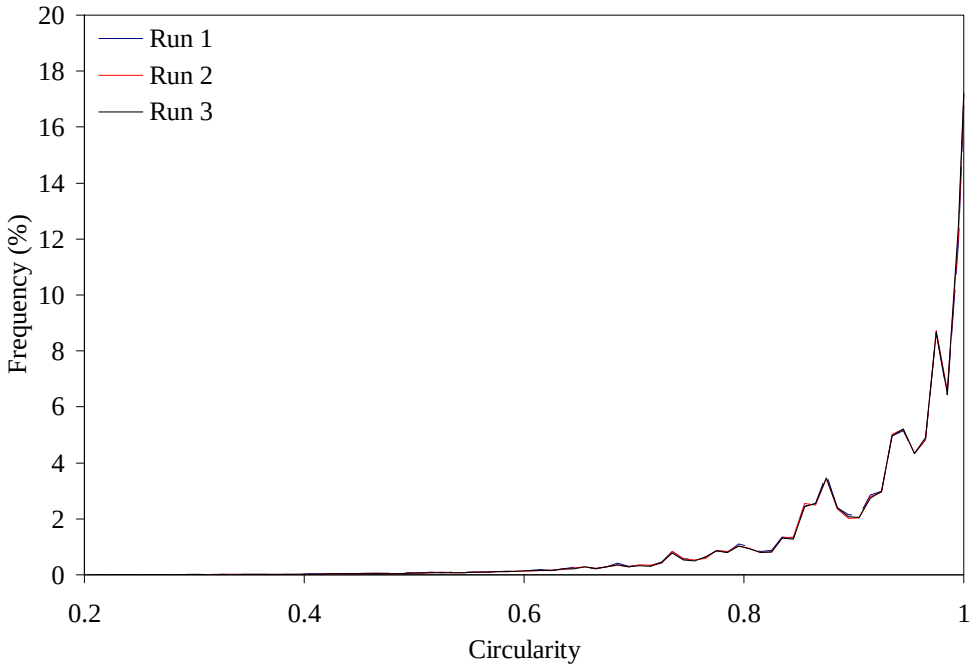

T-T(B)

Aggregated

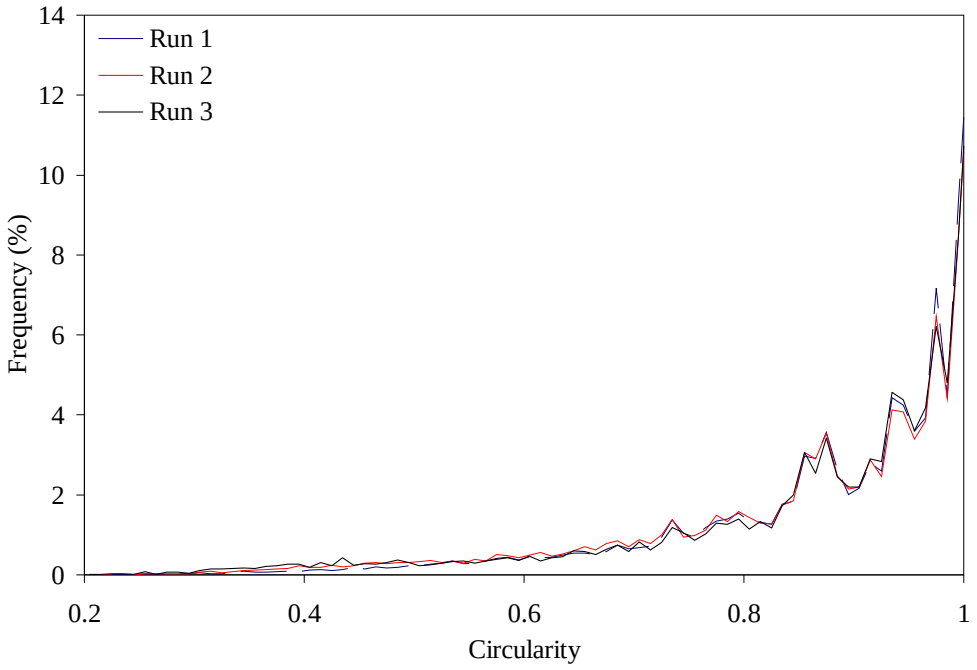

Dispersed